Signature of relic heavy stable neutrinos in underground experiments

D. Fargion

Dipartimento di Fisica Università degli Studi ''La Sapienza,'' 00185 Roma, Italy; I.N.F.N. Sezione di Roma I c/o Dipartimento di Fisica Università degli Studi ''La Sapienza,'' 00185 Roma, Italy; E. E. Faculty Technion Institute, Haifa, Israel

M. Yu. Khlopov

Cosmion Center for Cosmoparticle Physics, 125047 Moscow, Russia; M. V. Keldysh Institute of Applied Mathematics, 125047 Moscow, Russia; Moscow Engineering Physics Institute, 115409 Moscow, Russia

R. V. Konoplich

Dipartimento di Fisica Università degli Studi ''La Sapienza,'' 00185 Roma, Italy; Cosmion Center for Cosmoparticle Physics, 125047 Moscow, Russia; M. V. Keldysh Institute of Applied Mathematics, 125047 Moscow, Russia; E. E. Faculty Technion Institute, Haifa, Israel

R. Mignani

Dipartimento di Fisica ''E. Amaldi'' Università degli Studi ''Roma Tre,'' 00146 Roma, Italy; I.N.F.N. Sezione di Roma I c/o Dipartimento di Fisica Università degli Studi ''La Sapienza,'' 00185 Roma, Italy

(Submitted 22 September 1998)
Pis'ma Zh. Éksp. Teor. Fiz. **68**, No. 9, 657–662 (10 November 1998)

Considering heavy stable neutrinos of the 4th generation, we calculate the relic density of such neutrinos in the Universe. Taking into account the condensation of heavy neutrinos in the Galaxy and applying the results of calculations to experimental data from underground experiments on search for WIMPs in elastic neutral current scattering on nuclei, we find an exclusion region of neutrino mass 60 GeV$<m<$290 GeV. The bounds obtained from the present underground experiments, while confirming the previous bounds derived from analysis of cosmic ray spectra, are more reliable. We also discuss the first indication of elastic scattering induced by WIMPs in the DAMA experiment, finding a very narrow window of neutrino mass 45 GeV$<m<$50 GeV compatible with the possible signal rate in the detector. © *1998 American Institute of Physics.* [S0021-3640(98)00121-2]

PACS numbers: 98.80.Cq, 98.70.Sa, 14.60.Lm, 95.85.Ry

There are strong theoretical arguments and experimental evidence favoring an average density of matter in the Universe which might be significantly greater than the allowable 15% (Ref. 1) of critical density possibly provided by baryons. The nature of this dark matter is one of the most important questions facing both cosmology and particle physics. Among the various dark matter candidates, the theoretical favorites are

light neutrinos, axions, and neutralinos. However, in some models heavy neutrinos can play an important role in cosmology as a cold dark matter component contributing a part of the closure density.

In the present article we calculate the heavy neutrino density in the Galaxy and apply the results of calculations to experimental data from underground experiments on the direct search for WIMP–nucleus elastic scattering in order to obtain bounds on the mass of neutrino of the 4th generation.

To be specific, we consider the standard electroweak model but with the inclusion of one additional family of fermions. The heavy neutrino ν and heavy charged lepton L form a standard $SU(2)_L$ doublet. In order to ensure the stability of the heavy neutrino, we assume that its mass $m<M_L$ and that the heavy neutrino is a Dirac particle.

It is known that modern laboratory experimental results are not inconsistent with the existence of heavy Dirac neutrinos with mass $m<M_Z/2$, where M_Z is the mass of the Z boson. In the early Universe at high temperatures such heavy neutrinos should be in thermal equilibrium with other species of particles. As the temperature in the Universe drops, heavy neutrinos become nonrelativistic (at $T=m$), and their abundance falls off rapidly according to exponential law. In the further expansion of the Universe, as the temperature decreases below the freeze-out value T_f, the weak interaction processes become too slow to keep neutrinos in equilibrium with other particles. As a consequence, the number density of heavy neutrinos fails to follow the equilibrium concentration, reaching at present

$$n=\frac{6\times 10^3}{\sqrt{g_*}}\left(\frac{m_p}{M_{PL}}\right)\left(\frac{m_p}{m}\right)\left(\frac{\rho_c}{10^{-29}h^2\,\mathrm{g\cdot cm^{-3}}}\right)\left[\int_0^{x_f} dx m_p^2(\sigma v)\right]^{-1}\mathrm{cm}^{-3}, \tag{1}$$

where $\rho_c=1.879\times 10^{-29}h^2\,\mathrm{g\cdot cm^{-3}}$ is the critical density of the Universe; h is the normalized Hubble constant; $M_{PL}=1.221\times 10^{19}$ GeV is the Planck mass; m_p is the proton mass; $x=T/m$; $x_f=T_f/m$; σ is the annihilation cross section; v is the relative velocity of the neutrino–antineutrino pair in its center-of-mass frame; g^* is the effective number of relativistic degrees of freedom at $T=T_f$ (bosons contribute 1 to g^* and fermions 7/8). The freeze-out temperature T_f can be computed iteratively from

$$x_f^{-1}=\ln\frac{0.0955 M_{PL}\sigma v m\sqrt{x_f}}{\sqrt{g^*}}, \tag{2}$$

and generally $T_f \approx m/30$.

In the general case the following processes could lead to the annihilation of heavy neutrinos in the Universe: $\nu\bar{\nu}\to f\bar{f}$, W^+W^-, ZZ,ZH,HH; however, the dominant processes are $\nu\bar{\nu}\to f\bar{f}$ below the threshold for W^+W^- production and $\nu\bar{\nu}\to W^+W^-$ above the threshold.[2]

Figure 1 shows the dependence of the cosmological density $\rho_\nu=2mn$ of heavy neutrinos as a function of neutrino mass. In the region $m\sim M_Z/2$, the neutrino density is extremely small as a result of the huge value of the annihilation cross section at the Z boson pole. As the neutrino mass increases, the cross section for neutrino annihilation drops, and this leads to an increase of the neutrino density, which reaches its maximum

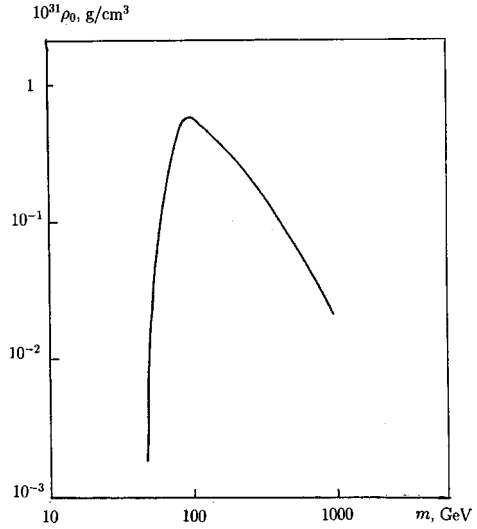

FIG. 1. Cosmological density of heavy neutrinos as a function of neutrino mass.

value at $m \approx 100$ GeV. At $m > M_W$ the annihilation channel into W^+W^- opens and gradually becomes the dominant one, and since its cross section grows as m^2 (Refs. 2 and 3), the present neutrino density drops again.

As is seen from Fig. 1, the neutrino density is small in comparison with the critical density. In the Galaxy, however, the neutrino density can be increased by some orders of magnitude due to neutrino condensation. It has been shown[3,4] that at the stage of galaxy formation the motion of heavy neutrinos in the nonstatic gravitational field of ordinary matter, which contracts as a result of energy dissipation via radiation, provides an effective mechanism of energy dissipation for neutrinos. As a consequence, the contracting ordinary matter induces the collapse of the neutrino gas and leads to the following significant increase in the neutrino density in the central part of the Galaxy:

$$n_{0G} \approx n\left(\frac{\rho_{0G}}{\rho_U}\right)^{3/4}, \tag{3}$$

where $\rho_{0G} \approx 10^{-20}$ g$\cdot$cm^{-3} is the central density of matter in the Galaxy and $\rho_U \approx 4 \times 10^{-31}g\cdot$cm^{-3} is the density of matter in the Universe (here we take an upper bound[1] on the density of matter in order to obtain a lower bound on the neutrino density). It is often assumed that the density of the dark matter halo in the Galaxy decreases with distance from the center according to the law

$$\rho(r) = \frac{\rho_0}{1 + (\rho/a)^2}, \tag{4}$$

where a (2 kpc$< a <$20 kpc) is the core radius of the halo. Assuming that the neutrino density also follows the distribution (4), taking the minimal value for the core radius $a = 2$ kpc, and substituting into Eq. (4) the distance $r_{\text{Sun}} \approx$ 8.5 kpc from the Sun to the center of the Galaxy, we find that the density in the solar neighborhood is reduced by a

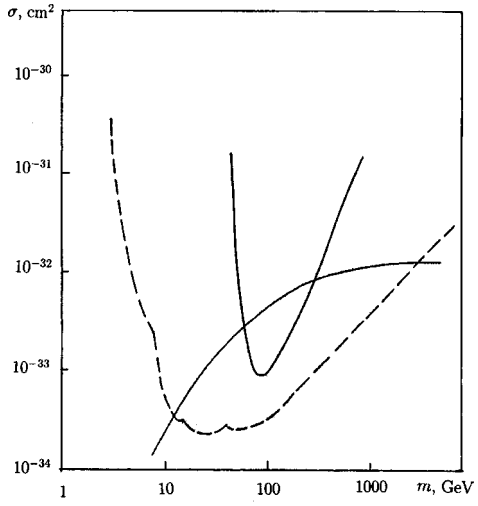

FIG. 2. Mass exclusion plot for the interaction of dark matter particles with Ge. The dashed curve represents the boundary[7] corresponding to the case when neutrinos constitute all dark matter (ρ=0.3 GeV·cm^{-3}). The solid curve corresponds to the ''real'' neutrino density in the Galaxy. The curve near the bottom of the plot shows the predicted cross section for a Dirac neutrino.

factor of ≈19 in comparison with the central neutrino density (3). Therefore taking (3) and (4) into account, we find that the density of heavy neutrinos in the solar neighborhood must satisfy the condition

$$n_{\rm Sun} \geqslant 3.3\times 10^6 n. \tag{5}$$

Let us apply the results obtained above to the experimental data on the direct search for WIMPs by WIMP–nucleus elastic scattering. Neutrinos scatter from nuclei by Z boson exchange, and therefore the axial coupling, which only produces small spin-dependent effects, can be neglected. In the nonrelativistic limit the neutrino cross section due to coherent scattering on nuclei is given by Ref. 5,

$$\sigma_{\rm elastic} \approx \frac{m^2 M^2}{2\pi (m+M)^2} G_F^2 \overline{Y}^2 \overline{N}^2, \tag{6}$$

where $\overline{N}=N-(1-\sin^2\theta_w)Z$; N, Z are the numbers of neutrons and protons, respectively; M is the mass of the target nucleus, G_F is the Fermi constant, and $\overline{Y}$ is the average hypercharge ($\overline{Y}\sim 1$). The nuclear degrees of freedom can be taken into account by a nuclear form factor.[6]

Figure 2 shows an exclusion plot in the cross section for coherent neutrino elastic interaction with Ge as obtained in underground experiments[7] versus the heavy neutrino mass. The theoretical cross section corresponding to heavy neutrino elastic interaction, taking into account the loss of coherence at high masses, also is shown in Fig. 2. However, this exclusion plot was obtained under the assumption that the heavy neutrinos constitute all of dark matter, with a density $\rho=0.3$ GeV·cm^{-3}, which is 5.3×10^{-25} g·cm^{-3}. In order to replace ρ by $\rho_{\rm Sun}$ and modify the exclusion plot to the ''real'' case we have to divide the values corresponding to the bound of the exclusion plot by the ratio

$$\xi = \rho_{\mathrm{Sun}}/\rho. \tag{7}$$

The new bound corresponding to the ''real'' neutrino density in the Galaxy is shown by the dashed line in Fig. 2. As we can see, in this case the existence of very heavy neutrinos is forbidden in the mass region

$$60\ \mathrm{GeV} \geqslant m \geqslant 290\ \mathrm{GeV}. \tag{8}$$

We note that (8) represents the minimal region excluded by Ge underground experiments, since this result was obtained by using a conservative set of values for the astrophysical and cosmological parameters. Changes from the parameter values chosen above can only extend the excluded region (8).

Previously less restrictive limits on mass of heavy neutrinos were obtained[3] from analysis of the spectrum of electrons in cosmic rays. However, that approach entailed uncertainties related, in particular, to the poor knowledge of the lifetime of cosmic rays in the Galaxy. Meanwhile, the bound (8) is essentially based on the sole assumption (but which is physically well motivated) of condensation of heavy neutrinos in the Galaxy.

Let us note that if the Higgs meson exists, the bound (8) does not exclude the possibility that the heavy neutrinos have a mass in the region $|M_H - m| \leqslant \Gamma_H$, where Γ_H is the width of Higgs meson, because in this case the *s*-channel annihilation $\nu\bar{\nu} \rightarrow H \rightarrow \ldots$ could reduce significantly the neutrino density in the Galaxy.[3]

Recently preliminary results on the underground search for WIMPs using the annual modulation signature with large-mass NaI(Tl) detectors have been published.[8] The overall analysis has shown that there is an indication of a single crystal response (however, as was mentioned by the authors,[8] only a very large exposure would make it possible to reach a firm conclusion).

In Fig. 3 we show qualitatively the region corresponding to the possible signal[8] with the use of the ''real'' neutrino density in the Galaxy according to Eq. (7). It was noted in Ref. 8 that the region of the signal is well embedded[6] in the minimal supersymmetric standard model estimates for the neutralino. However, as we see from Fig. 3, this case can also correspond to elastic scattering on the NaI nuclei of relic neutrinos with mass between 45 GeV and 50 GeV. This region is consistent with the present laboratory bound $m > 45$ GeV.

Confirmation of this event can be obtained in cosmic-ray experiments with the AMS spectrometer, which is in preparation for operation at the Alfa station. As was mentioned in Refs. 3, 9, and 10, the detection of an anomalous output of monochromatic positrons with energy above 45 GeV would be a clear signature of the annihilation of Dirac neutrinos in the galactic halo, because the direct annihilation of Majorana fermions into electron–positron pairs in the Galaxy is severely suppressed. On the other hand, detection of irregularity in the continuum spectrum of positrons could be an indication of annihilation of neutralinos.

Our approach is easily testable because we assumed only the simplest extended standard model with the 4th generation, without any *ad hoc* and fine-tuning parameters.

We also note that the search for heavy neutrinos at accelerators[11] in the reaction $e^+e^- \rightarrow \nu\bar{\nu}\gamma$ could provide the possibility of analyzing the mass region $m \sim M_Z/2$, which is difficult for an astrophysical investigation because of the low neutrino density, but can

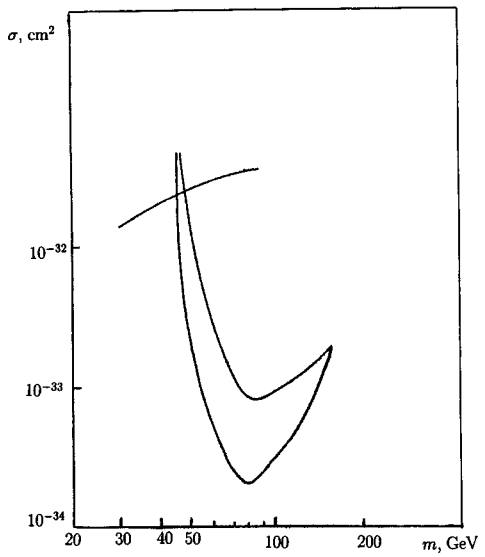

FIG. 3. Region corresponding qualitatively to the region of the possible dark matter signal[8] at $m>45$ GeV. The line intercepting the region shows the predicted cross section for a Dirac neutrino.

be important in relation with an event possibly observed in the DAMA experiment.[8] If heavy neutrinos exist there could be also an interesting hadronless signature for Higgs meson bremsstrahlung production at accelerators, $e^+e^-\to ZH\to Z\nu\overline{\nu}\to 1^+1^-\nu\overline{\nu}$, and this mode could be the dominant one.

In conclusion, we emphasize that it seems that only complex investigations including underground experiments, accelerator searches, and astrophysical investigations can clarify the physical nature of dark matter.

This work was supported by part by the Cosmion Science and Education Center. M. Yu. K. and R. V. K. are grateful to I Rome University for hospitality and support. We thank D. Prosperi for very interesting discussions.

[1] C. J. Copi, D. N. Schramm, and M. S. Turner, Science **267**, 192 (1995).
[2] K. Enquist, K. Kainulainen, and J. Maalampi, Nucl. Phys. B **317**, 647 (1989).
[3] D. Fargion, M. Yu. Khlopov, R. V. Konoplich, and R. Mignani, Phys. Rev. D **52**, 1828 (1995).
[4] Ya. B. Zeldovich, A. A. Klypin, M. Yu. Khlopov, and V. M. Chechetkin, Yad. Fiz. **31**, 1286 (1980) [Sov. J. Nucl. Phys. **31**, 664 (1980)].
[5] M. W. Goodman and E. Witten, Phys. Rev. D **31**, 3059 (1985).
[6] A. Bottino *et al.*, Phys. Lett. B **402**, 113 (1997).
[7] D. O. Caldwell, *Particles and Nuclear Astrophysics and Cosmology in the Next Millenium* (Snowmass 94 Proceedings), edited by E. W. Kolb and R. D. Peccei, World Scientific (1995), pp. 38–50.
[8] R. Bernabei *et al.*, http://xxx.lanl.gov/abs/astro-ph/9710290.
[9] M. S. Turner and F. Wilczek, Phys. Rev. D **42**, 1001 (1990).
[10] Yu. A. Golubkov and R. V. Konoplich, Preprint DESY-057 (1997).
[11] D. Fargion, M. Yu. Khlopov, R. V. Konoplich, and R. Mignani, Phys. Rev. D **54**, 4684 (1996).

Published in English in the original Russian journal. Edited by Steve Torstveit.

Cooling of ultracold neutrons during their long storage in a trap

L. Bondarenko, E. Korobkina, V. Morozov, and Yu. Panin
Kurchatov Institute Russian Science Center, 123182 Moscow, Russia

P. Geltenbort
Institute Laue-Langevin, 38042 Grenoble Cedex 9, France

A. Steyerl
Department of Physics, University of Rhode Island, Kingston, RI 02881, USA

(Submitted 9 June 1998; resubmitted 29 September 1998)
Pis'ma Zh. Éksp. Teor. Fiz. **68**, No. 9, 663–666 (10 November 1998)

We have observed the cooling of ultracold neutrons during their long storage in a trap, with a probability estimated as 1×10^{-6}/reflection and with an energy transfer of about 3 neV. © *1998 American Institute of Physics.* [S0021-3640(98)00221-7]

PACS numbers: 28.20.Cz

The main process of interaction of ultracold neutrons (UCNs) with matter is the elastic reflection from the vacuum/matter booundary[1,2] which permits storing UCNs in a trap almost up until their beta decay.[3–5] The probability of inelastic scattering of an ultracold neutron from a thermal lattice vibration is about 10^{-3}–10^{-6} per reflection into an energy range of $kT\sim2$–3 meV. Then the fraction of neutrons scattered into the UCN energy range $0-10^{-7}$ eV must be negligible. Nevertheless, the experimental data[6,7] indicate that UCNs with energies lower than the primary energy appear during UCN storage. This phenomenon could arise from an inelastic UCN reflection with energy loss. The present experiment was performed to search for UCN reflection with energy loss.

The UCN storage vessel (trap), see Fig. 1, had a cylindrical shape with a diameter of 65 cm and a flat bottom. It was placed inside a vacuum housing made of stainless steel. UCNs entered the vessel by passing over the edge of the vertical bottom cylinder wall of height $h_0=123$ mm, i.e., they overcame a gravity barrier $E_b=mgh_0$. During the filling the second, movable cylinder was at its maximum height, leaving a slit for UCN passage into the trap. After the filling this upper cylinder was moved down to close the gap and prevent UCNs from jumping back over the edge. In order to increase significantly the reflection frequency and to randomize the distribution of reflection angle the bottom of the vessel was covered with a layer of lead balls of diameter 3.5 mm. The balls and all the inner surfaces of the vessel were coated with Fomblin grease. The energy distribution of the UCN gas in the trap was cut off from above by the use of a polyethylene disk as an absorber, which was positioned at height h_f during filling and which was also used for scanning the spectrum after various storage times.

Thus the UCNs accumulating in the trap had energies over the range $E_b<E$

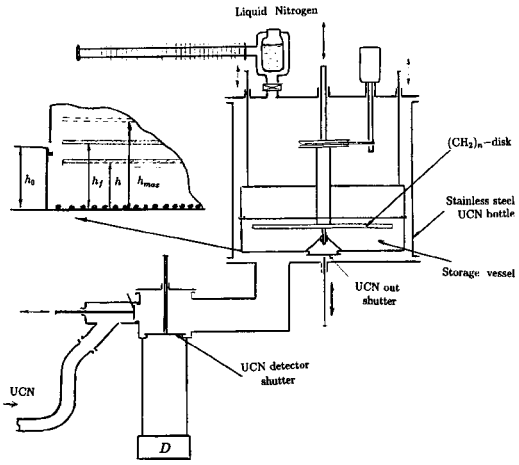

FIG. 1. The experimental layout; D shows the position of the UCN detector, h_0 is the entrance barrier height, h_f is the height of the position of the polyethylene $(CH_2)_n$ absorber disk during filling, and h and $h_{\max}$ are the height positions of the absorber disk during scanning and during the evolution time, respectively.

$<mgh_f$, i.e., the energy spectrum was rather narrow, with a width $\delta E = mg\,\delta h$, where $\delta h = h_f - h_0 \ll h_0$.

A measuring cycle consisted of the six successive steps:

1) filling of the trap at the disk height h_f ($T_f = 300$ s);

2) spectral precleaning (sharpening of the upper cutoff) while the filling gap was closed and the disk remained at height h_f ($T_p = 100$ s);

3) free spectral evolution over a period T_e. To eliminate interference with the UCN gas, the disk was at its maximum height $h_{\max} = 155$ mm ($T_e = 20,\ 620,\ 1200$ s);

4) scanning of the spectrum by lowering the disk to the variable height h and leaving it there sufficiently long for good spectral cleaning ($T_m = 200$ s);

5) emptying the trap and counting the surviving UCNs while the disk remained at height h (200 s);

6) measurement of the background (50 s).

This procedure gave the integral spectrum $N(h)$, which is related to the differential energy spectrum $F(x)$ as $N(h) = \int_0^h F(x)dx$. Here and below we use an energy scale expressed in height units (mm).

A precise investigation was carried out for the UCN spectra with $\delta h = 11.75$ mm. The measured storage time was $\tau = 680.0(9.5)$ s, and the calculated frequency f of collisions with the walls was about 20 Hz.

Figures 2 and 3 present the spectra $N(l)$, where $l = h - h_f$, for $T_e = 20$, 620, and 1200 s, which were normalized to the value $N_{20}(l)$ measured for $T_e = 20$ s, with corrections for the exponential losses determined by τ. All of the spectra $N(l)$ were fitted using the Gaussian cumulative distribution function (GCDF), which places the center of the energy distribution x and its variance σ^2. The criterion of confidence $\sqrt{\chi^2}$ of the fit was

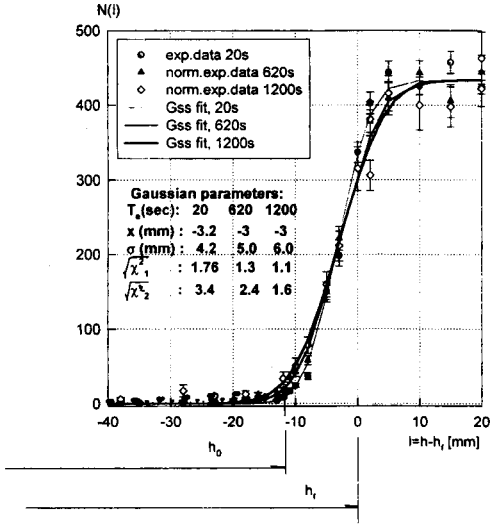

FIG. 2. Measured spectra $N(l)$ with GCDF fit curves. In Table I the parameter x is the center position of the Gaussian, σ^2 is its variance, and the criterion of confidence: $\sqrt{\chi_1^2}$ is calculated for $h>h_0$ and $\sqrt{\chi_2^2}$ is calculated for the entire h range.

near unity only for the energy range above the gravity barrier E_b, while for energies $E<E_b$, i.e., $h<h_0$, it was much greater than unity. Therefore for this energy range a parabolic fit was used.

Figure 2 clearly shows that the UCN spectra had no shift but became broader in the central part that is well fitted by the GCDF. The origin of this broadening $\Delta\sigma$ could be

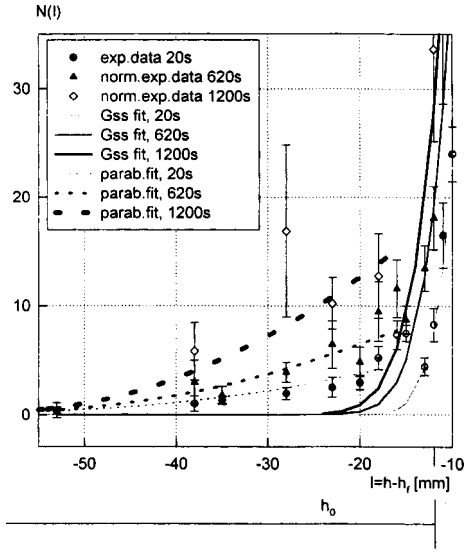

FIG. 3. Measured spectra $N(l)$ with GCDF and parabolic fit curves.

TABLE I. The result of the estimates for the cooling probability w.

T_e (s)	20	620	1200
T (s)	270(100)	870(100)	1450(100)
T/270 s	1	3.2(1.2)	5.37(2.02)
p(%)	0.95(23)	1.74(46)	3.21(69)
$w(10^{-6})$	1.8(1.3)	1.0(3)	1.1(3)

either wall vibration or any unknown process with a small energy transfer per collision.

The spectral broadening due to wall vibration can be estimated in a ''diffusion'' approach, $\Delta\sigma=\sqrt{2DT_e}$ (Ref. 8). The diffusion coefficient $D=(\Delta E)^2 f/2$ was obtained for an energy transfer per collision ΔE obtained from the estimate $\Delta E/E\approx 8\Delta v/3\pi v$, where Δv is the amplitude of the wall velocity and v is the neutron velocity. The maximum value of $\Delta\sigma$ was $\approx$1 mm for $T_e=1200$ s, $v=160$ cm/s, and $f=20$ Hz, and the maximum measured value of Δv was 100 μm/s. Comparison of this value with the experimental value, $\Delta\sigma=1.8$ mm, shows that the spectral broadening could be partly explained by vibration.

However, the shape of the UCN spectra below the input barrier h_0 cannot be explained by trap wall vibration. Figure 3 shows that the relative fraction of UCNs with energy $h<h_0$ increased with increasing evolution time in the trap. The integral spectra of UCNs could not be fitted by the GCDF in this range. Thus UCNs with energies noticeably lower than E_b could appear only as a result of a rare process of UCN cooling with an energy transfer per reflection of $\Delta h\approx 20-30$ mm$\geqslant\delta h$. Probably a similar process was observed in an earlier experiment,[7] where it was not interpreted.

Let us estimate the cooling probability w for the range below $l_1=-18$ mm, where the GCDF contribution is negligible. In Table I the value $w=p/f/T$ was estimated on the assumption of a rare process occurring in one reflection. The real time for UCN cooling T could be estimated as the sum $T\approx T_e+T_p+aT_f+bT_m$, where the coefficients $a,b<1$. The uncertainty of T was determined by the uncertainties of these coefficients. The factor $p=\Delta N/N$, where ΔN is the number of UCNs with $l<l_1$, and N is the total number of UCNs.

Table I confirms the linear dependence of p on the real cooling time T, with a criterion of confidence $\sqrt{\chi^2}=1.1$. In the case of any systematic effect, for instance, bad spectrum cleaning by the absorber disk, the value of p should be equal to a const(T). This hypothesis corresponds to $\sqrt{\chi^2}=2.3$. The weighted mean value of the cooling probability is equal to $\overline{w}=1.1(2)\times 10^{-6}$.

The observed cooling could not be explained in framework of the standard theory.[1,2] It contradicts the traditional point of view that UCN reflection is an absolutely elastic process and calls for a more-detailed investigation.

The authors are pleased to thank S. T. Belyaev for a very fruitful discussion of the result of this work, and the staff of the ILL reactor, where this experiment was performed.

This work was carried out with the support of the Russian Fund for Fundamental Research through Grant 98-02-16774.

[1] F. L. Shapiro, ''*Ultra-Cold Neutrons*'' [in Russian], Preprint JINR R3-7135, Dubna (1973).
[2] R. Golub, D. Richardson, and S. Lamoreaux, *Ultra-Cold Neutrons*, Adam Hilger, Bristol, 1991.
[3] W. Mampe, P. Ageron *et al.*, Nucl. Instrum. Methods Phys. Res. A **284**, 111 (1989).
[4] A. G. Kharitonov, V. V. Nesvizhevsky, A. P. Serebrov *et al.*, Nucl. Instrum. Methods Phys. Res. A **284**, 98 (1989).
[5] W. Mampe, L. Bondarenko, V. Morozov *et al.*, JETP Lett. **57**, 82 (1993).
[6] L. Bondarenko, E. Korobkina, V. Morozov *et al.*, ILL˙ Experimental Rep. # 3-14-44 (1997).
[7] Yu. Kosvintsev, Yu. Kushnir, and V. I. Morozov, Zh. Éksp. Teor. Fiz. **77**, 1277 (1979) [Sov. Phys. JETP **50**, 642 (1979)].
[8] Ya. B. Zel'dovich and A. D. Myshkis, *Elements of Applied Mathematics* [in Russian], Nauka, Moscow, 1973, p. 230.

Published in English in the original Russian journal. Edited by Steve Torstveit.

Diffractive vector mesons beyond the *s*-channel helicity conservation

E. V. Kuraev
Laboratory for Theoretical Physics, JINR, 141980 Dubna, Moscow Region, Russia

N. N. Nikolaev
IKP(Theorie), KFA Jülich, D-52428 Jülich, Germany; L. D. Landau Institute of Theoretical Physics, Russian Academy of Sciences, 117334 Moscow, Russia

B. G. Zakharov
L. D. Landau Institute of Theoretical Physics, Russian Academy of Sciences, 117334 Moscow, Russia

(Submitted 1 October 1998)
Pis'ma Zh. Éksp. Teor. Fiz. **68**, No. 9, 667–673 (10 November 1998)

We derive a full set, and determine the twist, of helicity amplitudes for diffractive production of light to heavy vector mesons in deep inelastic scattering. For large Q^2 all helicity amplitudes but the double-flip are calculable in perturbative QCD and are proportional to the gluon structure function of the proton at a similar hardness scale. We find a substantial breaking of the *s*-channel helicity conservation, which must persist in real photoproduction also. © *1998 American Institute of Physics.* [S0021-3640(98)00321-1]

PACS numbers: 13.60.Le, 12.20.Ds, 14.40.−n

Diffractive virtual photoproduction of vector mesons $\gamma^*+p\to V+p'$, where $V=\rho_0,\omega,\phi,J/\Psi,\Upsilon$ in deep inelastic scattering (DIS) at small $x=(Q^2+m_V^2)/(W^2+Q^2)$ is a testing ground of ideas on the QCD pomeron exchange and light-cone wave function (LCWF) of vector mesons (Refs. 1–5; for a recent review see Ref. 6; for the kinematics see Fig. 1; $Q^2=-q^2$ and $W^2=(p+q)^2$ are standard DIS variables). It is a self-analyzing process because the helicity amplitudes can be inferred from vector meson decay angular distributions.[7] The property of *s*-channel helicity conservation (SCHC) and the dominance of the transitions $\gamma_L^*\to V_L$ and $\gamma_T^*\to V_T$ with $R=\sigma_L/\sigma_T\approx Q^2/m_V^2$ are shared by nearly all models (L and T stand for the longitudinal and transverse polarizations). The nonperturbative contributions to σ_T tame the rise of R with Q^2 (Refs. 2 and 4), but still the theoretical predictions seem to be systematically higher than the experimentally determined values of R. However, the experimental data analyses suffer from the unwarranted assumption of exact SCHC,[6] which needs theoretical scrutiny. We report here a derivation of the full set of helicity amplitudes for the transitions $\gamma_L^*\to V_L$, $\gamma_L^*\to V_T$, $\gamma_T^*\to V_T$, $\gamma_T^*\to V_L$ for all flavors and small to moderate momentum transfer $\mathbf{\Delta}$ within the diffraction cone. We find substantial *s*-channel helicity-nonconserving (SCHNC) effects, similar to the SCHNC LT interference found earlier[8] by Pronyaev and

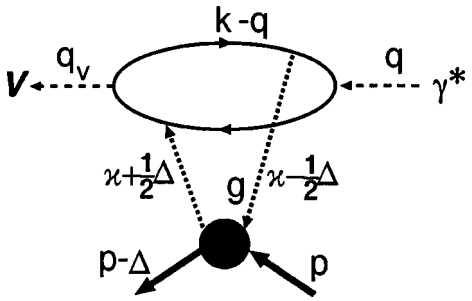

FIG. 1. One of the four Feynman diagrams for the vector meson production $\gamma^* p \to V p'$ via QCD two-gluon pomeron exchange.

two of the present authors (N.N.N. and B.G.Z.) for diffraction $\gamma^* p \to p' X$ into continuum states X.

The leading-log1/x (LL1/x) pQCD diagrams for vector meson production are shown in Fig. 1. We treat vector mesons as $q\bar{q}$ states with the $Vq\bar{q}$ vertex $\Gamma_V V_\mu \bar{u}\gamma_\mu u$. At small x it is sufficient to compute the imaginary part of the amplitude, the real part is a small correction which can readily be reconstructed from analyticity[4] and we will not discuss it further. We use the standard Sudakov expansion of all the momenta in the two light-cone vectors

$$p' = p - q\frac{p^2}{s}, \quad q' = q + p'\frac{Q^2}{s},$$

such that $q'^2 = p'^2 = 0$ and $s = 2p' \cdot q'$, and the two-dimensional transverse component: $k = zq' + yp' + k_\perp$, $\kappa = \alpha q' + \beta p' + \kappa_\perp$, $\Delta = \gamma p' + \delta q' + \Delta_\perp$, and for the final vector meson $q_V = q + \Delta = q' + (m_V^2 + \mathbf{\Delta}^2/s)\, p' + \Delta_\perp$ (hereafter $\mathbf{k}, \mathbf{\Delta}, \ldots$ always stand for $k_\perp, \Delta_\perp$ etc.). As usual, only the so-called nonsense components in Gribov's decomposition of the gluon propagators contribute in the high-energy limit,

$$D_{\mu\nu}(k) = \frac{2p'_\mu q'_\nu}{sk^2},$$

so that in the upper blob the amplitude $R_{\mu\nu\rho\sigma}$ of the subprocess $g_\mu \gamma^*_\sigma \to q\bar{q} \to g'_\nu V_\rho$ enters in the form $I(\gamma^* \to V) \propto p'_\mu p'_\nu R_{\mu\nu\rho\sigma} V^*_\rho e_\sigma$. The vertex function Γ is related to the radial LCWF of the $q\bar{q}$ Fock state of the vector meson as

$$\psi_V(z, \mathbf{k}) = \frac{\Gamma_V(z, \mathbf{k})}{D(m_V^2, z, \mathbf{k})}, \tag{1}$$

where $D(\mathbf{k}^2) = \mathbf{k}^2 + m_q^2 - z(1-z)m_V^2$. For the parametrizations of the LCWFs of vector mesons based on the technique of Ref. 9 the reader is referred to Ref. 4. The corresponding quantity for photons, $\psi_\gamma(z, \mathbf{k}) = 1/D(-Q^2, z, \mathbf{k})$, differs only by the substitution $\Gamma_\gamma(z, \mathbf{k}) = 1$ and $m_V^2 \to -Q^2$. To LL1/x the lower blob is related to the unintegrated gluon density matrix $\mathcal{F}(x, \boldsymbol{\kappa}, \mathbf{\Delta})$.[5,10,11] After the standard elimination of the Sudakov parameters

y,β etc. from the on-mass-shell condition, for instance, $(k-q)^2=-sy(1-z)-\mathbf{k}^2-Q^2(1-z)=m_q^2$, the virtual photoproduction amplitude takes the form

$$A(x,Q^2,\boldsymbol{\Delta})=is\frac{C_F N_c c_V\sqrt{4\pi\alpha_{em}}}{2\pi^2}$$

$$\times\int_0^1 dz\int d^2\mathbf{k}\int\frac{d^2\boldsymbol{\kappa}}{\boldsymbol{\kappa}^4}\alpha_S(\max\{\kappa^2,\mathbf{k}^2+m_V^2\})\mathcal{F}(x,\boldsymbol{\kappa},\boldsymbol{\Delta})I(\gamma^*\to V),\quad(2)$$

where $N_c=3$ is the number of colors, $C_F=(N_c^2-1)/2N_c$ is the Casimir operator, $C_V=1/\sqrt{2},1/3\sqrt{2},1/3,2/3$ for the $\rho^0,\omega^0,\phi^0,J/\Psi$ mesons, and α_S and α_{em} are the strong and electromagnetic couplings, respectively. The dependence of $\mathcal{F}(x,\boldsymbol{\kappa},\boldsymbol{\Delta})$ on the variable $\boldsymbol{\Delta}\boldsymbol{\kappa}$ corresponds to the subleading BFKL singularities[11] and can be neglected. For small $\boldsymbol{\Delta}$ within the diffraction cone

$$\mathcal{F}(x,\boldsymbol{\kappa},\boldsymbol{\Delta})=\frac{\partial G(x,\kappa^2)}{\partial\log\kappa^2}\exp\left(-\frac{1}{2}B_{3\mathrm{IP}}\boldsymbol{\Delta}^2\right),\quad(3)$$

where $\partial G/\partial\log\kappa^2$ is the conventional unintegrated gluon structure function and, modulo to a slow Regge growth, the diffraction cone $B_{3\mathrm{IP}}\sim 6\ \mathrm{GeV}^{-2}$ (Ref. 5). The familiar polarization vectors for virtual photons are

$$e_L=\frac{1}{Q}\left(q'+\frac{Q^2}{s}p'\right),\quad e_T=e_\perp,$$

whereas for vector mesons

$$V_T=V_\perp+\frac{2(\mathbf{V}_\perp\cdot\boldsymbol{\Delta})}{s}(p'-q'),\quad V_L=\frac{1}{m_V}\left(q'+\frac{\boldsymbol{\Delta}^2-m_V^2}{s}p'+\Delta_\perp\right),\quad(4)$$

such that $(V_TV_L)=(V_Tq_V)=(V_Lq_V)=0$. Because of the small factor $1/s$ it is tempting to neglect the component $\propto p'$ in V_T but that would be entirely erroneous. Indeed, closer inspection of the evaluation of $I(\gamma^*\to V)$ shows that $p'_\mu p'_\nu R_{\mu\nu\rho\sigma}p'_\rho e_\sigma\propto sp'_\mu p'_\nu R_{\mu\nu\rho\sigma}V^*_{\perp,\rho}e_\sigma$. The same is true of the contribution from the component $\propto\Delta_\perp$ in V_L.

It is convenient to define

$$\boldsymbol{\Psi}_{\gamma,V}(\mathbf{k})=\mathbf{k}\psi_{\gamma,V}(z,\mathbf{k}),\ \chi_\gamma(z,\mathbf{k})=[\mathbf{k}^2+m_q^2-z(1-z)Q^2]\psi_\gamma(z,\mathbf{k}),$$

$$\chi_V(z,\mathbf{k})=[\mathbf{k}^2+m_q^2+z(1-z)m_V^2]\psi_V(z,\mathbf{k})$$

and

$$\eta_\gamma=\psi_\gamma(z,\mathbf{k})-\psi_\gamma\left(z,\mathbf{k}-\boldsymbol{\kappa}+\frac{1}{2}\boldsymbol{\Delta}\right),\quad(5)$$

$$\eta_V=\psi_V(z,\mathbf{k}+(1-z)\boldsymbol{\Delta})-\psi_V\left(z,\mathbf{k}-\boldsymbol{\kappa}+\frac{1}{2}(1-2z)\boldsymbol{\Delta}\right),\quad(6)$$

$$\varphi_\gamma=\chi_\gamma(z,\mathbf{k})-\chi_\gamma\left(z,\mathbf{k}-\boldsymbol{\kappa}+\frac{1}{2}\boldsymbol{\Delta}\right)=-2z(1-z)Q^2\eta_\gamma,\quad(7)$$

$$\varphi_V=\chi_V(z,\mathbf{k}+(1-z)\boldsymbol{\Delta})-\chi_V\left(z,\mathbf{k}-\boldsymbol{\kappa}+\frac{1}{2}(1-2z)\boldsymbol{\Delta}\right), \tag{8}$$

$$\boldsymbol{\phi}_\gamma=\boldsymbol{\Psi}_\gamma(z,\mathbf{k})-\boldsymbol{\Psi}_\gamma\left(z,\mathbf{k}-\boldsymbol{\kappa}+\frac{1}{2}\boldsymbol{\Delta}\right), \tag{9}$$

$$\boldsymbol{\phi}_V=\boldsymbol{\Psi}_V(z,\mathbf{k}+(1-z)\boldsymbol{\Delta})-\boldsymbol{\Psi}_V\left(z,\mathbf{k}-\boldsymbol{\kappa}+\frac{1}{2}(1-2z)\boldsymbol{\Delta}\right), \tag{10}$$

$$\begin{aligned}\Phi_2=&\psi_\gamma(z,\mathbf{k}-(1-z)\boldsymbol{\Delta})-\psi_\gamma\left(z,\mathbf{k}-\boldsymbol{\kappa}-\frac{1}{2}(1-2z)\boldsymbol{\Delta}\right),\\&-\psi_\gamma\left(z,\mathbf{k}+\boldsymbol{\kappa}-\frac{1}{2}(1-2z)\boldsymbol{\Delta}\right)+\psi_\gamma(z,\mathbf{k}+z\boldsymbol{\Delta}),\end{aligned} \tag{11}$$

$$\begin{aligned}\Phi_1=&\boldsymbol{\Psi}_\gamma(z,\mathbf{k}-(1-z)\boldsymbol{\Delta})-\boldsymbol{\Psi}_\gamma\left(z,\mathbf{k}-\boldsymbol{\kappa}-\frac{1}{2}(1-2z)\boldsymbol{\Delta}\right),\\&-\boldsymbol{\Psi}_\gamma\left(z,\mathbf{k}+\boldsymbol{\kappa}-\frac{1}{2}(1-2z)\boldsymbol{\Delta}\right)+\boldsymbol{\Psi}_\gamma(z,\mathbf{k}+z\boldsymbol{\Delta}).\end{aligned} \tag{12}$$

Then the integrands $I(\gamma^*\to V)$ in (2) can be cast in a form which emphasizes the $V\leftrightarrow\gamma$ symmetry nicely:

$$I(\gamma_L^*\to V_L)=\frac{1}{Qm_V}\varphi_\gamma\varphi_V=-\frac{2Q}{m_V}z(1-z)\Phi_2[m_q^2+\mathbf{k}^2+z(1-z)m_V^2]\psi_V(z,\mathbf{k}), \tag{13}$$

$$\begin{aligned}I(\gamma_T^*\to V_T)=&(\mathbf{V}^*\cdot\mathbf{e})[m_q^2\eta_V\eta_\gamma+(\boldsymbol{\phi}_V\cdot\boldsymbol{\phi}_\gamma)]\\&+(1-2z)^2(\boldsymbol{\phi}_\gamma\cdot\mathbf{e})(\boldsymbol{\phi}_V\cdot\mathbf{V}^*)-(\boldsymbol{\phi}_V\cdot\mathbf{e})(\boldsymbol{\phi}_\gamma\cdot\mathbf{V}^*)\\=&\{(\mathbf{V}^*\cdot\mathbf{e})[m_q^2\Phi_2+(\mathbf{k}\cdot\boldsymbol{\Phi}_1)]+(1-2z)^2(\mathbf{V}^*\cdot\mathbf{k})(\mathbf{e}\cdot\boldsymbol{\Phi}_1)\\&-(\mathbf{e}\cdot\mathbf{k})(\mathbf{V}^*\cdot\boldsymbol{\Phi}_1)\}\psi_V(z,\mathbf{k}),\end{aligned} \tag{14}$$

$$I(\gamma_T^*\to V_L)=\frac{(1-2z)}{m_V}(\boldsymbol{\phi}_\gamma\cdot\mathbf{e})\varphi_V=\frac{(1-2z)}{m_V}(\mathbf{e}\cdot\boldsymbol{\Phi}_1)[m_q^2+\mathbf{k}^2+z(1-z)m_V^2]\psi_V(z,\mathbf{k}), \tag{15}$$

$$I(\gamma_L^*\to V_T)=\frac{(1-2z)}{Q}\varphi_\gamma(\mathbf{V}^*\cdot\boldsymbol{\phi}_V)=-2Qz(1-z)(1-2z)(\mathbf{V}^*\cdot\mathbf{k})\Phi_2\psi_V(z,\mathbf{k}). \tag{16}$$

We consistently keep the quark mass, so that our derivation holds from light to heavy vector mesons.

After simple shifts of the integration variables to the common argument of the vector meson LCWF, $I(\gamma^*\to V)$ can also be cast in the second form shown in (13)–(16). This second form emphasizes the close analogy, discussed in Refs. 8, 10, and 12, between the amplitudes of vector meson production and diffraction into the continuum, the major difference being the emergence of $\psi_V(z,\mathbf{k})$ instead of the plane WF. The second form is also convenient for the derivation of the $1/Q^2$ expansion, i.e., of the twist, of the

helicity amplitudes. To this end we notice that $\psi_V(z,\mathbf{k})$ varies on a hadronic scale $k^2 \sim R_V^{-2}$, where R_V is the radius of the vector meson, whereas $\psi_\gamma(z,\mathbf{k})$ is a slow function which varies on a large pQCD scale

$$\overline{Q}^2 = m_q^2 + z(1-z)Q^2, \tag{17}$$

which allows a systematic twist expansion in powers of $1/\overline{Q}^2$ for Δ within the diffraction cone. In all cases but the double helicity flip the dominant twist amplitudes come from the leading $\log\overline{Q}^2$ (LL$\overline{Q}^2$) region of $\mathbf{k}^2 \sim R_V^{-2}$, $\boldsymbol{\Delta}^2 \ll \boldsymbol{\kappa}^2 \ll \overline{Q}^2$. After some algebra in (13)–(16) we find

$$I(\gamma_L^* \to V_L) = -\frac{Q}{m_V}\frac{4z(1-z)[m_q^2 + \mathbf{k}^2 + z(1-z)m_V^2]}{\overline{Q}^4}\psi_V(z,\mathbf{k})\boldsymbol{\kappa}^2, \tag{18}$$

$$I(\gamma_T^* \to V_T; \lambda_V = \lambda_\gamma) = 2(\mathbf{V}^* \cdot \mathbf{e})\frac{m_q^2 + 2[z^2 + (1-z)^2]\mathbf{k}^2}{\overline{Q}^4}\psi_V(z,\mathbf{k})\boldsymbol{\kappa}^2, \tag{19}$$

$$I(\gamma_L^* \to V_T) = -8\frac{(\mathbf{V}^* \cdot \boldsymbol{\Delta})Q}{\overline{Q}^2}\frac{z(1-z)(1-2z)^2}{\overline{Q}^4}\mathbf{k}^2\psi_V(z,\mathbf{k})\boldsymbol{\kappa}^2, \tag{20}$$

$$I(\gamma_T^* \to V_L) = -2\frac{(\mathbf{e} \cdot \boldsymbol{\Delta})}{m_V}\frac{[m_q^2 + \mathbf{k}^2 + z(1-z)m_V^2](1-2z)^2}{\overline{Q}^4}\psi_V(z,\mathbf{k})\boldsymbol{\kappa}^2. \tag{21}$$

Here we split explicitly the amplitude (14) into the SCHC helicity-nonflip component (19) and SCHNC double-helicity-flip component

$$I(\gamma_T^* \to V_{T'}; \lambda_V = -\lambda_\gamma) = 2(\mathbf{V}^* \cdot \boldsymbol{\Delta})(\mathbf{e} \cdot \boldsymbol{\Delta})\frac{z(1-z)}{\overline{Q}^4}\left[6(1-2z)^2\frac{\boldsymbol{\kappa}^2}{\overline{Q}^2} + 1\right]\mathbf{k}^2\psi_V(z,\mathbf{k}). \tag{22}$$

In all cases when $I(\gamma^* \to V) \propto \boldsymbol{\kappa}^2$ and the LL$\overline{Q}^2$ approximation is in play, the gluon structure function enters the integrand in the form

$$\int^{\overline{Q}^2}\frac{d\boldsymbol{\kappa}^2}{\boldsymbol{\kappa}^2}\frac{\partial G(x,\boldsymbol{\kappa}^2)}{\partial \log \boldsymbol{\kappa}^2} = G(x,\overline{Q}^2) \tag{23}$$

and after the z integration one finds that the helicity amplitudes will be proportional to $\alpha_S(Q_V^2)G(x,Q_V^2)$, where the pQCD hardness scale

$$Q_V^2 \sim (0.1\text{–}0.2)(Q^2 + m_V^2) \tag{24}$$

can depend on the helicities because of the different end-point contributions from $z \to 0$ and $z \to 1$, where the running hardness $\overline{Q}^2$ is small.[2,4] This issue and the sensitivity of the helicity amplitudes to the LCWF of vector mesons will be discussed elsewhere. Here we cite our results for the dominant twist SCHC and single-flip SCHNC amplitudes $A_{\lambda_V\lambda_\gamma}$ in the helicity basis:

$$A_{0L} \propto \frac{Q}{m_V}\frac{\alpha_S(Q_V^2)}{(Q^2 + m_V^2)^2}G(x,Q_V^2), \tag{25}$$

$$A_{\pm\pm}\propto\frac{\alpha_S(Q_V^2)}{(Q^2+m_V^2)^2}G(x,Q_V^2), \tag{26}$$

$$A_{\pm L}\propto\frac{\Delta}{m_V}\frac{\alpha_S(Q_V^2)}{(Q^2+m_V^2)^2}G(x,Q_V^2), \tag{27}$$

$$A_{0\pm}\propto\frac{Q}{m_V}\frac{m_V\Delta}{Q^2+m_V^2}\frac{\alpha_S(Q_V^2)}{(Q^2+m_V^2)^2}G(x,Q_V^2). \tag{28}$$

First, all of the above amplitudes are pQCD calculable for large Q^2 and/or heavy vector mesons. Second, the factor Q/m_V in the longitudinal photon amplitudes (25) and (27) is a generic consequence of gauge invariance, irrespective of the detailed production dynamics. Third, the longitudinal Fermi momentum of quarks is $k_z\sim 1/2m_V(2z-1)$, and it is obvious from Eqs. (20) and (21) that single helicity flip requires a longitudinal Fermi motion of quarks and vanishes in the nonrelativistic limit. Similarly, double helicity flip requires the transverse Fermi motion of quarks. Fourth, the leading SCHNC effect is an interference of A_{0L} and $A_{0\pm}$, and the first experimental indications for that have been reported recently.[13] We notice here that a duality relation[14] holds between the twist of $\propto A_{0L}A_{0\pm}$ and that of the LT interference structure function F_{LT}^D derived in Ref. 8. The issue of duality for SCHNC diffractive DIS will be discussed elsewhere. Fifth, excitation of transverse mesons by longitudinal photons is of higher twist compared to excitation of longitudinal mesons by transverse photons.

In contrast to the above, the dominant twist double-helicity-flip amplitude comes from the nonleading-log$\overline{Q}^2$ term 1 in the square brackets in (22) and is proportional to

$$\int^{\overline{Q}^2}\frac{d\kappa^2}{\kappa^4}\frac{\partial G(x,\kappa^2)}{\partial\log\kappa^2}\sim\frac{1}{\mu_G^2}G(x,\mu_G^2), \tag{29}$$

where a soft scale $\mu_G\sim 0.7$–1 GeV is set by the inverse radius of propagation of perturbative gluons. Precisely the same nonperturbative quantity (29) describes the contribution from the $\gamma^*\to V$ transition vertex to the diffraction slope for helicity-nonflip amplitudes; for more discussion see Ref. 5. Then from Eq. (21) we find

$$A_{\pm\mp}\propto\Delta^2\frac{\alpha_S(Q_V^2)}{(Q^2+m_V^2)^2}\left[\frac{6G(x,Q_V^2)}{Q^2+m_V^2}\frac{\langle k_z^2\rangle}{4m_V^2}+\frac{G(x,\mu_G^2)}{\mu_G^2}\right], \tag{30}$$

where the leading log$\overline{Q}^2$ amplitude is of higher twist. Such a mismatch of the twist and leading log$\overline{Q}^2$ regime in diffractive DIS is *dejà vu*: the leading twist σ_T is soft-gluon dominated, whereas the full-fledged log$\overline{Q}^2$ is at work for the higher twist σ_L (Refs. 10 and 14). What is new in (30) is that the two regimes mix in one and the same helicity amplitude. The soft-gluon exchange dominance of the leading twist double helicity flip was noticed recently by Ivanov and Kirschner.[15]

Finally, we emphasize that nonvanishing single- and double-helicity-flip amplitudes (27) and (29) do not require the applicability of pQCD and can best be searched for in real photo- or electroproduction at small $Q^2\lesssim m_V^2$.

When this manuscript was in preparation, we learned of the related work by Ivanov and Kirschner (IK).[15] IK considered only light quarkonia and put $m_q=0$, our results are applicable from light to heavy quarkonia. While we agree with IK on the twist of helicity amplitudes, he have differences in the form of $I(\gamma^*\to V)$. For instance, the $\gamma^*\leftrightarrow V$ symmetry is not manifest in the IK formulas. The apparent source of differences is the unwarranted omission by IK of terms $\propto\Delta$ in the polarization vectors of the vector mesons.

To summarize, we have presented a perturbative QCD derivation of the helicity amplitudes for diffractive electroproduction of vector mesons. Unlike that of IK,[15] our derivation holds for light to heavy vector mesons, and our formulas are also applicable to the production of radially excited states. We have determined the twist of the *s*-channel helicity-nonconserving amplitudes. With the exception of the double-flip, all the helicity amplitudes are proportional to the gluon structure function of the proton at a similar pQCD hardness scale (24). Our principal conclusions as to the presence of substantial *s*-channel helicity-nonconserving effects hold beyond perturbative QCD and are applicable also to real photoproduction.

The authors are grateful to S. Gevorkyan for discussions, to D. Ivanov for useful correspondence on Ref. 15, to K. Piotrzkowski for information on presentations[13] at the recent ICHEP-98 in Vancouver, and to I. Akushevich for pointing out a misprint. E.V.K. is grateful to Institute für Kernphysik of Forschungszentrum Jülich for hospitality. The work of E.V.K. and B.G.Z. has been supported partly by INTAS Grants #93-0239 and #96-0597, respectively.

[1] N. N. Nikolaev, Comments Nucl. Part. Phys. **21**, 41 (1992); B. Z. Kopeliovich, J. Nemchik, N. N. Nikolaev, and B. G. Zakharov, Phys. Lett. B **309** 179 (1993); B. Z. Kopeliovich, J. Nemchik, N. N. Nikolaev, and B. G. Zakharov, Phys. Lett. B **B324**, 469 (1994).
[2] J. Nemchik, N. N. Nikolaev, and B. G. Zakharov, Phys. Lett. B **341**, 228 (1994).
[3] D. Yu. Ivanov, Phys. Rev. D **53**, 3564 (1996); I. F. Ginzburg and D. Yu. Ivanov, Phys. Rev. D **54**, 5523 (1996); I. Ginzburg, S. Panfil, and V. Serbo, Nucl. Phys. B **284**, 685 (1987); **296**, 569 (1988).
[4] J. Nemchik, N. N. Nikolaev, E. Predazzi, and B. G. Zakharov, Z. Phys. C **75**, 71 (1997).
[5] J. Nemchik, N. N. Nikolaev, E. Predazzi *et al.*, Zh. Éksp. Teor. Fiz. **113**, 1930 (1998) [JETP **86**, 1054 (1998)].
[6] J. Crittenden, *Springer Tracts in Modern Physics*, Vol. 140, Springer, Berlin, Heidelberg, 1997.
[7] K. Schilling and G. Wolf, Nucl. Phys. B **61**, 381 (1973).
[8] N. N. Nikolaev and B. G. Zakharov, in *Deep Inelastic Scattering and QCD (DIS97)*, Proc. of 5th Intern. Workshop, Chicago, Ill., USA, April 14–18, 1997, AIP Conf. Proc. 0094-243X 1997, Issue.407, edited by J. Repond and D. Krakauer, pp. 445–455; A. Pronyaev, http://xxx.lanl.gov/abs/hep-th/9808432, to be published in the Proc. of 6th Intern. Workshop on Deep Inelastic Scattering and QCD (DIS98), Brussels, Belgium, April 4–8, 1998.
[9] M. V. Terent'ev, Yad. Fiz. **24**, 207 (1976) [Sov. J. Nucl. Phys. **24**, 106 (1976)]; V. B. Berestetskiĭ and M. V. Terentev, Yad. Fiz. **25**, 653 (1977) [Sov. J. Nucl. Phys. **5**, 347 (1977)].
[10] N. N. Nikolaev and B. G. Zakharov, Phys. Lett. B **332**, 177 (1994); Z. Phys. C **53**, 331 (1992).
[11] L. N. Lipatov, Zh. Éksp. Teor. Fiz. **90**, 1536 (1986) [Sov. Phys. JETP **63**, 904 (1986)]; L. N. Lipatov, in *Perturbative Quantum Chromodynamics*, edited by A. H. Mueller, World Scientific, 1989; E. A. Kuraev, L. N. Lipatov and S. V. Fadin, Zh. Éksp. Teor. Fiz. **71**, 840 (1976) [Sov. Phys. JETP **44**, 443 (1976)]; Zh. Éksp. Teor. Fiz. **72**, 377 (1977) [Sov. Phys. JETP **45**, 199 (1977)].
[12] N. N. Nikolaev, A. V. Pronyaev, and B. G. Zakharov, http://xxx.lanl.gov/abs/hep-th/9809444, JETP Lett. **68**, 634 (1998).
[13] The reports by ZEUS, H1 and HERMES collaborations at the 29th International Conference on High Energy Physics (ICHEP-98), 23–29 July 1998, Vancouver, Canada, can be accessed from: (ZEUS) http://www-zeus.desy.de/conferences98/ichep98papers/diff/add-792-793/add.ps.gz, (H1) http://www-h1.desy.de/h1/www/

psfiles/confpap/vancouver98/abstracts/564-marage-paper.ps, (HERMES) http://ichep98.triumf.ca/private/convenors/body.asp.abstractID=887.
[14] M. Genovese, N. N. Nikolaev, and B. G. Zakharov, Phys. Lett. B **380**, 213 (1996).
[15] D. Ivanov and R. Kirschner, http://xxx.lanl.gov/abs/hep-ph/9807324.

Published in English in the original Russian journal. Edited by Steve Torstveit.

Induced γ-ray fluorescence of isomeric nuclei in a magnetic trap

A. A. Andreev and Yu. V. Rozhdestvenskiĭ
S. I. Vavilov State Optical Institute, 199034 St. Petersburg, Russia

K. Yu. Platonov
State Technical University, St. Petersburg, Russia

(Submitted 7 October 1998)
Pis'ma Zh. Éksp. Teor. Fiz. **68**, No. 9, 674–680 (10 November 1998)

Gamma-ray fluorescence induced in isomeric nuclei in a magnetic trap by x radiation from a laser plasma is studied. It is shown that under these conditions it is possible to obtain a γ-ray pulse with a duration of 100 ps and energy 10^{-5} J. © *1998 American Institute of Physics.* [S0021-3640(98)00421-6]

PACS numbers: 29.30.Kv, 23.20.Lv, 52.55.Lf

The production of induced fluorescence in resonant media is a necessary step in the development of lasers. In this case, as the wavelength of the radiation decreases, substantial difficulties in observing any induced effects arise, primarily because of the need to have very intense incoherent pumping of the working medium. The observation of induced γ-ray fluorescence is of fundamental interest, since essentially no induced effects have yet been observed at such short wavelengths.[1] At the same time, induced γ-ray fluorescence is the best test (in the development of a γ-ray laser) for the pump mechanism employed, whose efficiency should be sufficient for producing a certain inversion density in a system of nuclear levels.[1] Finally, the realization of induced γ-ray fluorescence (or, equivalently, induced radioactivity) will make it possible to produce a γ-ray source with unique properties: An initially weakly radioactive working medium emits as a result of incoherent pumping a substantial number of γ rays over a time of the order of the lifetime of the excited state of the nucleus.

In the present letter we examine induced γ-ray fluorescence for cold atoms of nuclear isomers localized in a magnetic trap (MT).[2,3] In our case the nuclei are first prepared in the required isomeric state (for example, by neutron irradiation) (Fig. 1), and then the cooled atoms of the nuclear isomer are injected into a magnetic trap (Fig. 2). Then it is proposed that the nuclei be transferred from the long-lived isomeric level to the upper isomeric level of an active γ transition (Fig. 1) by x radiation from a laser plasma produced by irradiating a solid-state target with a powerful picosecond laser pulse.[4–6] Localization of the nuclei in a MT makes it possible to increase the total number of excited nuclei to 10^{12} and correspondingly increase substantially the intensity of the γ-ray fluorescence obtained, since as a result of the relatively low density of isomeric nuclei, the x radiation is absorbed in the entire volume of the trap and not only in the skin layer, as was the case in Ref. 5, where a solid-state density of isomeric nuclei was employed.[a)]

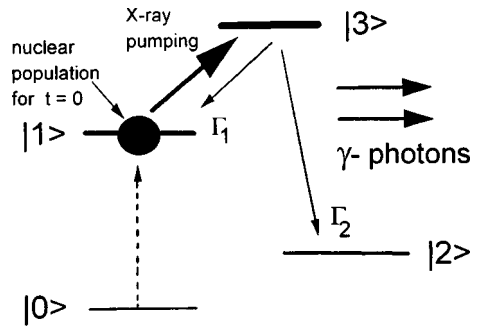

FIG. 1. Scheme of nuclear transitions. Here $|0\rangle$ is the ground state and $|1\rangle$ is the isomeric state of the nucleus. Initially, all nuclei are in the isomeric state $|1\rangle$. The x radiation from the laser plasma transfers the population to the upper active nuclear level $|3\rangle$, whence spontaneous decay to the state $|2\rangle$ with emission of a γ-ray occurs. $\Gamma_{1,2}$ — partial probabilities of the spontaneous decays $|3\rangle$–$|1\rangle$ and $|3\rangle$–$|2\rangle$.

At the same time, the relatively small number of isomeric nuclei required for loading the MT makes it possible to decrease the required efficiency of the production of isomeric nuclei, making it much easier to prepare the working medium as a whole. In addition, the low velocities of cold isomeric atoms in a MT greatly decrease the spectral width of the γ radiation obtained, since the linewidth in this case is determined by the Doppler effect due to the recoil of the nuclei during the emission of a γ-ray.

The idea of using a two-step pumping of a resonant γ transition (when isomeric nuclei are prepared first and then the nuclei are additionally excited by x-ray or optical radiation) was proposed in Ref. 4 in a discussion of possible schemes for γ-ray lasers, and it was elaborated in Ref. 5,[b)] where it was shown that nuclear isomers with lifetimes of several hours and with low-lying nuclear states with decay times of 100 ps are required to implement such a scheme.

Figure 2 shows the scheme for obtaining induced γ-ray fluorescence, where atoms of nuclear isomers in a MT are used as the active medium. We shall assume that the active γ transition is pumped in two stages: First, atoms of nuclear isomers are prepared, for example, by irradiating a dense gas with an intense beam of thermal neutrons (Fig. 1), and then, after a preliminary cooling and optical pumping of the atoms of the isomeric gas by laser radiation tuned to an appropriate atomic resonance transition of the nuclear

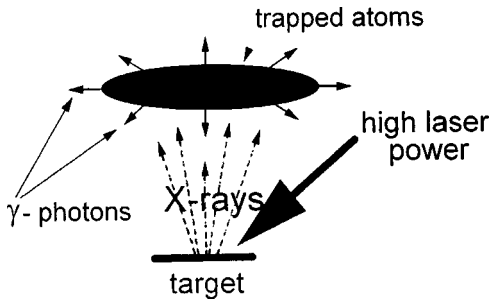

FIG. 2. Schematic diagram showing the production of induced γ-ray fluorescence.

isomer, the isomer atoms are trapped in a magnetic trap. Atoms are confined in such a trap by the force arising as a result of the spatial gradient of the magnetic field, since, as a result of interacting with the optical radiation, an atom is in a state with a definite value of the magnetic moment.[3] With pulsed loading of the cooled atoms of the nuclear isomer into the MT it is possible to accumulate $\approx 10^{12}$ atoms in the localization volume. Since the magnetic moment of an electronic shell can change as a result of atomic collisions, to obtain substantial densities of the nuclear isomer the total loading time τ_l should not exceed the interatomic collision time:

$$\tau_l \approx \tau_c = (\sigma N_{\rm at} \mathbf{v}_{\rm at})^{-1},$$

where $\sigma \approx 10^{-16}$ cm^2 is the gas-kinetic collision cross section, $N_{\rm at}$ is the density of atoms, and $\mathbf{v}_{\rm at}$ are the relative velocities of the atoms in the MT. For relative velocities of the atoms $\mathbf{v}_{\rm at} \approx 10^2$ cm/s (such velocities correspond to a temperature of the atomic ensemble $T = 10^{-2}$ K) the atomic collision time is $\tau_c \approx 0.1$ s and, correspondingly, the loading time τ_l of the MT should also be of the order of 0.1 s. At the same time, to confine 10^{12} atoms at temperature $T = 10^{-2}$ K in a ≈ 0.1 cm^3 trap, a magnetic field of 10^2 G is required. Such a field can be obtained relatively simply under laboratory conditions. As a result of such pulsed loading, a cloud of isomeric nuclei with density 10^{15} cm^{-3} at temperature $T = 10^{-2}$ K is formed in the MT in 0.1 s, after which the x radiation from the laser plasma, produced near the localization region, pumps the active γ transition $|3\rangle$–$|2\rangle$ in 10 ps (Fig. 1).

Let us now estimate the efficiency of the production of resonant γ rays by the pumping of isomeric nuclei in a magnetic trap with x radiation from a hot plasma. At the present time x-ray pumping of such intensity (where the number of resonant x-ray photons is at least equal to the number of isomeric nuclei in the magnetic trap) can be obtained only by irradiating a solid-state target with an intense (10^{17-18} W/cm^2) subpicosecond laser pulse.[4–6] The radiation spectrum from the hot plasma spot produced by such irradiation is close to that of an absolute black body.

The x-ray photon flux from a unit surface area of the hot plasma spot produced by irradiation with a powerful laser pulse is

$$\frac{dN_x}{dt d\omega_x ds} = \frac{\omega_x^2}{\pi^2 c^2} [e^{\hbar\omega_x/T} - 1]^{-1}, \tag{1}$$

where T is the temperature of the laser plasma and ω_x and N_x are, respectively, the frequency and initial number of x-ray photons, respectively. Let the area of the plasma spot be s and the size of the cloud of isomeric nuclei along the direction of propagation of the x rays be a_i. Then the total cross section for resonant absorption of x-ray pump photons by the ensemble of nuclei in the magnetic trap can be estimated as

$$\sigma_f = \sigma_x N_{\rm at} s a_i, \tag{2}$$

where $\sigma_x = 2\pi c^2/\omega_x^2$ is the cross section for resonant absorption of an x-ray photon and $N_{\rm at}$ is the density of isomeric nuclei. Then, over the time τ_i of the laser pulse producing the plasma, the number N_s of isomeric nuclei in the magnetic trap that will be transferred to the upper active level from which γ-ray fluorescence is expected is

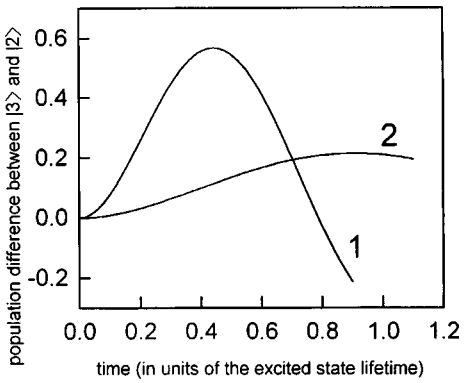

FIG. 3. Time-dependence of the population difference between the states $|3\rangle$ and $|2\rangle$ for different x-ray pump intensities: *1* — Saturation of the transition $|1\rangle$–$|3\rangle$,G=3; *2* — $G=0.3$. As one can see, the population inversion reaches 0.1 for a pulse duration $\approx 0.1\Gamma_0$ in the case of substantial saturations of the transition $|1\rangle$–$|3\rangle$, and 0.01 for weak saturation.

$$N_s = \frac{dN_x}{dt\,d\omega_x\,ds}\,\sigma_f \Gamma_0 \tau_i = \frac{2}{\pi}\,\frac{N_{\rm at} s a_i \Gamma_0 \tau_i}{e^{\hbar\omega_x/T}-1}, \tag{3a}$$

where $\Gamma_0=\Gamma_1+\Gamma_2$ is the natural width of the resonant γ transition $|3\rangle$–$|2\rangle$ (Fig. 1). Correspondingly, the nuclear population inversion density in the MT can be obtained from Eq. (3a) as

$$n_{\rm inv} \approx 0.1\Gamma_0 \tau_i N_{\rm at} \approx 10^{-2} N_{\rm at}, \tag{3b}$$

where we have assumed the excitation volume to be $\approx s a_i$ and the pulse duration $\tau_i = 10^{-10}$ s. Next, the partial widths $\Gamma_{1,2}$ of the transitions $|3\rangle$–$|1\rangle$,$|2\rangle$ can be obtained from the single-particle Weisskopf approximation[7] as $\Gamma_1 \approx 10^7$ s^{-1} for $\lambda_x \approx 6\times 10^{-8}$ cm ($\hbar\omega_\gamma = 1$ keV) and $\Gamma_2 \approx 10^9$ s^{-1} for $\lambda_\gamma \approx 6\times 10^{-9}$ cm ($\hbar\omega_\gamma = 20$ keV). Here we have assumed that the transitions $|3\rangle$–$|1\rangle$,$|2\rangle$ are magnetic-dipole transitions (see footnote b). It follows from the estimate (3b) that only a small fraction of the total number of nuclei in the MT can be transferred to the upper excited state $|3\rangle$ by the x radiation from the laser plasma.

To determine the temporal dynamics of the population of the active level $|3\rangle$ of the γ transition, we solved the equations for the elements of the density matrix of a three-level system ($|1\rangle$,$|2\rangle$,$|3\rangle$). In so doing, we assumed that initially the entire population is concentrated in the state $|1\rangle$ and that coherence (i.e., the off-diagonal element of the density matrix between the states $|1\rangle$ and $|3\rangle$) on the transition $|1\rangle$–$|3\rangle$ is absent. The computational results for different x-ray pump intensities are presented in Fig. 3. As one can see, for substantial x-ray pump intensities a population inversion of ≈ 0.1 can be obtained during a pulse of duration $0.1\Gamma^{-1}$. At the same time, for low saturations of the transition $|1\rangle$–$|3\rangle$ appreciable inversion can be obtained only for a pulse duration of $\approx \Gamma_0^{-1}$.

Let us now estimate the total energy $E_{\rm tot}$ of the γ-ray pulse in the induced fluorescence of isomeric nuclei in a magnetic trap. Then, according to Eq. (3b), the number of isomeric nuclei which are inverted by the x radiation will be $N_{\rm inv} \approx 10^{10}$ for $\approx 10^{12}$ nuclei

initially in the MT (here we assumed that the light spot is 10^{-2} cm in size, which is the characteristic size of the region of localization of the isomeric nuclei, while the absorption length of an x-ray photon for $\hbar\omega_\gamma = 1$ keV is $a_i = 0.1$ cm). This same number of γ rays will obtained in the spontaneous decay of the state $|3\rangle$ to the state $|2\rangle$. Accordingly, the total energy of the spontaneous γ-ray pulse will be $E_{\text{tot}} = \hbar\omega_\gamma N_{\text{inv}} \approx 3\times 10^{-6}$ J in a time $\tau = \Gamma_0^{-1} = 10^{-9}$ s. We note that such a source activity when scaled to one second, 10^{10} GBq, is comparable only to the activity existing one minute after a nuclear explosion, 7×10^{13} GBq. As a result, there appears a real possibility of modeling such intense irradiation of materials under laboratory conditions for times of tens or hundreds of picoseconds, which could be interesting and useful not only for materials science but also for investigating the mechanisms leading to mutations.

At the same time, the width of the γ-ray spectrum obtained in the transition $|3\rangle$–$|2\rangle$ is determined by the Doppler frequency shift due to the recoil accompanying emission of a γ ray. For the values presented above, the width of the γ-ray spectrum obtained is $\Delta\omega_D = \hbar k_\gamma^2 / A m_p = 10^{13}$ Hz, where k_γ is the modulus of the γ-ray wave vector, A is the atomic number, m_p is the proton mass, and the γ-ray energy is 20 keV. Accordingly, the spectral brightness of a radioactive source based on isomeric nuclei in a magnetic trap is also high: 10^6 Bq/Hz. At the same time, the spectrum of such a γ-ray source can be adjusted by using isomeric nuclei with the appropriate level structure.

We assumed above that all x-ray pump photons are absorbed by the corresponding transition $|1\rangle$–$|3\rangle$ of the isomeric nuclei. In that case Eq. (3) determines the number of activated nuclei in the magnetic trap in the absence of losses of x-ray pump photons as a result of two basic processes: the photoeffect in the continuous spectrum of the x-ray pump, with cross section[8]

$$\sigma^{\text{ph.eff}}(\omega) = \frac{32\pi 2^{1/2}\alpha^4 Z^5}{3}(e^2/m_e c^2)^2 (m_e c^2/\hbar\omega)^{7/2}, \tag{4}$$

and absorption of pump photons by other nuclei and low-lying electronic levels.

It is well known that the resonance absorption cross sections of the outer electronic shells of atoms are much larger than σ_x. For this reason, to cut off the low-energy part of the pump spectrum (i.e., the region in which the absorption lines of the outer electronic shells lie), it is necessary to use a filter that cuts off the pump below the frequency ω_*. Taking this into account, we can determine the number of activated isomeric nuclei as

$$N_\gamma = \frac{N_s}{1 + \sum\limits_{i=1} \dfrac{\gamma_i (e^{\hbar\omega_x/T} - 1)}{\Gamma_0 (e^{\hbar\omega_i/T} - 1)} + \displaystyle\int_{\omega_*} \sigma^{\text{ph.eff}}(\omega) \frac{\omega^2}{2\pi c^2} \frac{e^{\hbar\omega_x/T} - 1}{e^{\hbar\omega/T} - 1} \frac{d\omega}{\Gamma_0}}, \tag{5}$$

where the sum over i includes both nuclear and low-lying electronic levels which fall within the spectral interval of the pump. Every such resonance has an absorption cross section $\sigma_i = 2\pi c^2/\omega_i^2$ and width γ_i. Choosing the pump photon energy so that $\hbar\omega_x > T, \hbar\omega_*$ and assuming that $\omega_i > \omega_x$ for all i ($\omega_* < \omega_x < \omega_i$ for $\forall i$), we find that the terms in the sum in the denominator of Eq. (5) are small compared to 1.

Let us now estimate the losses of x-ray pump photons due to ionization of the atoms. For this, it is necessary to calculate the integral in the denominator of Eq. (5), and the condition for the ionization losses to be small can be written in the form

$$7.4Z^5\alpha^6(m_ec^2/\hbar\omega_*)^{3/2}\frac{T}{\hbar\gamma_0}(e^{\hbar\omega_x/T}-1)e^{-\hbar\omega_x/T}\leqslant 1, \tag{6}$$

where $\alpha=(137)^{-1}$ is the fine structure constant. Substituting into Eq. (6) $\hbar\gamma_0=10^{-3}$ eV, $\hbar\omega_*=511$ eV, $\hbar(\omega_x-\omega_*)<T$, and $T=400$ eV we obtain from Eq. (6) an estimate of the charge of an isomeric nucleus: $Z\leqslant 10$. Equation (6) shows that the losses of x-ray pump photons (and, in consequence, the losses of activated nuclei) due to ionization of the atoms increase rapidly with the nuclear charge Z (as $\sim Z^5$). Accordingly, for nuclear isomers with $Z\geqslant 10$ the x-ray photon yield from the surface of the plasma spot must be increased, which would require that the intensity of the laser pulse be increased to 10^{20}–10^{21} W/cm^2.

It should be specially noted that there are now no fundamental difficulties in observing experimentally phenomena such as laser-stimulated radioactivity of isomeric nuclei in a magnetic trap. For example, ^{58}Co, ^{84}Rb, ^{93}Mo, and ^{152}Eu nuclei found in suitable isomeric states and localized in a MT can be used as the working medium.[9] Since laser cooling is strongly selective, 10^{11} atoms can be obtained relatively easily in such a trap.[3] For example, for ^{84}Rb the lifetime of the excited state $|3\rangle$ is 10^{-8} s, while the energy of the spontaneously emitted γ ray in the transition $|3\rangle$–$|2\rangle$ is 219 keV (for a half-life of the isomeric state $\approx$0.3 h and with a 3.4 keV x-ray pump photon). Then such a source makes it possible to obtain $\approx 10^7$ resonant γ rays with total energy $E_{\rm tot}=10^{-7}$ J within the lifetime of the upper excited state. Such activity already corresponds to the activity of sources used for chemical analysis of samples. The activity of such a source can be increased by increasing the number of nuclei in the localization region.

Induced radioactivity can be detected by simply tuning the detection system to the energy of the emitted γ rays. Since the maximum of the radiation from the laser plasma lies in the range $\approx$3.4 keV, near $\approx$200 keV there are virtually no primary γ rays which are produced by vaporizing a solid-state target with a laser pulse.

At the same time, since isomeric nuclei also possess intrinsic radioactivity, the natural background can be eliminated by using time-selective signal detection. For example, the natural background radioactivity for isomeric nuclei with a 1-hour half-life is $\approx 10^7$ decays per second at the density indicated above. However, over times $\approx 10^{-6}$ s the number of γ rays due to natural radioactivity will equal only several tens, while the stimulated radioactivity signal will exceed several millions. For this reason, the signal/noise ratio in such a time-selective experiment will be 10^5, which can be easily detected.

We thank T. A. Vartanyan, L. A. Rivlin, A. E. Antronov, and A. P. Dubenskiĭ for interesting discussions and for their unflagging interest in this work.

[a)]For example, the cross section for resonant absorption of an x-ray pump photon is $\sigma_x\approx\lambda_x^2=10^{-16}$ cm^2 (for $\lambda_x=10^{-8}$ cm), while the absorption length is $l_{\rm abs}=(\sigma_xN)^{-1}=10^{-7}$ cm, where $N=10^{23}$ cm^{-3}. In addition, x-ray pump photons are absorbed not only by the dopant isomeric nuclei but by the whole sample. Then, for a density of isomeric nuclei in the solid-state target $\approx 10^{13}$ cm^{-3} (which corresponds to the production of isomeric nuclei in a nuclear reaction in the sample during the half-life of the isomeric state) and typical size of the light spot $\approx$0.1 cm, the total number of isomeric nuclei in the excitation volume is only 10^4.

[b)]In our view, the optimism concerning the realization of a γ-ray laser based on two-step pumping is greatly exaggerated, since in Refs. 4 and 5 the gain of resonant γ-ray radiation was estimated using the linewidth obtained in the electric-dipole approximation for an active γ transition. At the same time, it is known[7] that in nuclei such transitions are strongly suppressed (by a factor of 10^4–10^6 for the energy range considered,

20–100 keV). As a result, if the estimates presented in Refs. 4 and 5 are made with allowance for the specifics of nuclear systems, then the gain cannot exceed 10^{-4}–10^{-5} cm^{-1}.

[1] J. Baldwin and J. Solem, Rev. Mod. Phys. **69**, 1085 (1997).
[2] V. V. Vladimirskiĭ, Zh. Éksp. Teor. Fiz. **39,** 1062 (1960) [Sov. Phys. JETP **12**, 740 (1961)]; see also the references in V. I. Ignatovich, *Physics of Ultracold Neutrons*, Nauka, Moscow, 1986.
[3] D. Boiron, C. Triche, D. R. Meacher *et al.*, Phys. Rev. A **52**, R3425 (1995).
[4] C. B. Collins, F. W. Lee, D. M. Shemell *et al.*, J. Appl. Phys. **53**, 4645 (1982).
[5] A. V. Andreev, Vestn. Mosk. Univ. Ser. 3, Fiz., Astron. **35,** 28 (1994).
[6] Y. Izava, Phys. Lett. B **88**, 59 (1989).
[7] A. Bohr and B. Mottelson, *Nuclear Structure*, Benjamin, New York, 1975, Vol. 2 [Russian translation, Mir, Moscow, 1977].
[8] V. B. Berestetskiĭ, E. M. Lifshitz, and L. P. Pitaevskiĭ, *Quantum Electrodynamics*, Pergamon Press, New York, 1982, 2nd edition [Russian original, Nauka, Moscow, 1980, Vol. 4].
[9] Nuclear Data Sheets (1989–1998).

Translated by M. E. Alferieff

X-ray interferometric short-wavelength holography with diffraction focusing

A. M. Egiazaryan, K. G. Truni, and A. R. Mkrtchyan
Institute of Applied Physics, Armenian National Academy of Sciences, 375014 Erevan, Armenia

(Submitted 26 August 1998)
Pis'ma Zh. Éksp. Teor. Fiz. **68**, No. 9, 681–684 (10 November 1998)

A four-unit off-axis interferometric scheme for recording x-ray short-wavelength holograms of amorphous bodies which are opaque to visible light is proposed. The diffraction spreading of the object wave in a unit is removed by diffraction focusing of the same wave in the next unit. © *1998 American Institute of Physics.*
[S0021-3640(98)00521-0]

PACS numbers: 41.50.+h, 07.85.−m

The realization of x-ray short-wavelength holography is very important for the advancement of microscopy as well as for visualization of the internal microstructure of materials which are opaque to optical radiation. For this reason, x-ray short-wavelength holography is of definite interest together with electronic microscopy and optical holography. The realization of x-ray holography will open up new prospects for x-ray flaw detection, holography of microobjects, medical diagnostics, and x-ray coherent optics. Moreover, the reconstruction of an x-ray wave front using a wave from an optical laser makes it possible to reduce, in part, the problem of x-ray investigations to the problem of determining the information content of an optical wave.

In 1952 El-Sum and Kirkpatrick were able to obtain a visible image of a thin wire by illuminating an x-ray diffraction pattern of the wire recorded 20 years earlier by Kellström. The possibility of realizing x-ray-holographic microscopy in the soft x-ray range using radiation from an x-ray microanalyzer was demonstrated in Refs. 1 and 2. The real possibilities of x-ray-holographic microscopy, from the standpoint of the limited spectral power of existing x-ray sources, have been examined in detail in Refs. 3 and 4.

In Refs. 5 and 6 we estimated the spatial-coherence radius of x-ray beams diffraction-collimated in crystal monochromators for the purpose of using them in x-ray holography. Later,[7] combining the phenomenon of coherent splitting of the x-ray radiation in the process of Laue transmission through perfect crystals, the sharp increase in their coherence characteristics in the course of this transmission, the recording of x-ray interferometric patterns, and the recording of holograms, we proposed an interferometric scheme for recording x-ray short-wavelength holograms of crystals.

In the present letter we propose a four-unit scheme, using diffraction focusing of x-ray beams in two-crystal systems, for recording x-ray short-wavelength holograms of amorphous bodies which are opaque to visible light.

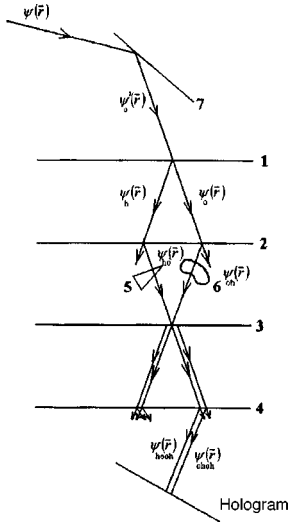

FIG. 1. Diagram illustrating the recording of a hologram.

INTERFEROMETRIC SCHEME FOR RECORDING HOLOGRAMS OF AMORPHOUS BODIES

The following interferometric scheme is proposed for recording x-ray short-wavelength holograms of amorphous bodies (see Fig. 1). An x-ray wave with complex amplitude $\psi(\mathbf{r})$ from an x-ray source is incident at the Bragg reflection angle on a crystal monochromator *7*. After diffraction collimation in the monochromator, depending on the collimation angle, the transverse coherence radius of the reflected beam increases. This radius is inversely proportional to the collimation angle and is of the order of 100 μm for radiation with wavelength $\lambda \sim 1$ Å and collimation angles $\Delta\alpha \sim 10^{-6}$ rad. The plane-parallel plates *1*, *2*, *3*, and *4*, consisting of perfect crystals, are oriented in a position of reflection relative to the incident wave with amplitude $\psi_0^i(\mathbf{r})$. As a result of diffraction by the plate *1* the wave $\psi_0^i(\mathbf{r})$ splits coherently into two almost identical waves, $\psi_h(\mathbf{r})$ and $\psi_0(\mathbf{r})$, propagating in the reflection and transmission directions, respectively.[8,9] As a result of the diffraction of these waves by crystal *2*, the waves of interest to us, with amplitudes $\psi_{h0}(\mathbf{r})$ and $\psi_{0h}(\mathbf{r})$, are formed among other waves. A homogeneous prism *5* is placed in the path of the wave $\psi_{h0}(\mathbf{r})$. This prism deflects this wave by a small angle $\Delta\alpha$ without taking it out of the reflection position. This angle is determined by the expression

$$\Delta\alpha = (1-n)\tan\alpha, \tag{1}$$

where α and n are, respectively, the angle and index of refraction of the prism. As a result of this deflection, after the wave $\psi_{h0}(\mathbf{r})$ is diffracted by crystals *3* and *4*, a reference wave with amplitude $\psi_{h00h}(\mathbf{r})$ is formed. The propagation axis of this wave is inclined by the angle $\Delta\alpha$ away from the position of exact Bragg reflection. The amorphous object *6* is placed in the propagation path of the wave $\psi_{0h}(\mathbf{r})$. The radiation passing through this object forms an object wave $\psi_{0h}(\mathbf{r})$ (see Fig. 1), which is diffracted by crystals *3* and *4*. After diffraction by crystals *3* and *4*, part of the object wave $\psi_{0h}(\mathbf{r})$ forms an object wave

with amplitude $\psi_{0h0h}(\mathbf{r})$ whose propagation axis makes a small angle $\Delta\alpha$ with the propagation axis of the reference wave $\psi_{h00h}(\mathbf{r})$. That is, the proposed scheme for recording short-wavelength x-ray holograms of amorphous bodies is an off-axis holographic recording scheme. The waves ψ_{h0} and ψ_{0h} are brought into coincidence at the entrance surface of the analyzer crystal *3* before diffracting in it. The intensity J_0 of this interference field is given by the formula

$$J_0(\mathbf{r})=|\psi_{h0}+\psi_{0h}|^2=|\psi_{h0}|^2+|\psi_{0h}|^2+2|\psi_{h0}||\psi_{0h}|\cos[(\mathbf{k}_{h0}-\mathbf{k}_{0h})\cdot\mathbf{r}+\varphi(\mathbf{r})], \quad (2)$$

where the argument of the interference term consists of two terms. The term $(\mathbf{k}_{h0}-\mathbf{k}_{0h})\cdot\mathbf{r}$ changes by 2π in three-dimensional objects of size $\Delta r\sim 10^{-8}$ cm, since the quantity $(\mathbf{k}_{h0}-\mathbf{k}_{0h})$ is of the order of 10^8cm^{-1}. Let the amorphous body *6* add to the wave ψ_{0h} a macroscopically varying phase $\varphi(\mathbf{r})$. The mathematical condition for this is

$$|\nabla\varphi(\mathbf{r})|<10^3\ \text{cm}^{-1}.$$

Since the argument of the interference term in Eq. (2) changes by 2π in spatial regions of size 10^{-8} cm, the interference field cannot be detected by existing recording materials because of the limited resolution. Let us see how the intensity $J(\mathbf{r})$ of the interference field differs from that of the interference field of the waves ψ_{h00h} and ψ_{0h0h}. $J(\mathbf{r})$ is defined as

$$J(\mathbf{r})=|\psi_{h00h}|^2+|\psi_{0h0h}|^2+2|\psi_{0h0h}||\psi_{h00h}|\cos[(\mathbf{k}_{h00h}-\mathbf{k}_{0h0h})\cdot\mathbf{r}+\varphi(\mathbf{r})]. \quad (3)$$

Let us determine the angular region $\Delta\alpha_1$ of spatial frequencies of the wave ψ_{0h} within which the characteristic Fourier components passing through the crystal unit *3* or a vacuum layer of the same thickness are identical in the sense of acquiring an additional phase. This condition is

$$\frac{kd(n-1)}{\cos(\theta_B+\Delta\alpha_1)}-\frac{kd(n-1)}{\cos\theta_B}<\frac{\pi}{100}, \quad (4)$$

where $k\sim 10^8$ cm^{-1} is the wave number; $d\sim 10^{-1}$ cm is the thickness of the third unit; θ_B is the exact Bragg angle, of the order of 1 rad; and, $n-1\sim 10^{-6}$. From condition (4) with the above-indicated values of the parameters we find that $\Delta\alpha_1\sim 10^{-3}$ rad, which is much greater than the angular region of transmission of the crystal. Therefore the wave fronts of the waves ψ_{h0}, ψ_{h00}, and ψ_{h00h} are similar surfaces.

The argument of the interference term in expression (3) is a macroscopically varying phase, since the wave vectors $\mathbf{k}_{h00h}$ and $\mathbf{k}_{0h0h}$ are deflected by the angle $\Delta\alpha_1$. A comparison of expressions (2) and (3) shows that the analyzer unit *3* is a kind of filter of the intensity of the interference field, transmitting only the low modulation frequency of the field. This phenomenon makes it possible to record the interference pattern of the waves ψ_{h00h} and ψ_{0h0h}, which in the case at hand is an off-axis x-ray hologram of the object *6*.

Specifically, when the object *6* consists of two media with different electron densities N_1 and N_2 (see Fig. 2) such that $N_2>N_1$, total internal reflection of the x-ray beam occurs at the boundary of these media. Then the object wave ψ_{0h0h} contains complete information about the interface of these media.

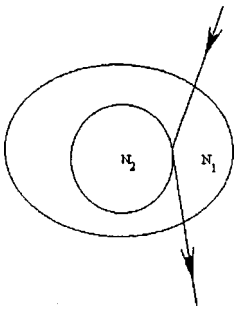

FIG. 2. Diagram illustrating the formation of an object wave.

When the object wave ψ_{0h} is diffracted by the analyzer unit *3*, diffraction spreading of the x-ray beam occurs and is removed by diffraction focusing in the unit *4*:[10,11]

$$\psi_{0h0h}(x) = \exp[i\mathbf{k}_h\cdot\mathbf{r}]\left\{\frac{\pi^2k^2c^2\chi_h\chi_{\hbar}}{\gamma_0\gamma_h}\int_{-\infty}^{\infty}\phi_{0h}(p)e^{ipx}\frac{\sin z_3\sqrt{p^2b^2+\beta^2}\sin z_4\sqrt{p^2b^2+\beta^2}}{p^2+\beta^2}dP,\right. \tag{5}$$

where $\phi_{0h}(p)$ is the Fourier transform of the function $\psi_{0h}(x)$, z_3 and z_4 are the thicknesses of the corresponding units, $\beta=\pi kc(\chi_h\chi_{\hbar})^{1/2}/\gamma_0\gamma_h$ (C is the polarization factor of the diffracted beam), χ_h and $\chi_{\hbar}$ are, respectively, the Fourier components of the polarizability of the crystal, γ_0 and γ_h are the direction cosines of the diffracted beam, and $b=\sin^2\theta_B/2\gamma_0\gamma_h$.

For $\psi_{0h}(x)=\delta(x)$, where $\delta(x)$ is the Dirac delta function, $\phi_{0h}(p)\equiv 1$. In the scheme which we have proposed $z_3=z_4$, and it follows from expression (5) that when the beam undergoes double reflection by the units *3* and *4*, diffraction focusing of the beam occurs. Then we obtain after some simplifications

$$\psi_{0h0h}(x)=-\frac{\pi\beta}{8}e^{-\beta x}. \tag{6}$$

The diffraction smearing of the object image in the process of diffraction of an x-ray beam by the unit *3* is removed by the diffraction focusing accompanying diffraction by the unit *4*. Therefore the image of a point of the object *6* is a point in the region where the hologram is recorded. Hence it follows that the object wave $\psi_{0h0h}(\mathbf{r})$ contains complete information about the exact geometry of the interior interface in the object 6. Reconstructing the object wave in visible light, we solve the visualization problem and obtain a reconstructed visible three-dimensional image of the interface of the two media in the object 6. It follows from Eq. (6) that the phenomenon of diffraction focusing of x rays can be used to decrease the size of the focus to 1 μm. The angular region of transmission of the crystal is $\sim 10''$, and therefore when the hologram is recorded at a wavelength $\lambda\sim 1$ Å, a local resolution of the order of 1 μm in the object image can actually be achieved in the reconstructed image.

[1] J. W. Giles, J. Opt. Soc. Am. **59**, 1179 (1969).
[2] S. Aoki and S. Kikuta, Jpn. J. Appl. Phys. **13**, 1385 (1974).
[3] V. V. Aristov and G. A. Ivanova, J. Appl. Crystallogr. **12**, 19 (1979).
[4] V. V. Aristov and G. A. Bashkina, in *Proceedings of the All-Union Conference of Schools of Higher Learning on Multiwave Scattering of X Rays*, Erevan State University Press (1978).
[5] A. M. Egiazaryan, A. G. Rostomyan, and P. A. Bezirganyan, Dokl. Akad. Nauk Arm. SSR **66**, 228 (1978).
[6] A. M. Egiazaryan, A. G. Rostomyan, A. M. Grigoryan, and P. A. Bezirganyan, Zh. Tekh. Fiz. **49**, 2238 (1979) [Sov. Phys. Tech. Phys. **24**, 1236 (1979)].
[7] A. M. Egiazaryan and P. A. Bezirganyan, Izv. Akad. Nauk Arm. SSR, Fiz. **15**, 35 (1980).
[8] A. M. Afanasiev and Yu. Kagan, Acta Cryst. A **24**, 163 (1968).
[9] V. L. Indenbom and F. N. Chukhovskiĭ, Usp. Fiz. Nauk **107**, 229 (1972) [Sov. Phys. Usp. **15**, 298 (1972)].
[10] V. L. Indenbom, I. Sh. Slobodetskiĭ, and K. G. Truni, Zh. Éksp. Teor. Fiz. **66**, 1110 (1974) [Sov. Phys. JETP **39**, 542 (1974)].
[11] V. L. Indenbom and G. M. Aladzhadyan, Dokl. Akad. Nauk SSSR **227**, 827 (1976) [Sov. Phys. Dokl. **21**, 191 (1976)].

Translated by M. E. Alferieff

Interdiffusion of layers in PbSe–PbS epitaxial superlattices

A. Yu. Sipatov[a)]
Kharkov State Polytechnical University, 310002 Kharkov, Ukraine

(Submitted 8 September 1998)
Pis'ma Zh. Éksp. Teor. Fiz. **68**, No. 9, 685–687 (10 November 1998)

X-ray diffraction methods are used to investigate the diffusional mixing of layers in PbSe–PbS superlattices. The interdiffusion coefficients of the layers are determined from the change in the intensity of satellite reflections. Two stages of diffusion are observed — fast (at the initial stages of anneals) and slow. © *1998 American Institute of Physics.* [S0021-3640(98)00621-5]

PACS numbers: 68.65.+g, 68.35.Fx

IV–VI superlattices open up wide possibilities both for fundamental investigations in solid-state physics[1–4] and for the development of new functional components for microelectronics, IR technology, and thermoelectricity.[5,6] For such structures with ultrathin layers the state of the interphase boundaries — their roughness, the sharpness of the transition from one layer to another, the presence and size of the mixed zones, and the temporal and temperature stability of their structure and properties — is very important. Diffusion processes in such ultrathin layers with a large concentration gradient of the elements can have their own unique features and differences from the bulk state.[7,8] For this reason, investigations of the interdiffusion of layers in superlattices (SLs) are of great importance from both the theoretical and practical standpoints.

One of the most effective methods for investigating SLs is x-ray diffraction. This method makes it possible not only to follow the mixing of the layers but also to determine the interdiffusion coefficients of the layers according to the variation of the intensity of the satellites of reflections:[9,10]

$$\ln[I_k(\tau_2)/I_k(\tau_1)] = -8k^2\pi^2 D(\tau_2-\tau_1)/H^2, \tag{1}$$

where D is the diffusion coefficient, H is the superlattice period, k is the order of the satellite reflection, I_k is the relative intensity of the satellite reflection of order k, normalized to the intensity of the zeroth-order reflection, and τ is the annealing time.

The subject of the present investigation are PbSe–PbS superlattices fabricated in an oil-free vacuum (10^{-4}–10^{-5} Pa) by thermal evaporation of lead chalcogenides from tungsten boats and subsequent condensation of the chalcogenides on a (001) KCl surface at 473 K. The thickness of the layers and the condensation rate were monitored with a calibrated quartz resonator placed next to the substrate. Superlattices with different layer thicknesses and with periods of 19 and 22 nm (the number of periods was 20) were fabricated. To eliminate from the diffraction pattern the reflections from the substrate, the

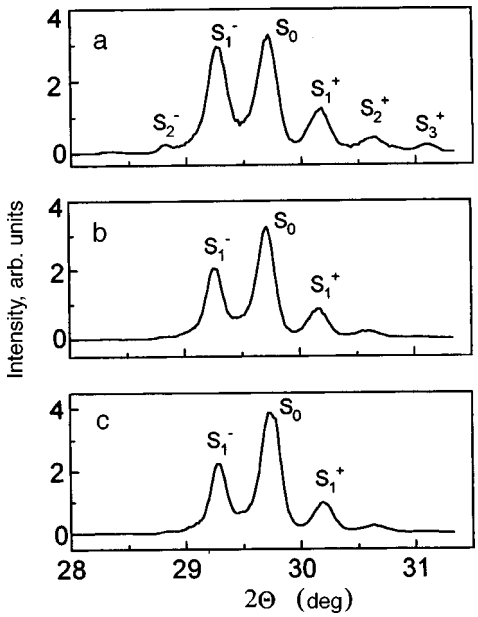

FIG. 1. X-ray diffraction patterns of PbSe–PbS superlattices with period 22 nm in the initial state (a) and after 10 h (b) and 78 h (c) anneals at 543 K. S_n — satellite reflections.

superlattices were detached from the substrates by dissolving the KCl in distilled water and ''fished out'' onto amorphous quartz wafers. Structural investigations (electron microscopy and x-ray diffraction) showed that the PbSe–PbS superlattices consist of single-crystal layers in the (001) orientation, with sharp interfaces. This is indicated by the presence of satellite reflections of third order in the x-ray diffraction patterns (Fig. 1a). A series of diffusion anneals was performed in vacuum at temperatures 543, 593, and 623 K. The samples were periodically removed for x-ray measurements, which were performed in a $\Theta-2\Theta$ scheme in the reflection (200). One can see in Fig. 1 that in the process of annealing, the intensity of the lateral satellite reflections decreases while that of the central (zeroth) reflection increases, indicating intermixing of the layers. The process of mixing of the layers at 543 K is shown more clearly in Fig. 2, whence one can see that there exist two stages of diffusion — fast (at the initial stages of anneals) and slow. Similar behavior of the change in the relative intensity of the satellite reflections are observed at 593 and 623 K. Using expression (1), we have determined the interdiffusion coefficients of the layers. Their values are: for fast diffusion $D=3.6\times10^{-19}$ cm^2/s (543 K), 2×10^{-18} cm^2/s (593 K), and 4.9×10^{-18} cm^2/s (623 K); for slow diffusion $D=1.6\times10^{-19}$ cm^2/s (543 K), 4×10^{-19} cm^2/s (593 K), and 2.15×10^{-18} cm^2/s (623 K).

Using the Arrhenius law ($D=D_0\exp(E/kT)$) we have determined the activation energies E and the pre-exponential factors D_0 for the fast and slow stages of diffusion: $D_0=2.4\times10^{-10}$ cm^2/s and $E=0.95$ eV for the fast stage, and $D_0=5.3\times10^{-4}$ cm^2/s and $E=1.78$ eV for the slow stage.

The fast diffusion at the initial stages of anneals is evidently due to the presence of

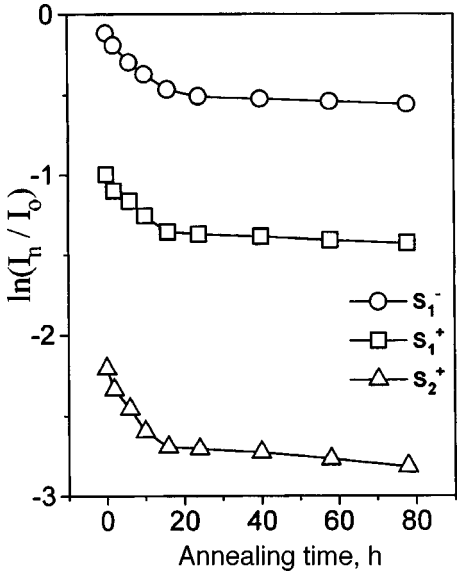

FIG. 2. Variation of the relative intensity of the satellite reflections of first (S_1) and second (S_2) reflection orders as a function of the annealing time at 543 K for the PbSe–PbS superlattices with a 22 nm period.

nonequilibrium nonstoichiometric point defects in lead chalcogenides.[11] This is also indicated by the low value of the activation energy ($E=0.95$ eV).

[a)]e-mail: sipat@kpi.kharkov.ua

[1] I. V. Kolesnikov and A. Yu. Sipatov, Fiz. Tekh. Poluprovodn. **23**, 954 (1989) [Sov. Phys. Semicond. **23**, 598 (1989)].
[2] V. N. Lytskii, V. A. Petrov, A. S. Rylik *et al.*, Phys. Low-Dim. Struct. **7**, 37 (1994).
[3] N. Yu. Fogel, V. G. Cherkasova, A. S. Pokhila *et al.*, Czech. J. Phys. **46**, 727 (1996).
[4] A. Stachow-Wojcik, A. Twardowski, T. Story *et al.*, Acta Phys. Pol. A **92**, 985 (1997).
[5] D. L. Partin, Appl. Phys. Lett. **45**, 487 (1984).
[6] L. D. Hicks, T. C. Harman, X. Sun *et al.*, Phys. Rev. B **53**, R10, 493 (1996).
[7] G. E. Henein and J. E. Hilliard, J. Appl. Phys. **55**, 2895 (1984).
[8] D. K. Arch, J. P. Faurie, J.-L. Staudenmann *et al.*, J. Vac. Sci. Technol. A **4**, 2101 (1986).
[9] H. Krenn, E. Koppensteiner, A. Holzinger *et al.*, J. Appl. Phys. **72**, 97 (1992).
[10] A. G. Fedorov, I. A. Shneiderman, A. Yu. Sipatov *et al.*, Functional Materials **5**, 52 (1998).
[11] V. Leute, H. Bottner, and H. Schmidtke, Z. Naturforsch. Teil A **34**, 89 (1978).

Translated by M. E. Alferieff

Self-organization of the critical state in a chain of SQUIDs

S. L. Ginzburg and N. E. Savitskaya
St. Petersburg Institute of Nuclear Physics, 188350 Gatchina, Russia

(Submitted 22 September 1998)
Pis'ma Zh. Éksp. Teor. Fiz. **68**, No. 9, 688–694 (10 November 1998)

The critical state of a 1D granular superconductor (modeled as a chain of SQUIDs or, in other words, a 1D Josephson-junction array) is studied on the basis of a system of differential equations for the gauge-invariant phase difference. It is established that the critical state is self-organized. It is shown that the problems of self-organization in the sandpile model and in a granular superconductor belong to the same universality class. © *1998 American Institute of Physics.* [S0021-3640(98)00721-X]

PACS numbers: 74.80.Bj, 85.25.Dq, 85.25.Cp

Interest in granular superconductors arose after the discovery of high-temperature superconductivity and it became clear that most HTSC materials can be obtained in the form of granular systems. In recent years[1–3] there have been a number of theoretical papers on the magnetic properties of granular superconductors (GSCs) as modeled by an ordered array of intercoupled Josephson junctions. In Refs. 1 and 2 it was shown that, like hard type-II superconductors, such systems arrive in a critical state (CS) that can be described by the Bean model.[4] At the same time, if the main parameter of the system $V \sim j_c a^3/\Phi_0$ (j_c is the critical current density at a junction, a is the array spacing, and Φ_0 is the magnetic flux quantum), each cell in the array and therefore the system as a whole have a large number of metastable states.[3]

The presence of a large number of metastable states is a characteristic feature of systems in which the phenomenon of self-organized criticality (SOC) is observed.[5] This phenomenon consists in the fact that in the course of its evolution a dynamical system arrives in a CS which is self-sustaining and does not require exact tuning of the external parameters for its existence. Structurally, the CS that arises consists of a collection of metastable states which pass into one another by means of ''avalanches'' arising as a result of a local external disturbance. Such a CS is said to be self-organized, and a power-law dependence of the probability density of avalanche sizes is taken as the criterion for the existence of SOC in the system. The concept of SOC is extremely general. It is applicable for describing the behavior of dynamical systems in different fields of modern science. Despite this, however, SOC has been studied thus far only in model systems which are difficult to obtain in practice, while experimental investigations of SOC have been performed only for a sandpile.[6] The observation of SOC in GSCs would

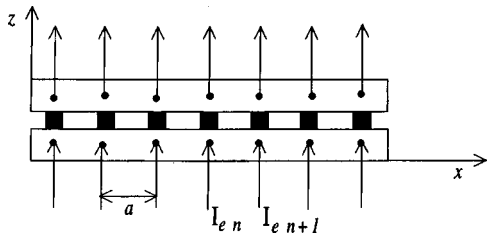

FIG. 1. Chain of SQUIDs; a is the distance between junctions, and I_{en} is the current injected into the nth junction.

make it possible to investigate this phenomenon in real systems which can be studied not only theoretically but also experimentally.

The possibility of self-organization of the CS in a GSC for $V \gg 1$ was studied in Ref. 7, where a simplified model of a GSC was introduced and studied. In constructing this model, using the characteristic physical features of the behavior of the system for $V \gg 1$, the system of differential equations for the gauge-invariant phase difference across the junctions was replaced by a system of mappings (equations with discrete time) for the currents flowing through the junctions. It was found that for a two-dimensional multijunction SQUID the system of mappings obtained is equivalent to the classic model for studying SOC — the Abelian sandpile model (ASPM).[8] Thus it has been shown that in a simplified model of a multjunction SQUID described by a system of mappings the critical state is self-organized.

However, the behavior of real GSCs is described by differential equations, and it is impossible to draw a conclusion about the existence of SOC in these systems on the basis of only a simplified model, since the simplifications introduced can result both in a loss of some properties of the initial system and in the appearance of new qualities which are not characteristic of the initial system. Therefore the problem of investigating the critical state of GSCs on the basis of a system of differential equations for the phase difference and the question of the degree to which the simplified model reflects the real behavior of the initial system remain. In the present letter we study both problems for the example of a one-dimensional GSC (chain of SQUIDs).

We show on the basis of a system of differential equations for the phase difference that the CS in a chain of SQUIDs is self-organized. We also demonstrate that the behavior of the simplified model described by a system of mappings is completely equivalent to that of the initial system described by differential equations.

The chain of SQUIDs consists of two superconducting plates, which are of infinite extent along the y axis and are connected with one other by Josephson junctions at the points with coordinates $x = an, n = 1, \ldots, N$ (Fig. 1).[9] The system of equations for the gauge-invariant phase difference φ_n across the junctions can be written in dimensionless form as[2]

$$V \sin \varphi_n + \tau \frac{\partial \varphi_n}{\partial t} = -2\varphi_n + \varphi_{n+1} + \varphi_{n-1} + 2\pi F_{en}, \quad n \neq 1, \; N;$$

$$V\sin\varphi_1+\tau\frac{\partial\varphi_1}{\partial t}=-\varphi_1+\varphi_2+2\pi F_{e1},$$

$$V\sin\varphi_N+\tau\frac{\partial\varphi_N}{\partial t}=-\varphi_N+\varphi_{N-1}+2\pi F_{eN},$$

$$V=2\pi\frac{4\pi aSj_c}{\Phi_0},\quad F_{en}=\frac{4\pi j_{en}aS}{\Phi_0},\quad \tau=\frac{4\pi aS}{\rho},\tag{1}$$

where j_c is the critical Josephson current density, ρ is the surface resistance of a junction, j_{en} is the density of the injection current in a junction, and S is the area of the cell between two junctions. The parameter V is the most important characteristic of the system, and in what follows we shall assume that $V\gg 1$. Under this condition each of the SQUIDs in our system has a large number of metastable states.[9]

For $V\gg 1$ we introduce (as in Refs. 7 and 10) for the dimensionless currents through the junctions

$$z_n=\frac{V}{2\pi}\sin\varphi_n+\frac{\tau}{2\pi}\frac{\partial\varphi_n}{\partial t},$$

a system of mappings of the form[7]

$$\begin{aligned}z_n(k+1)=z_n(k)-2[\theta[z_n(k)-z_c]-\theta[-z_n(k)-z_c]]+[\theta[z_{n+1}(k)-z_c]\\ -\theta[-z_{n+1}(k)-z_c]]+[\theta[z_{n-1}(k)-z_c]-\theta[-z_{n-1}(k)-z_c]\\ +(F_{en}(k+1)-F_{en}(k)),\quad n\neq 1,\ N;\end{aligned}$$

$$\begin{aligned}z_1(k+1)=z_1(k)-[\theta[z_1(k)-z_c]-\theta[-z_1(k)-z_c]]\\ +[\theta[z_2(k)-z_c]-\theta[-z_2(k)-z_c]]+(F_{e1}(k+1)-F_{e1}(k));\end{aligned}$$

$$\begin{aligned}z_N(k+1)=z_n(k)-[\theta[z_N(k)-z_c]-\theta[-z_N(k)-z_c]]\\ +[\theta[z_{N-1}(k)-z_c]-\theta[-z_{N-1}(k)-z_c]]+(F_{eN}(k+1)-F_{eN}(k)),\end{aligned}\tag{2}$$

where $z_c=V/2\pi$ is the dimensionless critical current, $\theta[z]$ is the Heaviside θ function, k is a discrete time, and F_{en} is the same as in Eq. (1).

The system (2) can be rewritten in the form of algorithms which are ordinarily used to write down the equations describing the dynamics of systems in problems with SOC.[5] The system of mappings (2) for the currents is an extension, to the case of two thresholds, of the algorithm for the change in the slope in the one-dimensional sandpile model studied in Refs. 11 and 12, where only one threshold value z_c was taken into account and the right-hand boundary was open, i.e., $z_{N+1}=0$. In Refs. 11 and 12 it was shown that the possibility of obtaining SOC in the one-dimensional case depends on the way of perturbing the system. We shall determine the appropriate perturbation for our system.

It has been shown for the system studied in Refs. 11 and 12 that SOC is realized if the following perturbation is used. If all $z_n<z_c$, then

$$z_m\to z_m+h;\quad z_{m+1}\to z_{m+1}-h,\tag{3}$$

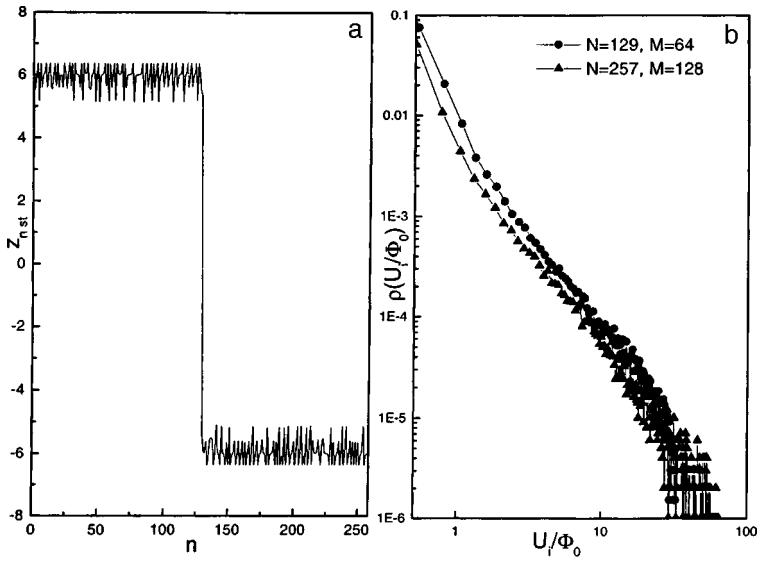

FIG. 2. a: One of the metastable states that comprise the critical state of a chain of SQUIDs. b: Probability density of U_i/Φ_0 for chains of SQUIDss of sizes $N=257$ and $N=129$; $\rho(U_i/\Phi_0)\approx(U_i/\Phi_0)^{\alpha}$, where $\alpha\approx-1.75$ for $N=257$ and $\alpha\approx-1.80$ for $N=129$.

where m is a randomly chosen site, $m\neq N$, and $h=1/2$. We shall extend this perturbation scheme to our case, where the action on the system in the metastable state is described by injection currents. Then, for the mappings (2) the perturbation scheme (3) means that we must take $F_{en}(k+1)-F_{en}(k)=0$ for all n if $|z_n(k)|>z_c$ on at least one junction and $F_{em}(k+1)-F_{em}(k)=1/2$ and $F_{em+1}(k+1)-F_{em+1}=-1/2$ if the system is in a metastable state. Here m is a randomly chosen junction; $m\neq N$;

For the system of differential equations (1) this perturbation scheme gives the following rule. If the system is in a metastable state, then

$$F_{em}\rightarrow F_{em}+1/2; \quad F_{em+1}\rightarrow F_{em+1}-1/2. \tag{4}$$

Using the perturbation described by expression (4) and computer simulation with $V=40$ and $\tau=1$, we studied the CS of a chain of SQUIDs described by the system (1) in the following regime. Starting in a state where all $\varphi_n(0)=0$, we perturb the system by injecting a current according to the rule (4). Then we allow the system to relax completely to a metastable state according to Eqs. (1) with fixed values of the injection currents, after which we perturb the system once again according to (4), and so on. In our calculations we assumed that the system has completely relaxed if all $\partial\varphi_n/\partial t<10^{-8}$.

As a result, we observed that the critical state arising in the system after the transient period is a collection of metastable states which pass into one another and in which the values of the dimensionless currents $z_{nst}=z_c\sin\varphi_n$ on the left-hand side of the array are positive and close to the critical values z_c, while on the right-hand side they are negative and close to $-z_c$ (Fig. 2a). This picture is reminiscent of the critical state in the Bean model, but in the latter model there is only one metastable state into which the system returns each time after a successive perturbation. In our case, however, after the pertur-

bation the system relaxes to a different metastable state in which the separation into ''positive'' and ''negative'' parts remains but the values of the currents in the junctions change somewhat. This behavior is characteristic for systems with self-organization.

We note that the separation of the system into positive and negative parts does not arise in the case of a one-dimensional sandpile,[11,12] though both positive and negative slopes also occur there. In our case the separation is due to the fact that the system contains two threshold values of the currents. An interesting feature of our system is that the separation occurs despite the fact that the positive and negative currents are injected into randomly chosen junctions.

To check whether or not the critical state is self-organized, in the sandpile problem the size of avalanches is calculated according to the formula

$$T_i = \frac{1}{N} \sum_{n=1}^{N} \sum_{k=k_{bi}}^{k_{ei}} \theta(z_n(k) - z_c), \tag{5}$$

where k_{bi} is the time at which the ith avalanche starts and k_{ei} is the time at which this avalanche ends. If the probability density $\rho(T_i)$ is described by a power law, then the system is self-organized.

Introducing an analogous quantity for our case, we shall study only the positive part of the system. This is because, as one can see from Eqs. (1), our system is closed, i.e., one of the most important conditions for the existence of SOC — the possibility of a drain — is not satisfied. However, there exists for the positive and negative parts of the system separately a process which replaces a drain. It consists in the fact that the excess positive current, which cannot leave the system through a boundary, flows into the negative part of the system, where it annihilates with the negative current; similarly, the excess negative current is dumped into the positive part. Therefore the boundary between the positive and negative subsystems effectively plays the role of an open boundary for each subsystem. That is, the positive part is a system with one open boundary and SOC can be realized in it.

In our case we shall call an ''avalanche'' the process whereby the system arrives in a new metastable state after a successive perturbation by the method (4). In the sandpile model T_i increased by 1 each time that the slope of the pile at some site exceeded a critical value. Since in our case the analog of the slope is the current, this means that the current in some junction exceeded the critical current. The phase across that junction changes abruptly by 2π,[9] and therefore a voltage jump occurs since, according to the expression for the nonstationary Josephson effect, the voltage across the nth junction at time t can be represented in the form

$$u_n(t) = \frac{\Phi_0}{2\pi} \frac{\partial \varphi_n}{\partial t}. \tag{6}$$

That is, in our case, the analog of the quantity (5) is the integral, averaged over the positive part of the array, of the voltage with respect to the time of the avalanche:

$$U_i = \frac{1}{M} \sum_{n=1}^{M} \int_{t_{ib}}^{t_{ie}} u_n(t)\,dt, \tag{7}$$

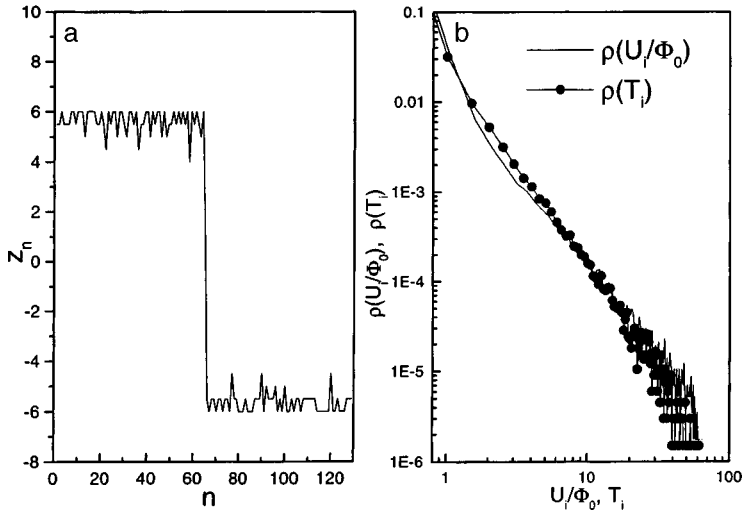

FIG. 3. a: Metastable state in a simplified model of a chain of SQUIDs. b: Probability densities of U_i/Φ_0 and T_i for the case $N=257$.

where M is the number of sites in the positive part of the array, t_{ib} is the time when the ith avalanche starts, and t_{ie} is the time when the ith avalanche ends. Then we have for U_i the expression

$$U_i=\frac{\Phi_0}{2\pi M}\sum_{n=1}^{M}[\varphi_n(t_{ei})-\varphi_n(t_{bi})]. \tag{8}$$

In the course of the numerical simulation the quantity U_i/Φ_0 was calculated for each avalanche and then the probability density $\rho(U_i/\Phi_0)$ of the quantity was calculated. Figure 2b shows $\rho(U_i/\Phi_0)$ for a chain of SQUIDs with $N=257$ and 129 junctions, the positive parts of which had sizes $M=128$ and 64, respectively. One can see that $\rho(U_i/\Phi_0)$ exhibits power-law behavior $\rho(U_i/\Phi_0)\sim(U_i/\Phi_0)^{\alpha}$($\alpha\approx-1.75$ for $N=257$, $\alpha\approx-1.80$ for $N=129$), indicating that SOC is realized in the positive part of the system.

In conclusion, we shall present the results of a comparison of the behavior of the simplified model described by the system of mappings (2) and the initial system described by Eqs. (1). We studied the model (2) in the same regime and using the same perturbation scheme as in the case of the initial system (1). The structure of the critical state arising in this case is completely analogous to that observed using differential equations to describe the system (Fig. 3a). We also calculated the probability density of T_i for the positive part of the system in the simplified model and compared it with the probability density obtained for U_i/Φ_0 in the case that the system is described by differential equations. The results are presented in Fig. 3b. The agreement obtained shows that the simplified model reflects exactly the basic features of the behavior of the initial system and belongs to the same universality class, while the simplifying assumptions made in Ref. 7 do not lead to a loss of the basic properties of the initial system by the model.

The main results of this work can be formulated as follows.

First, it was established on the basis of a system of differential equations for the phase difference that the critical state in a chain of SQUIDs is self-organized. A physical system which can be realized experimentally and in which SOC exists has thereby been described. The result obtained is important in connection with the fact that commercial production of Josephson-junction arrays has become possible in the last few years, and it is hoped that the system described will become a convenient experimental object for the practical study of SOC.

Second, it was shown that the simplified model of a chain of SQUIDs, which is a generalized sandpile model, and the initial system described by differential equations belong to the same universality class.

We also note that in our case SOC is realized in a closed system on account of the existence of an annihilation process which effectively replaces a drain. This situation will be examined in greater detail in subsequent works.

We thank O. V. Gerashchenko and M. A. Pustovoĭt for valuable remarks.

This work was supported by the Scientific Council for the direction ''Superconductivity'' of the program ''Topical Problems in Condensed-Matter Physics'' and was performed as part of Project No. 96021 ''Profile.'' The work was also supported by the subprogram ''Statistical Physics'' of the State Science and Technology Program ''Physics of Quantum and Wave Processes'' as part of Project VIII-3 and by the State Program ''Neutron Investigations of Matter.''

[1] D.-X. Chen, J. J. Moreno, and A. Hernando, Phys. Rev. B **53**, 6579 (1996).
[2] D.-X. Chen, A. Sanches, and A. Hernando, Phys. Rev. B **50**, 10342 (1994).
[3] A. Manjofer and T. Wolf, Phys. Rev. B **47**, 5383 (1993).
[4] C. P. Bean, Rev. Mod. Phys. **36**, 31 (1964).
[5] P. Bak, C. Tang, and K. Wisenfeld, Phys. Rev. Lett. **59**, 381 (1987).
[6] G. A. Held, D. H. Solina, II, D. T. Keane *et al.*, Phys. Rev. Lett. **65**, 1120 (1990).
[7] S. L. Ginzburg, Zh. Éksp. Teor. Fiz. **106**, 607 (1994) [JETP **79**, 334 (1994)].
[8] D. Dhar, Phys. Rev. Lett. **64**, 1613 (1990).
[9] K. K. Likharev, *Introduction to the Dynamics of Josephson Junctions and Circuits*, Gordon and Breach, New York, 1986 [Russian original, Nauka, Moscow, 1985].
[10] S. L. Ginzburg, M. A. Pustovoit, and N. E. Savitskaya, Phys. Rev. E **57**, 1319 (1998).
[11] L. Kadanoff, S. R. Nagel, L. Wu, and S.-M. Zhou, Phys. Rev. A **39**, 6524 (1989).
[12] S. T. R. Pinho, C. P. C. Prado, and S. R. Salinas, Phys. Rev. E **55**, 2159 (1997).

Translated by M. E. Alferieff

Prismane C_8: a new form of carbon?

L. A. Openov and V. F. Elesin
Moscow State Engineering Physics Institute, 115409 Moscow, Russia

(Submitted 7 July 1998; resubmitted 22 September 1998)
Pis'ma Zh. Éksp. Teor. Fiz. **68**, No. 9, 695–699 (10 November 1998)

Our numerical calculations on small carbon clusters point to the existence of a metastable three-dimensional eight-atom cluster C_8 which has a shape of a six-atom triangular prism with two excess atoms above and below its bases. We gave this cluster the name ''prismane.'' The binding energy of prismane is 5.1 eV/atom, i.e., 0.45 eV/atom lower than the binding energy of the stable one-dimensional eight-atom cluster and 2.3 eV/atom lower than the binding energy of bulk graphite or diamond. Molecular dynamics simulations give evidence for a rather high stability of prismane, the activation energy for prismane decay being about 0.8 eV. The prismane lifetime increases rapidly as the temperature decreases, indicating the possibility of experimental observation of this cluster.
[S0021-3640(98)00821-4]

PACS numbers: 36.40.Mr, 36.40.Qv

Carbon is known to form a rich variety of crystal structures due to its ability to exist in different valence states. As a result, coordination numbers in carbon compounds range from two (e.g., carbyne), through three (e.g., graphite) to four (e.g., diamond), while typical (''favorable'') values of the angles between covalent bonds are 180° in carbyne, 120° within graphite layers, and 109° 28′ in diamond. The recent discovery of the C_{60} molecule[1] and synthesis of C_{60} clusters in macroscopic quantities[2] have stimulated a renewed interest in carbon nanostructures.[3] A carbon nanostructure may be viewed as a graphite layer transformed into a tube (nanotube), a ball (fullerene), etc., except for the fact that such nanostructures usually comprise pentagons along with hexagons.

The discovery of cubane C_8H_8 (Ref. 4) has turned out to be very important from a fundamental viewpoint, since the carbon atoms in the C_8H_8 molecule are located at the corners of a cube, so that the angles between the C–C bonds is equal to 90°, in contrast to the majority of carbon compounds. As a consequence of ''energetically unfavorable'' bond angles, the molecule C_8H_8 is metastable and stores a considerable amount of energy.[4] Its cubic structure is stabilized by the corner hydrogen atoms. This raises the question as to whether there exist stable or metastable three-dimensional clusters that are composed of carbon atoms only and have 90° bond angles.

Another interesting question discussed in the literature[5–8] is, ''what is the minimum number of atoms in stable and metastable *three-dimensional* carbon clusters?'' It must be emphasized that while there has been substantial progress in studies of relatively large

carbon nanoparticles C_N composed of $N\sim 100$ carbon atoms,[3] there is still controversy concerning the structure and energetics of small carbon clusters with $N\sim 10$, e.g., whether the stable C_4, C_6, and C_8 clusters are cyclic or linear.[5] Three-dimensional carbon clusters (cages) are believed to be stable for $N\geqslant 20$ only,[6–8] while for clusters with $N<20$ the stable structures are one-dimensional linear chains or monocyclic rings.[5–7] A characteristic feature of small carbon clusters is the existence of metastable states whose binding energies are lower than the binding energy of the stable cluster with the same N. For $N<14$, the metastable structures are either one-dimensional (chains and rings) or two-dimensional (graphite flakes); see, e.g., Ref. 6. To our knowledge, up to now there has been no experimental or theoretical evidence for either stable or metastable *three-dimensional* carbon clusters with $N<14$ (the occurrence of a metastable C_{14} cage has been reported,[8] based on the results of density functional calculations).

The purpose of this work was to search for metastable three-dimensional clusters C_N with $N<14$ by means of numerical simulation. One such cluster, C_8, was found. Here we report the numerically calculated structural and energy characteristics of this cluster, whose lifetime turns out to be surprisingly long due to the rather high value of its activation energy, about 0.8 eV.

We have carried out TBMD (tight-binding molecular dynamics) simulations of small carbon clusters, making use of a transferable tight-binding potential recently developed for carbon by Xu *et al.*[7,9] This numerical technique allows one to calculate the total energy of a cluster having an arbitrary atomic configuration. It had been proven to reproduce accurately the energy-versus-volume diagram of carbon polytypes and to give a good description of both small clusters and bulk structures of carbon.[7,9] We have checked that this technique describes the structure and energetics of small carbon clusters quite well, the difference in bond lengths and binding energies between our results and available *ab initio* calculations[5] usually not exceeding 10%.

The binding (cohesive) energy $E_{\mathrm{coh}}(N)$ of an N-atom cluster C_N was defined as (see, e.g., Ref. 6)

$$E_{\mathrm{coh}}(N)=NE(1)-E(N), \tag{1}$$

where $E(N)$ is the total energy of the cluster and $E(1)$ is the energy of an isolated carbon atom. A positive value of E_{coh} points to stability of the cluster against its fragmentation into N carbon atoms. At a given N, there may exist several atomic configurations having $E_{\mathrm{coh}}>0$. The cluster with the highest value of E_{coh} is stable, while the clusters with lower (but positive) values of E_{coh} are metastable. A metastable cluster can transform to the stable, energetically favorable configuration. The characteristic time of such a process (the lifetime τ) depends on the height of the energy barrier separating the metastable and stable configurations.

We have thoroughly analyzed a number of atomic configurations as possible candidates for metastable three-dimensional carbon structures. However, all of them (with one exception that constitutes the essence of this paper; see below) turned out to be unstable and transformed to one-dimensional clusters or decayed into small fragments even at $T\to 0$. In particular, we have checked for the possible existence of a three-dimensional cluster C_8 having a cubic structure (by analogy with cubane C_8H_8),[4] but we found that such a cluster is unstable. Nevertheless, we discovered that the eight-atom cluster C_8 can

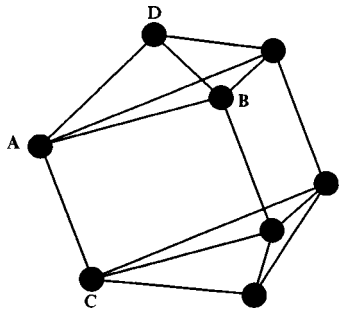

FIG. 1. Prismane C_8. Bond lengths: $d_{AB}=2.31$ Å, $d_{AC}=1.28$ Å, $d_{AD}=1.47$ Å. Bond angles: $\angle BAC=90°$, $\angle ADB=104°$, $\angle ABE=60°$.

exist as a three-dimensional cluster having the shape of a six-atom triangular prism with two excess top atoms above and below its bases. We gave this cluster the name ''prismane.'' It is shown in Fig. 1.

The binding energy of prismane is $E_{\rm coh}(8)/8=5.1$ eV/atom. This is 0.45 eV/atom lower than the binding energy of the stable one-dimensional eight-atom cluster and 2.3 eV/atom lower than the binding energy of bulk graphite or diamond. Hence, the prismane C_8 is metastable. The lengths of C–C bonds are 2.31 Å within each base, 1.28 Å between the two bases, and 1.47 Å between each base and the nearest top atom; see Fig. 1. We note that the angle between the C–C bonds within the bases and the C–C bonds connecting the bases is 90°. This is one reason for the lower value of the binding energy of prismane relative to the binding energy of the stable one-dimensional eight-atom cluster. Meanwhile, the angle between the C–C bonds connecting the top atoms with the bases of the prism is equal to 104°, which is close to the value of bond angle in bulk diamond (109° 28′).

In order to determine the energy barrier separating the metastable prismane structure and the stable chain structure, we carried out molecular dynamics simulations of the prismane decay for different values of the initial temperature $T_{\rm ini}$. The time of one molecular dynamics step constituted $t_0=2.72\times10^{-16}$ s, about one percent of the oscillation period of the dimer C_2. The temperature T of the cluster was calculated after each 500 molecular dynamics steps according to the formula

$$\frac{3}{2}k_BT=\langle E_{\rm kin}\rangle, \tag{2}$$

where k_B is Boltzmann's constant and $\langle E_{\rm kin}\rangle$ is the kinetic energy per atom averaged over a period of time $\Delta t=500t_0$. Such a time averaging enables one to avoid strong fluctuations of T stemming from the small number of atoms in the cluster under investigation. The initial temperature $T_{\rm ini}$ was determined from Eq. (2) at $0\leqslant t\leqslant 500t_0$.

On general grounds one would expect the probability W of decay of the cluster per unit time to be given by a statistical formula

$$W=W_0\exp(-E_a/k_BT_{\rm ini}), \tag{3}$$

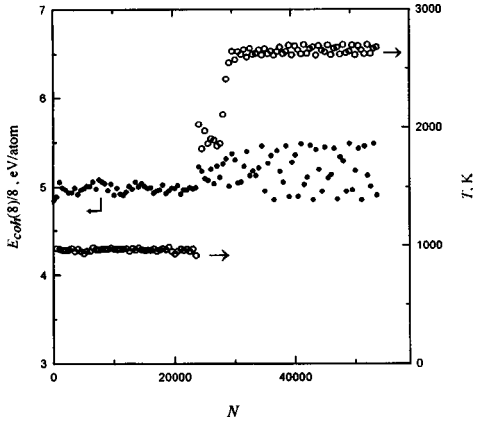

FIG. 2. Cohesive energy per atom $E_{\mathrm{coh}}(8)/8$ (closed circles) and temperature T (open circles) of the prismane C_8 versus the number of molecular dynamics steps N. The time of one step $t_0=2.72\times10^{-16}$ s. The initial temperature $T_{\mathrm{ini}}=950$ K. The prismane decays at $N_c=23500$–23700. The lifetime $\tau=N_c t_0=6.4\times10^{-12}$ s.

where the factor W_0 has dimensions of s^{-1} and E_a is the activation energy, i.e., the height of the energy barrier separating the given metastable state from the stable or some other metastable state of the cluster. The cluster lifetime τ may be defined as

$$\tau=1/W=\tau_0\exp(E_a/k_BT_{\mathrm{ini}}), \tag{4}$$

where $\tau_0=1/W_0$. Molecular dynamics simulations allow one to determine the lifetime τ directly at any particular value of T_{ini} as the time of cluster decay into another atomic configuration. It is convenient to change over from the cluster lifetime τ to the critical number of molecular dynamics steps $N_c=\tau/t_0$ which it takes for the cluster to decay:

$$N_c=N_0\exp(E_a/k_BT_{\mathrm{ini}}), \tag{5}$$

where $N_0=\tau_0/t_0$.

Figure 2 shows a typical example of the binding energy per atom, $E_{\mathrm{coh}}(8)/8$, and the temperature T of the prismane as functions of the number of molecular dynamics steps N for the case $T_{\mathrm{ini}}=950$ K. One can see that $E_{\mathrm{coh}}(8)/8$ and T fluctuate near the values 5.0 eV/atom and 950 K, respectively, over $N\approx23500$ molecular dynamics steps. The prismane preserves its form during this period of time. At $N_c=23600\pm100$ the prismane decays into the stable eight-atom chain. The temperature rises to 2600 K. Strong oscillations of the atoms within the chain with respect to one another cause $E_{\mathrm{coh}}(8)/8$ to vary in time from 4.9 eV/atom up to the binding energy of the equilibrium chain, 5.55 eV/atom.

Note, however, that the lifetime $\tau=N_c t_0=6.4\times10^{-12}$ s is rather short on a macroscopic scale, while we are interested in phenomena which happen on time scales of seconds or even months and years. According to Eq. (4), such long lifetimes are expected for temperatures much lower than the value $T_{\mathrm{ini}}=950$ K used in the simulations shown in Fig. 2. But those lifetimes are impossible to achieve by means of direct computer simulations.

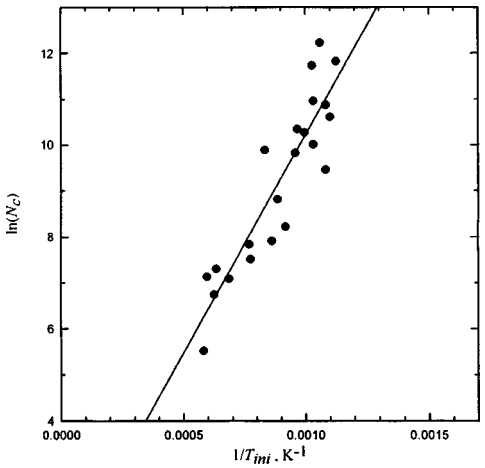

FIG. 3. Plot of the logarithm of the critical number of molecular dynamics steps N_c (corresponding to decay of the prismane) versus the inverse initial temperature $1/T_{\rm ini}$. The circles are the results of numerical calculations. The solid line is the least-squares fit $\ln(N_c)=0.7263+9496/T_{\rm ini}$, where $T_{\rm ini}$ is measured in K.

To overcome the problem, we have calculated numerically the critical values of N_c for several values of $T_{\rm ini}$ and fitted the numerical data by Eq. (5). The results are shown in Fig. 3. We stress that the process of cluster decay is probabilistic in nature. Hence, the lifetime τ is not uniquely determined at a given value of $T_{\rm ini}$. As a result, the data for $\ln(N_c)$ as a function of $1/T_{\rm ini}$ are somewhat scattered; see Fig. 3. Nevertheless one can see that the numerical data can be fitted well by a straight line over the rather wide ranges of values $N_c=300-206000$ and $T_{\rm ini}=890-1700$ K, in accordance with Eq. (5). The coefficients of this fit give the values of $N_0=2.1$ and $E_a/k_B=9500$ K in Eq. (5).

We note that the activation energy $E_a=0.82$ eV is very large, thus resulting in relatively high stability of the prismane. Indeed, since the dependence of τ on $T_{\rm ini}$ is exponentially strong, a decrease in $T_{\rm ini}$ leads to a rapid increase in τ, so that $\tau\sim 10$ μs at $T_{\rm ini}=400$ K. An important remark is in order here. Since the total energy of the cluster is conserved in our simulations, the cluster is unable to decay if the *maximum* attainable (at a given value of $T_{\rm ini}$) kinetic energy $E_{\rm kin}^{\rm max}$ of the cluster is less than E_a. In turn, $E_{\rm kin}^{\rm max}$ is twice the *time-averaged* kinetic energy at the initial stage of cluster evolution, i.e., $E_{\rm kin}^{\rm max}=2\cdot 8\cdot \frac{3}{2}k_BT_{\rm ini}=24k_BT_{\rm ini}$; see Eq. (2). Hence, at $T_{\rm ini}<E_a/24k_B\approx 400$ K the lifetime of the cluster equals infinity. Thus, in general, extrapolation of the $\tau(T_{\rm ini})$ curve to the range $T_{\rm ini}<400$ K is incorrect.

The lifetime τ is extremely sensitive to the value of the activation energy E_a, since the latter appears in the exponent; see Eq. (4). Hence, even a minor change in E_a will result in a substantial variation of τ at a given $T_{\rm ini}$. In order to refine the value of E_a it is necessary to calculate the critical values of N_c for a greater number of initial temperatures $T_{\rm ini}$. However, we believe it is unlikely that such a refinement will cause the value of E_a to change significantly.

Finally, it should be stressed that we have confirmed the existence of the three-dimensional metastable prismane structure by making use of other computer codes, e.g., MOPAC and that based on the empirical interatomic potential proposed for carbon sys-

tems by Tersoff.[10] The overall shape of the cluster (Fig. 1) turned out to be the same, while the bond lengths and the binding energy were to some extent different. So, the prismane C_8 certainly is not just an artifact of the specific simulation technique used in this study, and the values of the prismane binding energy, activation energy, and lifetimes at different temperatures may be refined by means of more-sophisticated calculations.

In conclusion, we have predicted the existence of a three-dimensional cluster C_8 (prismane) which is the smallest three-dimensional carbon cluster found so far experimentally or theoretically. This cluster turns out to be metastable and has a binding energy 0.45 eV/atom below the binding energy of the stable one-dimensional eight-atom cluster. However, molecular dynamics simulations point to a rather high stability of prismane, suggesting that this cluster may be observed experimentally.

We are grateful to A. V. Krasheninnikov and N. E. L'vov for the help in preparation of the manuscript. The work was supported in part by the Russian State Program ''Integration,'' by the International Science and Technology Center (Project #467) and by the Contract DSWA01-98-C-0001.

[1] H. W. Kroto, J. R. Heath, S. C. O'Brien *et al.*, Nature (London) **318**, 162 (1985).
[2] W. Krätschmer, L. D. Lamb, K. Fostiropoulos, and D. R. Huffman, Nature (London) **347**, 354 (1990).
[3] Yu. E. Lozovik and A. M. Popov, Usp. Fiz. Nauk **167**, 751 (1997).
[4] P. E. Eaton and G. J. Castaldi, J. Am. Chem. Soc. **107**, 784 (1985), and references therein.
[5] W. Weltner, Jr., and R. J. Van Zee, Chem. Rev. **89**, 1713 (1989).
[6] D. Tománek and M. A. Schluter, Phys. Rev. Lett. **67**, 2331 (1991).
[7] C. H. Xu, C. Z. Wang, C. T. Chan, and K. M. Ho, Phys. Rev. B **47**, 9878 (1993).
[8] R. O. Jones and G. Seifert, Phys. Rev. Lett. **79**, 443 (1997).
[9] C. H. Xu, C. Z. Wang, C. T. Chan, and K. M. Ho, J. Phys.: Condens. Matter **4**, 6047 (1992).
[10] J. Tersoff, Phys. Rev. Lett. **61**, 2879 (1988).

Published in English in the original Russian journal. Edited by Steve Torstveit.

Current filamentation in GaAs/AlGaAs heterojunctions preceding quantum-Hall-effect breakdown

S. I. Dorozhkin and M. O. Dorokhova

Institute of Solid-State Physics, Russian Academy of Sciences, 142432 Chernogolovka, Moscow Region, Russia[a)]

(Submitted 29 September 1998)
Pis'ma Zh. Éksp. Teor. Fiz. **68**, No. 9, 700–704 (10 November 1998)

Self-induced filamentation of the current near the edges of a sample in the Hall geometry has been observed in the quantum-Hall-effect regime in a two-dimensional electronic system arising near a GaAs/AlGaAs heterojunction. If in the case of integer values of the filling factor ν averaged over the sample the currents flowing along opposite edges are approximately the same, then away from such a value within the quantum plateau the current is increasingly concentrated near that edge of the sample where the local value of ν is closer to being an integer. When the direction of the magnetic field or of the current changes, the filament switches to the opposite edge of the sample. © *1998 American Institute of Physics.* [S0021-3640(98)00921-9]

PACS numbers: 73.20.Dx, 73.40.Hm, 75.70.Cn

The integer-quantum-Hall-effect (QHE) state, characterized by virtually dissipation-free Hall current flow and quantization of the Hall resistance in units of h/e^2, occurs when the Fermi level at the center of the sample lies in a gap between delocalized electronic states belonging to different Landau levels. The question of the distribution of the currents in the QHE state is fundamental for explaining this effect. This is because two different approaches exist. One approach (see, for example, Ref. 1) assumes that the current is transported by delocalized electronic states lying below the Fermi level. In this case, on scales exceeding the magnetic length a local relation exists between the electric field and the current density. In the other approach[2] it is assumed that the entire current is transported by regions on the sample edges, where the delocalized states emerge at the Fermi level. In this approach the current is determined only by a different filling of the delocalized states on opposite edges of the sample. In principle, these two approaches can be mutually complementary,[3] though in this case there arises the question of the relation between the volume and edge currents. A phenomenological modification of the first approach are self-consistent calculations[4–6] of the distributions of the electric field, electron, and current densities, employing a model form of the magnetoconductivity tensor.

We have performed measurements of the potential distribution across the conducting channel of a Hall bridge fabricated on the basis of a selectively silicon-doped GaAs/AlGaAs heterostructure in which a two-dimensional electronic system arises near the GaAs/AlGaAs junction, which lies about 1000 Å below the surface of the sample.

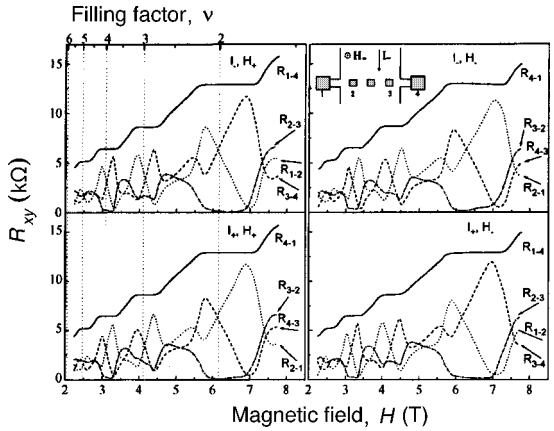

FIG. 1. Magnetic field dependence of the dc voltage drop, converted to the corresponding Hall resistance $R_{i-j}(I_0=5\mu\text{A})$, between different potential contacts. Here i and j are the numbers of the contacts (see the inset); the first number corresponds to the contact with the highest potential. The results presented in different parts of the figure correspond to different orientations of the magnetic field and the dc current, designated by the indices + and −. Negative directions for the corresponding quantities are defined in the inset, where the arrangement of the contacts (indicated by the rectangles) is also shown; $T=1.5$ K.

The two-dimensional electron density is $n_s=3.0\times10^{11}$ cm^{-2} and the mobility at liquid-helium temperatures is $\mu=5\times10^5$ cm^2/V·s. The measurements were performed using potential contacts placed inside the channel (see the inset in Fig. 1). The channel width was 240 μm and the area of the internal contact pads was 40×60 μm, the short side of a pad being oriented across the channel. Contacts to the layer were produced by diffusing the material of a layered structure formed by depositing Ni and Au/Ge films, 400 Å and 2000 Å thick, respectively, on the sample surface. Diffusion was accomplished by heating the sample to 450 °C for ~90 s. The measurements were performed in dc and ac currents in a magnetic field perpendicular to the plane of the two-dimensional system at temperature 1.5 K. The voltage signal from the contacts was amplified by a wide-band amplifier with input impedance $10^8\Omega$. Two types of energy splittings exist in the experimental material — cyclotron and spin, the latter being much smaller than the former. The Fermi level falls at them for even and odd filling factors of the magnetic levels, respectively. The main results of this work were obtained for Hall plateaus at filling factors of 2 and 4.

We note first that the measurements of the potential distribution in the QHE regime by means of internal contacts are extremely difficult to perform because of the contact resistance, which is proportional to the reciprocal σ_{xx}^{-1} of the dissipative conductivity in the region near the contact and is ordinarily very large. We avoided this problem by limiting ourselves to measurements of the potential distribution for comparatively large values of the dc current I_0 through the sample (several μA), at which the resistances of the internal contacts decreased substantially (see the inset in Fig. 2) and did not distort the results. It is important that such currents did not destroy the QHE states at even filling factors 2 and 4 (Fig. 2). The substantial growth of the magnetoresistance R_{xx} for nonintegral filling factors is probably due to QHE breakdown at the nondissipative edges of the strips (see Ref. 7 for a more detailed discussion). The magnetic field dependences of the

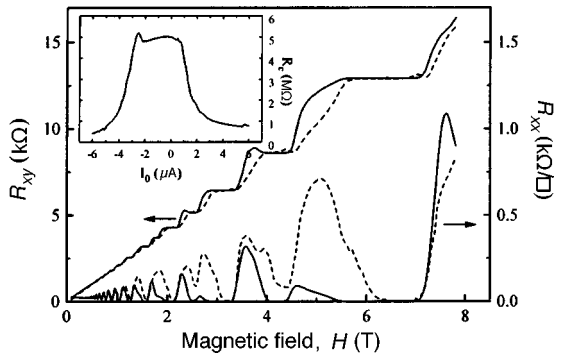

FIG. 2. Magnetic field dependence of the magnetoresistance R_{xx} and the Hall resistance R_{xy}, measured with a 0.04 μA ac current (solid curves) and a 5 μA dc current (dashed curves). Inset: Resistance R_c measured between contacts *1* and *2* as a function of the dc current through the sample for a 9 Hz ac current with a 10 mV voltage applied between these contacts; $H=6.37$ T ($\nu=1.94$).

voltage drop between different pairs of contacts are shown in Fig. 1. It is easy to see from these data that near the edges of the plateau of the Hall resistance measured between the contacts *1* and *4* most of the voltage falls between one of these contacts and the internal contact closest to it. This effect is most clearly seen near the right-hand edges of the plateau. Curiously, the effect is much stronger for the additional voltage arising upon a weak modulation of the current through the sample (Fig. 3). A transition from one edge of the plateau to the other and also a change in the signs of the current or magnetic field cause the region of the main voltage drop to move from one edge of the sample to the other. Two important facts should be noted. First, within the Hall resistance plateau the voltage drop between the two internal potential contacts *2* and *3* is close to zero. Second, near an integer filling factor the voltage drops near the opposite edges of the sample are approximately the same. All dependences presented in Fig. 1 are summarized together in Fig. 4a. They cluster in groups of four near the four universal curves. The correctness of

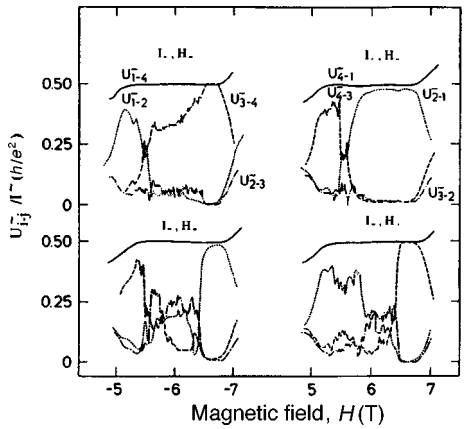

FIG. 3. Same as in Fig. 1 for the voltage drop of an ac current in the region of the plateau with $\nu=2$ with a dc current $I_0=6$ μA and an ac current 0.1 μA.

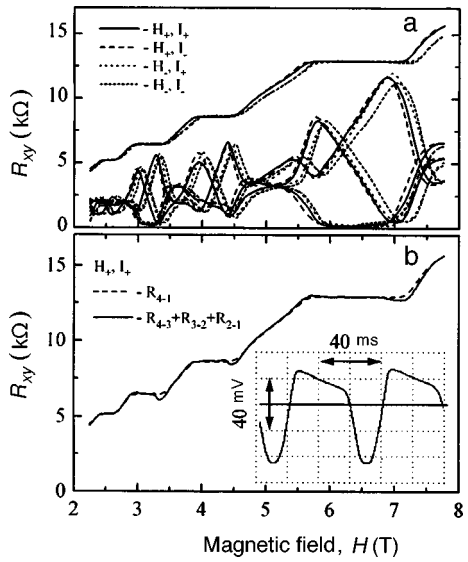

FIG. 4. a: Data of Fig. 1 plotted together in the same figure. The different types of lines correspond to different directions of the magnetic field and current, explained in the figure. b: Comparison of the sum of the voltage drops measured with internal contacts (solid curve) with the total Hall voltage across the sample (dashed curve) for positive orientations of the field and current (according to the data of Fig. 1). Inset: Oscillogram of the ac voltage measured between contacts *1* and *2* with a 3 μA ac current at a frequency of 16 Hz passed through the sample.

our measurements performed with internal contacts is confirmed by comparing the total Hall voltage across the sample, calculated as the sum of the voltages measured with internal contacts, with the voltage measured between contacts *1* and *4* (see Fig. 4b). We thought it would also be interesting to look at the nonlinear properties of the sample with an ac current of sufficiently large amplitude. An example of such measurements is shown in the inset in Fig. 4b. We note that the observed asymmetric shape of the signal remained up to frequencies of about 1 kHz.

It seems obvious to us that the region of maximum voltage drop should be identified with a Hall current filament. We shall discuss first the current filamentation, occurring near the edges of the Hall plateau, near one edge of the sample. The displacement of the filament from edge to edge of the sample indicates that the filamentation effect is not associated with the initial inhomogeneity of the sample. An additional confirmation of this is the closeness of the signals measured near different edges of the sample with opposite polarities of the current or field (Fig. 4a). On the basis of a simple qualitative analysis of the redistribution of the electron density in the sample that is required for producing the Hall potential difference, it is easily shown that in our experiment the current filament is always located near that edge of the sample where the filling factor is closer to an integer value. This rule describes all observed displacements of the filament. This result can be easily explained qualitatively on the basis of the considerations presented in Ref. 4, where the filamentation effect was predicted. Indeed, in a Hall bridge the relation between the current density j_x along the channel and the electric field E_x in the same direction has the form $j_x = E_x/\rho_{xx}$. In a long sample the variations of the field E_x

across the channel (in the y direction) are expected to be negligible on the basis of the condition $\nabla \times \mathbf{E} = 0$. As is well known, in the QHE regime ρ_{xx} can vary by several orders of magnitude with a small change in the filling factor, having a deep minimum at an integer value of the filling factor. In the case of a nonuniform electron density across the channel the current will contract into a filament at the location where the filling factor is an integer. The Hall electric field $E_y = \rho_{xy} j_x = \rho_{xy} E_x / \rho_{xx}$ will have a maximum at the same location. These considerations are confirmed by calculations both for field-effect transistors[4,5] and for gateless two-dimensional systems.[6] Therefore the current filamentation observed near one edge of the sample at the edges of a plateau can easily be explained by the y dependence of ρ_{xx} due to the redistribution of the electron density across the channel which is required for producing the Hall voltage. We note that despite the large number of investigations of the potential distribution in GaAs/AlGaAs heterostructures in the QHE regime which have been performed by different methods (see, for example, Refs. 8–11), this effect has not been previously observed in pure form in this system. Indirect evidence of filamentation and displacement of a filament from one edge of the sample to another has been obtained only for field-effect transistors,[12,13,5] where in contrast to gateless heterostructures the relation between the potential and the electron density is of a local character and has a simple form.

Calculations[4–6] predict, however, that in the case of integer average value of the filling factor the filament should be located at the center of the sample. This is not observed in our experiment. This experimental result, incidentally, agrees with observations in Ref. 10 performed on GaAs/AlGaAs heterostructures using a method based on the rotation of the plane of polarization of light by optically active GaAs. It should be noted, however, that we cannot assert today that the presence of filaments at two edges of the sample cannot be a consequence of the initial inhomogeneities in our sample (for example, inhomogeneities resulting from the fabrication of the internal contacts) for which the sample parameters at the center of the channel between the contacts *2* and *3* are worse than at the edges. Some arguments against this possibility are the quite uniform current distribution across the sample in regions where the filling factors fall between different quantum plateaus and the effect of the current on the resistance of the internal contacts.

Current concentration at two edges of a sample with an integer filling factor everywhere has been obtained in a quantum-mechanical calculation[1] that takes into account the nonzero compressibility of the electronic system in crossed electric and magnetic fields. However, at present it is unclear how this approach can be transferred to noninteger values of the filling factor found within a plateau. We also note that the calculations based on the use of the magnetoconductivity tensor can be improved by taking into account the diffusion (which is proportional to the chemical potential gradient) of the current.[14,15] It is possible that this will improve the agreement between the calculations and our data for integer filling factors.

We gratefully acknowledge support from project No. 98-02-16633 of the Russian Foundation for Basic Research and the State Science and Technology Program ''Statistical Physics.'' S. I. D. and M. O. D. are grateful to the RFBR–PICS Foundation (Grant 98-02-22037) and the Soros Foundation, respectively, for stipends. We would also like to thank V. T. Golgopolov for helpful discussions of the questions considered in this letter.

[a)]e-mail: dorozh@issp.ac.ru

[1] A. H. MacDonald, T. M. Rice, and W. F. Brinkman, Phys. Rev. B **28**, 3648 (1983).
[2] M. Buttiker, Phys. Rev. B **38**, 9375 (1988).
[3] D. J. Thouless, Phys. Rev. Lett. **71**, 1879 (1993).
[4] V. M. Pudalov and S. G. Semenchinskiĭ, JETP Lett. **42**, 232 (1985).
[5] A. A. Shashkin, V. T. Dolgopolov, and S. I. Dorozhkin, Zh. Éksp. Teor. Fiz. **91**, 1897 (1986) [Sov. Phys. JETP **64**, 1124 (1986)].
[6] M. I. Dyakonov and F. G. Pikus, Solid State Commun. **83**, 413 (1992).
[7] S. I. Dorozhkin, S. Koch, K. von Klitzing, and G. Dorda, JETP Lett. **52**, 652 (1990).
[8] G. Ebert, K. von Klitzing, and G. Weimann, J. Phys. C **18**, L257 (1985).
[9] H. Z. Zheng, D. C. Tsui, and A. M. Chang, Phys. Rev. B **32**, 5506 (1985).
[10] P. F. Fontein, J. A. Kleinen, P. Hendriks *et al.*, Phys. Rev. B **43**, 12090 (1991).
[11] R. Knott, W. Dietsche, K. von Klitzing *et al.*, *Proceedings of the 11-th International Conference on ''High Magnetic Fields in the Physics of Semiconductors,''* edited by D. Heiman, World Scientific, 1994, p. 122.
[12] S. I. Dorozhkin, A. A. Shashkin, N. B. Zhitenev, and V. T. Dolgopolov, JETP Lett. **44**, 241 (1986).
[13] S. G. Semenchinskiĭ, Zh. Éksp. Teor. Fiz. **91**, 1804 (1986) [Sov. Phys. JETP **64**, 1068 (1986)].
[14] G. V. Kravchenko, *Diploma Dissertation* [in Russian], Moscow Physicotechnical Institute (1990); V. T. Dolgopolov, private communication.
[15] V. B. Shikin, JETP Lett. **66**, 581 (1997).

Translated by M. E. Alferieff

On the origin of quantum oscillations in the mixed state of an anisotropic superconductor

L. P. Gor'kov

National High Magnetic Field Laboratory, Florida State University, Tallahassee, FL 32310; L. D. Landau Institute of Theoretical Physics, Russian Academy of Sciences, 117334 Moscow, Russia

(Submitted 5 October 1998)
Pis'ma Zh. Éksp. Teor. Fiz. **68**, No. 9, 705–710 (10 November 1998)

For the vortex lattice in an anisotropic superconductor with well-separated cores ($H_{c1} \ll B \ll H_{c2}$) it is shown that sizable de Haas–van Alphen oscillations are caused by the levels' crossing of the energy threshold separating localized and extended states of excitations moving in the average magnetic field B. © *1998 American Institute of Physics.* [S0021-3640(98)01021-4]

PACS numbers: 74.25.Ha

Recent experiments[1,2] show that the de Haas–van Alphen (dHvA) effect persists in the superconducting (SC) state for magnetic fields B as low as $B \sim (0.3–0.4)H_{c2}$. The effective SC gap Δ at such fields is large enough to preclude motion of an electron along a closed Larmor orbit with a radius $r_L \sim v_F/\omega_c$ very much larger than the coherence length ξ_0 and the intervortex distance d (Ref. 3). The dHvA signal is expected to weaken exponentially as $\exp(-\Delta/\omega_c)$ (Ref. 4). In what follows we suggest a new mechanism for the quantum oscillations in the mixed SC state.

In the normal state the dHvA effect is brought about by levels crossing the chemical potential μ as the field is varied. The oscillations are periodic in B^{-1} because a minor field change, $\Delta B/B \sim \omega_c/\mu$, is enough to push a level across μ.

The SC excitations will have an electron- or hole-like character, depending on the extent to which their energy exceeds the gap. Even for a ''d-wave'' superconductor[5] the levels cannot cross the chemical potential. In this sense, there is no difference between a ''d-wave'' or any other anisotropic SC.

It is shown below that a new energy threshold takes over the role of the chemical potential in the SC state. Consider, for example, an anisotropic superconductor with a spectrum $\varepsilon(\mathbf{p}) = \sqrt{v_F^2(p-p_F)^2 + |\Delta(\mathbf{p})|^2}$. Assume, for simplicity, that the gap $\Delta(\mathbf{p})$ has only one maximum, $\Delta_{\max}$, and one minimum, $\Delta_{\min}$, along the Fermi surface (FS). Excitations with $\varepsilon(\mathbf{p}) > \Delta_{\max}$ have itinerant behavior, while at $\Delta_{\max} > \varepsilon(\mathbf{p}) > \Delta_{\min}$ this is only true for excitations with a proper $\mathbf{p}$. The latter become localized in a magnetic field, for the Lorentz force changes the $\mathbf{p}$ direction. Excitations with energies larger than $\Delta_{\max}$ may move along an extended Larmor orbit.

To pose this phenomenon as a theoretical problem, consider the limit of well-separated vortices $d \gg \xi_0 (H_{c1} \ll B \ll H_{c2})$. The vortex cores occupying only a minor frac-

tion of the volume may be neglected. A typical electron trajectory would run across the ''bulk,'' where the gap amplitude is saturated:

$$\Delta(\mathbf{p},\mathbf{r}) \cong \Delta(\mathbf{p})\exp(i\varphi(\mathbf{r})). \tag{1}$$

The method[5] used to treat the problem is based on averaging the Gor'kov system of Green functions over quasiclassical trajectories[6] (all notation below is from Ref. 5). The Green functions are presented in terms of the position φ of an electron along the FS. The essence of the method is given by Eqs. (23)–(28) of Ref. 5. After the Gor'kov matrix is diagonalized, the whole problem reduces to solving the following Schrödinger equation:

$$-\omega_c^2 y'' + [\Delta^2(\varphi) - \omega_c \Delta'(\varphi)]y = E^2 y. \tag{2}$$

The term $-\omega_c \Delta'(\varphi)$ plays no role and will be omitted. In (2) we have also left out the term $h(\varphi)$ from Eq. (31) of Ref. 5. The Doppler shift given by Eq. (31) of Ref. 5 is essential for the magnitude of the effect and will be taken into account later.

The eigenfunctions are given by solutions of (2) satisfying the periodicity condition $(\varphi \to \varphi + 2\pi)$ for

$$y(\varphi)e^{-i\kappa\varphi}, \tag{3}$$

where $\kappa = \overline{\mu}/\omega_c$ comes from writing the chemical potential in the form[5]

$$\mu = \omega_c N_0 + \overline{\mu}. \tag{4}$$

For large μ one has $N_0 \gg 1$, and the specific N_0 does not affect the pattern of periodic (in B^{-1}) oscillations of the magnetization, which depends on κ in the interval (0,1). Equations (2) and (3) go over to the problem of finding the band structure for a particle moving in the periodic potential $\Delta^2(\varphi)$ with κ as a quasimomentum.

We rewrite (2) in the form

$$-\omega_c^2 y'' + (\Delta^2(\varphi) - \Delta_{\max}^2)y = (E^2 - \Delta_{\max}^2)y) \tag{2'}$$

and consider (2′) first in the quasiclassical WKB approximation $(\omega_c \ll \Delta)$. For $|E| \gg \Delta$ the periodicity of (3) leads to the spectrum of free electrons in the magnetic field: $E_n = \omega_c n + \overline{\mu}$. For $E^2 - \Delta_{\max}^2 < 0$ the attractive potential in (2′) has many $(\Delta/\omega_c \gg 1)$ ''localized'' levels (tunneling across the barrier is neglected). The boundary separating the ''extended'' and ''localized'' states in the WKB sense lies at $\Delta_{\max}$. We introduce in Eq. (2′)

$$E^2 - \Delta_{\max}^2 \simeq 2\Delta_{\max}(-\varepsilon) \tag{5}$$

for $|E|$ close to $\Delta_{\max}$. The WKB solutions are:[7]

$$y_{\pm}(\varphi) = A(S'(\varphi))^{1/2}\exp\left[\pm i\int_0^{\varphi} S'(\varphi)d\varphi\right], \tag{6}$$

where

$$\omega_c S'(\varphi) = [2\Delta_{\max}(-\varepsilon) + \Delta_{\max}^2 - \Delta^2(\varphi)]^{1/2} \tag{7}$$

and A is the normalization coefficient. The BCS factors $u(\varphi)$ and $v(\varphi)$ in Eq. (23) of Ref. 5 are to be normalized together: $\overline{|u^2|}+\overline{|v^2|}=1$ (the bar in $\overline{(\ldots)}$ means the normalization integral: $(2\pi)^{-1}\int_0^{2\pi}(\ldots)d\varphi$). Two auxiliary expressions which follow from Eqs. (26)–(28) of Ref. 5:

$$\overline{|u^2|}=\frac{1}{2}\{\overline{|y|^2}+(i\omega_c/2E)\overline{(y^*y'-yy^{*'})}\},\quad \overline{|v^2|}=\frac{1}{2}\{\overline{|y|^2}-(i\omega_c/2E)\overline{(y^*y'-yy^{*'})}\} \tag{8}$$

immediately show that $\overline{|y|^2}=1$.

Expression (6) of Ref. 5, containing oscillatory effects

$$M=-\frac{\mu e}{\pi c}\sum_{\lambda}\overline{|u_\lambda(\varphi)|^2} \tag{9}$$

(λ enumerates the eigenvalues, the factor of 2 inserted in Eq. (6) of Ref. 5 accounts for spins, and $n(E_\lambda)\equiv 1$ for $E_\lambda<0$ and $T=0$), is converted to an integral over λ with the use of the Poisson formula:

$$\sum_{-\infty}^{+\infty}\delta(\lambda-n)=\sum_{k=-\infty}^{+\infty}e^{2\pi iK\lambda}. \tag{10}$$

Integration by parts transforms $M_{\rm osc}$ into[5]

$$M_{\rm osc}=\frac{i\mu e}{2\pi^2 c}\sum_K\frac{1}{K}\int_{-\infty}^{+\infty}e^{2i\pi K\lambda}\frac{d}{d\lambda}(\overline{|u_\lambda(\varphi)|^2})d\lambda. \tag{10$'$}$$

Although integration over λ acquires meaning only after the connection between λ and the energy is established, the threshold separating the ''localized'' and ''extended'' (in the WKB sense, (6), (7)) states is already seen in Eq. (10$'$): for ''localized'' states, $|E|<\Delta_{\max}$, the wave functions are real, and from (8) $\overline{|u_\lambda^2|}=1/2$. For ''extended'' states (6) we have

$$\overline{|u_\lambda|^2}=\frac{1}{2}\left\{1\pm\frac{\omega_c}{E_\lambda}|A_\lambda|^2\right\}, \tag{11}$$

where $|A_\lambda|^2$ is a function of energy (see Eq. (6)). The derivative in (10$'$) thus *eliminates states below* $\Delta_{\max}$, for which $\overline{|u_\lambda|^2}=1/2$ is energy-independent.

Returning to the summation over λ in Eqs. (10) and (10$'$), we need to construct a function

$$\lambda(E)=\Phi(E)/2\pi \tag{12}$$

such that the provision

$$\Phi(E_n)=2\pi n \tag{12$'$}$$

would enumerate all the energy levels in consecutive order. In the WKB approach $\Phi(E)$ is given by

$$S(2\pi,-\varepsilon)=(1/\omega_c)\int_0^{2\pi}S'(\varphi,-\varepsilon)d\varphi-2\pi\kappa, \tag{13}$$

which at large energies matches the Landau free-electron spectrum. The approach falls short near $(-\varepsilon)=0$.

We choose $\Delta^2(\varphi)$ near $\Delta_{\max}$ as

$$\Delta^2(\varphi)=\Delta^2_{\max}(1-a\varphi^2). \tag{14}$$

Expanding (13) in $(-\varepsilon)>0$, we obtain

$$S(2\pi,-\varepsilon)\simeq S(2\pi,0)-(l/2)\ln(l/\wedge), \tag{15}$$

with the useful notation

$$l=(-2\varepsilon)/\omega_c a^{1/2} \;\; ; \quad \wedge=(a^{1/2}\Delta_{\max}/\omega_c)\gg 1. \tag{16}$$

Similarly, the factor $|A|^2$ in (6) and (11) at small l obeys the proportionality:

$$|A|^2\propto[\ln(l/\wedge)]^{-1}. \tag{15$'$}$$

Because of the singularity (15) the ''numbering'' function $\Phi(E)$ cannot be comprised of the two WKB branches, the one that is given by (13) (at $(-\varepsilon)>0$), and the other which counts ''localized'' states ($(-\varepsilon)<0$).

Note that far from $\varphi=0$ the WKB solution

$$y(\varphi)=ay_+(\varphi)+by_-(\varphi) \tag{17}$$

is still correct. With the use of (5), (14), (16), Eq. (2$'$) can be solved near $\varphi=0$ in terms of the parabolic cylinder functions. It establishes a matrix relation between the coefficients (a,b) in (17) to the right of $\varphi=0_+$ and the other set (a',b') to the left of $\varphi=0_-$:

$$\begin{pmatrix} a' \\ b' \end{pmatrix}=\begin{pmatrix} \alpha & \beta \\ \beta^* & \alpha^* \end{pmatrix}\begin{pmatrix} a \\ b \end{pmatrix}. \tag{18}$$

Starting at $\varphi=0_+$, moving along with Eq. (17) toward $(2\pi)_-$, and using (18), we find that the periodicity condition for (3) provides the equation

$$R(l)\equiv|\alpha|(e^{i\tilde{S}}+e^{-i\tilde{S}})=2\cos 2\pi\kappa. \tag{19}$$

In Eq. (19) we have used the abbreviations

$$\tilde{S}=S(2\pi,-\varepsilon)-\theta, \;\; \alpha=|\alpha|\exp(i\theta). \tag{19$'$}$$

Of the two solutions of Eq. (19) we choose

$$e^{i\tilde{S}}=\frac{1}{|\alpha|}\{\cos 2\pi\kappa+i\sqrt{|\alpha|^2-\cos^2 2\pi\kappa}\}\equiv\rho(l), \tag{20}$$

because at $(-\varepsilon)$, i.e., l large and positive we have $|\alpha|\Rightarrow 1$, $\theta\Rightarrow 0$, and we return in this limit to (13). On the real axis of l the function

$$\Phi(l)=S(2\pi,l)-\theta(l)-\frac{1}{i}\ln\rho(l) \tag{21}$$

is positive, with $d\Phi/dl>0$, and matches asymptotically (at $l\to\infty$) the free-electron spectrum. With the help of (12) and (21) the oscillatory magnetization is

$$M_{\rm osc}=\frac{i\mu e}{2\pi^2 c}\sum_K \frac{1}{K}\int_{-\infty}^{+\infty} e^{iK\Phi(l)}\frac{d}{dl}(\overline{|u_l(\varphi)|^2})dl. \tag{22}$$

If $\Phi(l)$ is analytically continued into the complex l plane, the integration may be shifted into the upper half plane (Eqs. (11) and (15′) give the behavior of $d(\overline{|u_l|^2})/dl$ at large $|l|$). Consider singularities in (22). Thus from the expression for $|\alpha|$[a)]

$$|\alpha|=(1+e^{-\pi l})^{1/2} \tag{23}$$

we conclude that the branch points in (23) lie at

$$l_m=\pm(2m+1)i. \tag{24}$$

This is also true for $\theta(l)$ (see $\tilde{S}(2\pi,l)$ below). The definition of $\rho(l)$ together with (23) for $|\alpha|$ leads to square-root singularities at

$$l'_m=\pm(2m+1)i-\frac{1}{\pi}\ln(\sin^2 2\pi\kappa)\equiv l_m+l_0. \tag{24′}$$

For $\Phi(l)$ to be analytic in a strip at the real axis, the branch cuts in the l plane due to the singularities (24), (24′) must be chosen parallel to the imaginary axis.

The integral in (22) may be bent to the contours C_1 and C_2, each passing along the branch cuts (24) and (24′) in the upper half plane. The nonanalytic terms of Eq. (15) at $|\lambda|\sim 1$ are now absent in $\tilde{S}(2\pi,l)(c\sim 1)$:

$$\tilde{S}(2\pi,l)\simeq S(2\pi,0)+\frac{1}{2}l[\ln(\wedge\cdot c)]-\frac{1}{2i}\ln\left[\Gamma\left(\frac{1}{2}+\frac{il}{2}\right)/\Gamma\left(\frac{1}{2}-\frac{il}{2}\right)\right]. \tag{25}$$

Both integrals (along C_1 and C_2) rapidly converge.

It is necessary to normalize $\overline{|u_l(\varphi)|^2}$ to an accuracy better than that given by the WKB approximation in (6), (11). Fortunately the properties of the Bloch functions in a one-dimensional periodic potential are well-studied. With the help of Eq. (4.18) of Ref. 8 and our Eqs. (8) we derive

$$\overline{|u_l(\varphi)|^2}=\frac{1}{2}-\pi a^{1/2}\sin 2\pi\kappa\left[\frac{dR}{dl}\right]^{-1} \tag{26}$$

(here $R(l)$ is the right-hand side of (19)). After differentiation with respect to l in (22) has eliminated the 1/2 in (26), one may use for the rest the rapid convergence of the integrals to integrate back by parts in (22). The single terms under the sum symbol (22) become

$$I_K=\frac{i\pi a^{1/2}\sin 2\pi\kappa}{2}\int\frac{\exp(iK\Phi(l))dl}{(\sin^2 2\pi\kappa+e^{-\pi l})^{1/2}}, \tag{27}$$

with the integrals running along C_1, C_2. Assume that $\ln\wedge\gg 1$ in (25). First, the term in (22) with $K=1$ prevails. In addition, as is seen from (25), it is enough to consider the nearest singularities with $m=0$ in (24), (24′). When the branches of the square roots in (27) are properly defined, one obtains from (27) the contributions to I_1 from the two contour integrals, over C_1 and C_2, respectively:

$$I_1(C_1) = -\frac{(2\pi)^{3/2} a^{1/2} \tan 2\pi\kappa}{(\wedge c)^{1/2} (\ln \wedge c)^{1/2}} e^{iS(2\pi,0) + \frac{i\pi}{4}}, \tag{28}$$

$$I_1(C_2) = \frac{\pi a^{1/2} \sin 2\pi\kappa e^{\frac{i\pi}{4}}}{(\wedge c)^{1/2} (\ln \wedge c)^{1/2}} \left[\frac{\Gamma\left(1 - \frac{il_0}{2}\right)}{\Gamma\left(1 + \frac{il_0}{2}\right)} \right]^{1/2} \cdot e^{iS(2\pi,0) + \frac{il_0}{2} \ln(\wedge c)}, \tag{28'}$$

with l_0 from (24′). (I_1 has the form (28), (28′) for l_0 not too small ($l_0 \gtrsim (\ln \wedge c)^{-1}$). Otherwise the two contours C_1 and C_2 start to merge. Also, if l_0 becomes large ($\sin^2 2\pi\kappa \to 0$), expression (25) for $\tilde{S}(2\pi, l)$ which is correct at $|l| \sim 1$, ceases to be applicable.)

Expressions (28) explicitly present the periodic (in B^{-1}) oscillations in the magnetization as κ varies in the interval (0,1). It is notable that the amplitude is of the order of $(\omega_c/\Delta_{\max})^{1/2}$, i.e., is not exponentially small. Both (28) and (28′) lead to a large content of the higher harmonics. In principle, $M_{\rm osc}$ could be measured directly as a function of small changes in B. $I_1(C_1)$ exhibits a rather regular behavior in ΔB (i.e., κ), while $I_1(C_2)$ rapidly becomes chaotic due to the phase factor in (28′), $\exp[i(l_0/2)\ln(\wedge c)]$, contributing to the higher harmonics. In the Fourier analysis of the dHvA signal the first few harmonics are expected to be seen, with an intensity of the order of

$$(\omega_c/\Delta_{\max})^{1/2}. \tag{29}$$

Unfortunately, expression (29) does not take into account scattering of electrons on the flux lines. The term $h(\varphi)$ of Eq. (31) of Ref. 5, if included, adds to the potential of Eq. (2′):

$$2\Delta_{\max} h(\varphi). \tag{30}$$

Even though $h(\varphi) \sim v_F/d$ is small compared with $\Delta_{\max}$, expression (30) drastically distorts the potential near $\varphi = 0$. It is a local $\tilde{h}_{\max}$ in the vicinity of the maximum in $\Delta(\varphi)$ which now sets the energy threshold between ''localized'' and ''extended'' states. Note that although $h(\varphi)$ is rather irregular (for a given trajectory) and varies on a typical scale of $\delta\varphi \sim (d\omega_c/v_F)$, its local maxima produce potential barriers in (30) which remain impenetrable in the quasiclassical sense. The above analysis of $M_{\rm osc}$ can be performed around $\tilde{h}_{\max}$ in exactly the same manner as above. There is a change in the scale (29), because the curvature a near a maximum in (30) is much higher than in (14). Without going into details, we comment that this only increases the effect, because the potential $h(\varphi)$ near $\tilde{h}_{\max}$ comprises a much sharper barrier as compared with Eq. (14).

The major destructive effect comes from the phase factor in (25), $S(2\pi,0)$. At $h(\varphi) \neq 0$, $S(2\pi,0)$ may be expanded in $\delta h(\varphi) = h(\varphi) - \tilde{h}_{\max}$. (Now $(-\varepsilon) \Rightarrow E - \Delta_{\max} - \tilde{h}_{\max}$.) The fluctuating part, $\delta S(2\pi,0)$, is

$$\delta S(2\pi,0) = -(\Delta_{\max}/\omega_c) \int_0^{2\pi} \delta h(\varphi) (\Delta_{\max}^2 - \Delta^2(\varphi))^{-1/2} d\varphi. \tag{31}$$

Since $\langle \delta h(\varphi) \rangle$ (the average over all trajectories) is obviously zero, fluctuations in $\exp(i\delta S(2\pi,0))$ lead, as in Ref. 5, to an effective Dingle factor of the form

$$\exp(-v_F/d\omega_c) \Rightarrow \exp(-(\Delta/\omega_c)(\xi_0/d)). \quad (32)$$

The exponent in (32) provides much more favorable conditions for observation of the dHvA effect than previous results.[4]

To conclude, in the developed mixed state of an anisotropic superconductor there exists an energy threshold sorting excitations into two categories: localized and extended. Crossing of this threshold by the levels of the excitations as the magnetic field is varied is a new mechanism for quantum oscillations. Scattering on the flux lines reduces the dHvA effect. Nevertheless, the effect remains bigger than anticipated.

The work was supported by the NHMFL through NSF cooperative agreement DMR-9016241 and the State of Florida.

[a)]To the best of the author's knowledge, the complete matrix in (17) has not been published, although transmission/reflection processes for a parabolic barrier have been studied (see Ref. 7). The author thanks V. Pokrovsky for a discussion of the references.

[1] T. Terashima *et al.*, Phys. Rev. B **56**, 5120 (1997).
[2] Y. Onuki, in *Proceedings of the Conference SCES '98*, Paris, 1998 (to be published).
[3] A. A. Abrikosov, Zh. Éksp. Teor. Fiz. **32**, 1442 (1957) [Sov. Phys. JETP **5**, 1174 (1957)].
[4] K. Maki, Phys. Rev. B **44**, 2861 (1991); M. J. Stephen, Phys. Rev. B **45**, 5481 (1992).
[5] L. P. Gor'kov and J. R. Schrieffer, Phys. Rev. Lett. **80**, 3360 (1998).
[6] E. A. Shapoval, Zh. Éksp. Teor. Fiz. **47**, 1007 (1965) [Sov. Phys. JETP **20**, 675 (1965)].
[7] L. D. Landau and E. M. Lifshitz, *Quantum Mechanics: Non-Relativistic Theory*, Pergammon Press, New York, 1977.
[8] W. Kohn, Phys. Rev. **115**, 809 (1959).

Published in English in the original Russian journal. Edited by Steve Torstveit.

Dynamic polarization of nuclei in a self-organized ensemble of quantum-size *n*-InP/InGaP islands

R. I. Dzhioev,[a] B. P. Zakharchenya, V. L. Korenev, P. E. Pak, M. N. Tkachuk, D. A. Vinokurov, and I. S. Tarasov
A. F. Ioffe Physicotechnical Institute, Russian Academy of Sciences, 194021 St. Petersburg, Russia

(Submitted 6 October 1998)
Pis'ma Zh. Éksp. Teor. Fiz. **68**, No. 9, 711–714 (10 November 1998)

Dynamic polarization of ^{31}P nuclei is observed in a self-organized system of InP islands grown by metalorganic–hydride epitaxy in an InGaP matrix. The polarized nuclei produce an effective magnetic field which acts on the polarization of the excitonic radiation. Optical detection of the magnetic resonance signal from ^{31}P nuclei in the crystal lattice of nanosize InP islands is successfully carried out.. © *1998 American Institute of Physics.* [S0021-3640(98)01121-9]

PACS numbers: 71.35.Ji, 75.70.Cn, 76.70.Hb

1. The ground state of an $e1$-$hh1$ ($1s$) exciton with a heavy hole in a quantum well with the zinc blende lattice is fourfold degenerate and is characterized by the projection of the angular momentum $M=s+j=\pm 1,\pm 2$ on the growth axis $z \parallel [001]$ of the structure (the electron spin $s=\pm 1/2$ and the hole angular momentum $j=\pm 3/2$). The exchange interaction splits this state into a radiative doublet $|\pm 1\rangle$ and two close-lying optically inactive singlets, which are a superposition of the states $|\pm 2\rangle$. Localization of an exciton on an anisotropic island lowers the symmetry of the system, and in the process the radiative doublet splits into two sublevels, linearly polarized in two orthogonal directions.[1] When excitons are excited by circularly polarized light the photoluminescence (PL) in zero magnetic field is unpolarized because of the anisotropic exchange interaction, which mixes the radiating states $|+1\rangle$ and $|-1\rangle$. In a magnetic field in Faraday geometry ($B \parallel z$) the Zeeman effect decouples them, and the PL is circularly polarized, i.e., the magnetic field restores the orientation of the optically active excitons.[2] Similarly a magnetic field restores the spin polarization of the optically inactive excitons (the states $|\pm 2\rangle$). Their polarization appears in the PL of *n*-InP islands in the system InP/InGaP as a result of the formation of a D^0X complex of an exciton at a neutral donor or at a ''charged exciton'' (trion).[3] The degree of circular polarization of the PL of the complex D^0X is determined by the polarizations of both the excitons and electrons at the donors prior to formation of the complex.

The hyperfine interaction of the electrons and nuclei in a crystal lattice should have a large effect on the spin splitting of excitonic levels and on the polarization of the excitons. Optically oriented electrons in excitons transfer the angular momentum to the nuclear spin system (NSS) by means of the Overhauser effect. In turn, the polarized nuclei produce an effective magnetic field B_N which changes the spin splitting of the

levels. The dynamic polarization of nuclei in GaAs/AlGaAs quantum wells has been reported in Ref. 4, where it was shown that the polarization of the nuclei is due to electrons and excitons localized at donors or well-width fluctuations. This conclusion has been confirmed by near-field spectroscopy experiments,[5] where excitons localized on isolated island fluctuations of the quantum well width were observed directly.

This work is devoted to the observation of the dynamic polarization of nuclei in a self-organized ensemble of quantum-size donor-doped InP islands in an InGaP matrix. The effective magnetic field $B_N \sim 100$ G of the polarized nuclei influences the polarization of the optically inactive excitons. Optical detection of the NMR signal of ^{31}P nuclei is accomplished. It is shown that the characteristic spin-relaxation times of the NSS are $T_1 \geqslant 33 \mu$s.

2. The structures were grown by metalorganic–hydride epitaxy on GaAs substrates with $(100) \pm 30'$ orientation and contained (in order) a 500 nm thick $In_{0.5}Ga_{0.5}P$ buffer layer lattice-matched with the substrate, a layer of nanosize InP islands with nominal thicknesses of three or five monolayers, and a 50 nm thick $In_{0.5}Ga_{0.5}P$ layer on top. The layers contained donor impurities at the level 10^{15} cm^{-3}.

The experimental samples were lowered into a cryostat with liquid helium and placed at the center of an electromagnet. The photoexcitation was performed with a 10 W/cm^2 He–Ne laser beam ($h\nu = 1.96$ eV) directed along the growth axis of the structure $z \parallel [001]$. The polarization of the photoluminescence was measured in a magnetic field in the Faraday geometry at the maximum of the recombination emission band of the InP islands ($\lambda = 723$ nm).

The optical orientation of electrons and the measurement of the degree of circular polarization of the recombination radiation were performed by two methods.

1) In a regime in which the sign of the circular polarization of the exciting light changed with a high frequency (the modulation period of the quartz polarization modulator was 33 μs), while the polarization of the luminescence was analyzed with a quarter-wave phase plate and a linear polarizer. In this case there is not enough time for the nuclear spin to follow the polarization of the electrons and there is no dynamic polarization of the nuclei (the spin relaxation time of the nuclei $T_1 \sim 0.1-1$ s).[6] The effective degree of circular polarization $\rho_c = (I_+^+ - I_+^-)/(I_+^+ + I_+^-)$ is measured, where I_+^+ and I_+^- are the intensities of the σ^+ components of luminescence in the case of σ^+ and σ^- excitation, respectively. The filled circles in Fig. 1a show the function $\rho_c(B)$ corresponding to the recombination of a D^0X complex with excitation by light with a sign-alternating circular polarization. It is symmetric with respect to a change in the sign of the magnetic field and saturates in fields $B \approx 300$ G. This dependence reflects the restoration of the spin orientation of optically inactive excitons as a result of the Zeeman splitting overcoming their exchange splitting. For $B = 0$ the excitons are unpolarized, while the nonzero value of $\rho_c(B=0)$ is due to the magnetic-field-independent spin polarization of electrons at donors.[3]

2) Excitation by light whose circular polarization remains constant in time, in which case the Overhauser effect arises. A quartz modulator serves as the analyzer of the luminescence polarization. The degree of circular polarization $\rho_c = (I_+^+ - I_-^+)/(I_+^+ + I_-^+)$ is measured. In the present samples there are no effects due to circular dichroism, so that the parameters ρ_c in the two geometries of the experiment are identical and can be

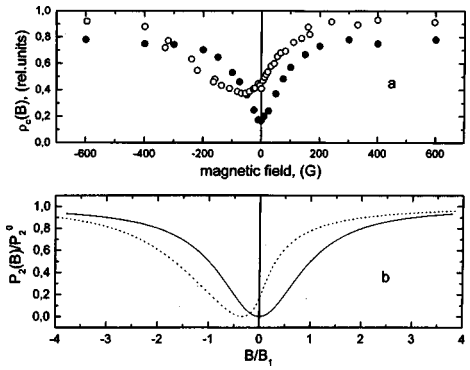

FIG. 1. Restoration of the optical orientation of inactive excitons in a magnetic field in Faraday geometry. a: Experimental points were measured with: ● — excitation by circularly polarized light, the sign of whose circular polarization was changed with a high frequency; ○ — excitation by light with a constant sign of the circular polarization. b: The solid curves were computed using Eqs. (1) and (2): $aP_d/B_1 = bP_2^0/B_1 = 0$ (solid curve) and $aP_d/B_1 = 0.33$, $bP_2^0/B_1 = 0.70$ (dashed curve).

viewed as an ordinary Stokes parameter characterizing the circular polarization of luminescence due to the circular polarization of the excitation. The open circles in Fig. 1a show the function $\rho_c(B)$ measured with excitation by light with constant circular polarization. One can see that the minimum of $\rho_c(B)$ is reached in a field $B \approx -55$ G and not for $B = 0$, as was the case for excitation by light with sign-alternating polarization. Moreover, the dependence is not symmetric with respect to the position of the minimum. These results indicate dynamic polarization of the nuclei. Indeed, in this case the total field $B + B_N$ acts on the excitons. If the field B_N does not depend on the magnitude of the external field B, then the presence of nuclear polarization should lead only to a shift of the curve $\rho_c(B)$ along the abscissa axis by an amount equal to the nuclear field. The presence of asymmetry relative to the minimum of $\rho_c(B)$ indicates that the field B_N varies with the external field. These results can be explained by taking into account the fact that the nuclei in *n*-InP islands are polarized by both electrons at donors and electrons in excitons. We shall use a model in which the field B_N of the nuclei is determined by the sum of two terms: One term, $B_{Nd} = aP_d$, is proportional to the magnetic-field-independent polarization P_d of electrons at donors, and the other, $B_{Nx} = bP_2(B)$, is determined by the polarization of electrons in optically inactive excitons, i.e., ultimately by the polarization $P_2(B)$ of inactive excitons. Then

$$B_N = B_{Nd} + B_{Nx} = aP_d + bP_2(B). \tag{1}$$

Here the phenomenological parameters a and b are assumed to be independent of the magnetic field and characterize the efficiency of the polarization of nuclei by electrons at donors and in excitons, respectively. The field B_{Nd} shifts the curve $P_2(B)$, while the field B_{Nx} introduces an asymmetry of the curve relative to the minimum. The polarization $P_2(B)$ of the excitons is determined by the competition between the Zeeman splitting $\mu_B g(B + B_N)$ of the levels and the anisotropic exchange splitting δ_1 of the optically inactive states:

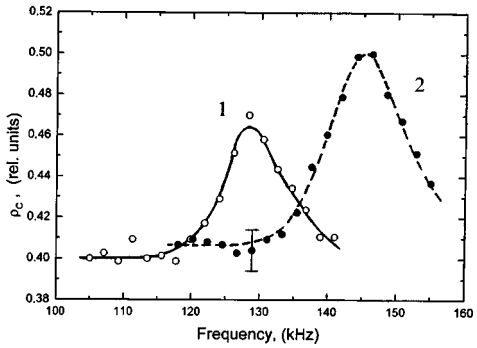

FIG. 2. NMR signal of ^{31}P nuclei, measured in fields $B=80$ G (curve *1*) and $B=90$ G (curve *2*).

$$P_2(B)=P_2^0\frac{(B+B_N)^2}{(B+B_N)^2+B_1^2}, \tag{2}$$

where $B_1=\delta_1/\mu_B g$, μ_B is the Bohr magneton, g is the g factor of optically inactive excitons, and P_2^0 is the initial degree of polarization of the excitons at the time of their formation. The results obtained by solving Eqs. (1) and (2) simultaneously are displayed in Fig. 1b: the solid curve is constructed in the absence of nuclear polarization ($B_N=0$) and the dashed curve was calculated with $aP_d/B_1=0.33$ and $bP_2^0/B_1=0.70$. Comparing Figs. 1a and 1b shows that the proposed simple model agrees qualitatively with the experimental curves obtained with constant and variable circular polarization of the exciting light. Therefore the presence of long spin relaxation times and the magnetic field dependences $\rho_c(B)$ indicate dynamic polarization of the nuclei in the system of InP islands.

The observation of a NMR signal is a direct proof of the Overhauser effect. Detection of the NMR signal was accomplished by measuring the difference $I_+^+-I_-^+$ as a function of the frequency of an rf field transverse to the external magnetic field. To improve the signal/noise ratio, an AI-1024 apparatus for accumulating analog signals was used. The NMR spectra of ^{31}P nuclei in 80 G and 90 G fields are presented in Fig. 2 (curves *1* and *2*).

In conclusion, we note that we have examined above the influence of a field (both external and nuclear) on the polarization of optically inactive excitons. Optically active excitons in fields <1 kG are unpolarized because of the large anisotropic exchange splitting $\delta_2\sim 100$ μeV, which mixes the states $|+1\rangle$ and $|-1\rangle$. The characteristic field restoring their polarization is ≈ 1 T.[3]

In summary, the dynamic polarization of nuclei by electrons at donors and excitons in quantum-size *n*-InP/InGaP islands was observed in this work. A nonlinear strongly coupled excitonic–nuclear spin system, where the nuclear spin influences the polarization of the excitons (by means of the nuclear field) and in turn itself also depends on it (because of the Overhauser effect), is realized in the InP islands. Optical detection of the NMR signal on ^{31}P nuclei was accomplished.

We are deeply grateful to I. A. Merkulov for discussions. The work of R. I. D.,

B. P. Z., V. L. K., and M. N. T. was partially supported by the Russian Fund for Fundamental Research, Projects Nos. 96-02-16887a and 98-02-18213. D. A. V. and I. S. T. were supported by Project N96-2005 of the Interdisciplinary Science and Technology Program ''Physics of Solid-State Nanostructures.''

[a)]e-mail: orient@orient.ioffe.rssi.ru

---

[1] E. L. Ivchenko and G. E. Pikus, *Superlattices and Other Heterostructures. Symmetry and Optical Phenomena,* Springer-Verlag, Berlin, 1995.
[2] R. I. Dzhioev, H. M. Gibbs, E. L. Ivchenko *et al.*, Phys. Rev. B **56**, 13405 (1997); R. I. Dzhioev, B. P. Zakharchenya, E. L. Ivchenko *et al.*, JETP Lett. **65**, 804 (1997).
[3] R. I. Dzhioev, B. P. Zakharchenya, V. L. Korenev *et al.*, Fiz. Tverd. Tela (St. Petersburg) **40**, 1745 (1998) [Phys. Solid State **40**, 1587 (1998)].
[4] V. K. Kalevich, V. L. Korenev, and O. M. Fedorova, JETP Lett. **52**, 349 (1990).
[5] S. W. Brown, T. A. Kennedy, D. Gammon, and E. S. Snow, Phys. Rev. B **54**, R17339 (1996); D. Gammon, S. W. Brown, E. S. Snow *et al.*, Science **277**, 85 (1997).
[6] B. P. Zakharchenya and F. Maĭer (Eds.), *Optical Orientation. Current Problems of Condensed-Media Science,* Nauka, Leningrad, 1989.

Translated by M. E. Alferieff

$\bar{\partial}$ problem for the generalized Korteweg–de Vries equation

A. I. Zenchuk[a)]
L. D. Landau Institute of Theoretical Physics, Russian Academy of Sciences, 142432 Chernogolovka, Moscow Region, Russia

(Submitted 9 September 1998)
Pis'ma Zh. Éksp. Teor. Fiz. **68**, No. 9, 715–720 (10 November 1998)

The generalized Korteweg–de Vries equation, which has applications in hydrodynamics, in particular, is essentially the first example of a case in which the $\bar{\partial}$ dressing of a nonlinear equation is constructed by introducing into the dressing operator an arbitrary function of the independent variables of this equation. The proposed algorithm reveals a class of solutions of this equation which are expressed in terms of the solution of algebraic equations. An example of a new type of solution whose derivative with respect to the independent variables has a power-law singularity at some point is presented.
 [S0021-3640(98)01221-3]

PACS numbers: 03.40.Kf, 02.30.Hq, 02.30.Rz

The $\bar{\partial}$ problem[1,2] is the modern version of the dressing method[3] — the basic method of constructing the solutions of a wide class of integrable nonlinear equations of mathematical physics, such as the Korteweg–de Vries (KdV) equation. In the present letter I propose a new algorithm for constructing the solutions of the generalized KdV equation,[4] which, like the KdV equation itself, has applications in hydrodynamics,[5] where it describes one of the shallow-water approximations (if $\Gamma>0$ in Eq. (1), see below). Its complete integrability was proved in Ref. 4. The regular method of constructing solutions of this equation by means of the inverse spectral scattering problem[6,7] encounters the problem of solving a spectral equation (19) (see below). I shall formulate the dressing method for a generalized KdV equation by using a nonlocal $\bar{\partial}$ problem, which reduces the process of constructing the solutions of a nonlinear equation to solving linear integral and algebraic equations. This approach demonstrates the possibility of using one of the latest modifications of the dressing method, based on the introduction of an arbitrary function of the independent variables (the time and the coordinate) into the dressing operator,[8,9] making it possible to construct a wide class of solutions of the generalized KdV equation which are expressed explicitly in terms of the solution of algebraic equations. The simplest solution constructed by this method is a representative of a new class of soliton-type solutions whose first derivative with respect to the independent variable possesses a *power-law singularity* at some point. I call attention to the fact that in the peakon-type solutions studied previously[5] the derivatives have a *finite jump* at some point.

The nonlinear equation in question has the form

$$m_t+2\kappa u_x-um_x-2u_xm=0,\quad m=u_{xx}-\Gamma u, \tag{1}$$

where Γ and κ are real constants. The integral equation (in this case a scalar equation) in the plane of the complex parameter λ,

$$\psi(\lambda;x,t)=\eta+\frac{1}{2\pi i}\int\frac{d\nu\wedge d\bar{\nu}}{\nu-\lambda}\int\psi(\mu;x,t)R(\mu,\nu;x,y)d\mu\wedge d\bar{\mu},\qquad \eta=\frac{1}{\lambda}, \tag{2}$$

is called a nonlocal $\bar{\partial}$ problem. Here δ is the Dirac delta function ($\int\delta(\lambda)d^2\lambda=-2i, i^2=-1$), R is the kernel of the integral operator which ensures that Eq. (2) has a single-valued solution, and the function η is called the normalization of the problem (for the present problem it has a specific form). To determine the relation of this linear equation with Eq. (1), we proceed as follows. First, we introduce the parameters x and t, which are independent variables of the desired nonlinear equation, in the kernel R as follows:

$$R(\mu,\lambda;x,t)=R_0(\mu,\lambda)e^{K(\mu;x,t)-K(\lambda;x,t)},\qquad K(\lambda;x,t)=\lambda\Phi+\frac{\gamma t}{\lambda-a},\qquad a\neq 0. \tag{3}$$

Here a and γ are constants and $\Phi=\Phi(x,t)$ is an arbitrary function, which was discussed at the beginning of this letter. In what follows we shall require the asymptotic behavior of the function $\psi(\lambda)$ as $\lambda\to\infty$, 0. According to Eq. (2), these asymptotic forms are

$$\psi\to\sum_{k>0}\frac{\psi_k}{\lambda^k},\quad \lambda\to\infty,\qquad \psi\to\frac{1}{\lambda}+\sum_{k\geqslant 0}\psi_k(0)\lambda^k,\quad \lambda\to 0, \tag{4}$$

$$\psi_k\equiv\psi_k(x,t)=\frac{i}{2\pi}\int\nu^{k-1}d\nu\wedge d\bar{\nu}\int\psi(\mu;x,t)R(\mu,\nu;x,t)d\mu\wedge d\bar{\mu},$$

$$\psi_k(0)\equiv\psi_k(0;x,t)=\frac{1}{2\pi i}\int\left(\frac{1}{\nu}\right)^{k+1}d\nu\wedge d\bar{\nu}\int\psi(\mu;x,t)R(\mu,\nu;x,t)d\mu\wedge d\bar{\mu}.$$

Note that by virtue of Eq. (3) the functions ψ_k and $\psi_k(0)$ depend explicitly on the arbitrary function Φ. We shall make use of this fact below (see Eqs. (12) and (13)). In addition, we impose on the kernel R an additional condition which is necessary for implementing the algorithm for constructing a nonlinear equation:

$$R(\mu,\lambda)(\Omega(\mu)-\Omega(\lambda))=0,\quad \Omega(\lambda)=\frac{1}{\lambda(\lambda-a)}, \tag{5}$$

which means that R_0 has the form

$$R_0=r_0(\mu,\lambda)(\delta(\lambda-\mu)+\delta(\lambda+\mu-a)).$$

The $\bar{\partial}$ problem is now completely formulated. Next we consider a short algorithm for constructing Eq. (1) (a detailed derivation of the nonlinear equations from the $\bar{\partial}$ problem (2) is given in Refs. 1 and 2) and indicate its characteristic features which are due to the presence of the arbitrary function Φ in the problem.[8]

Let the kernel R_0 ensure the uniqueness of the solution of Eq. (2). Then together with ψ the solutions of Eq. (2) with the same kernel R will be the following functions but with different normalizations η, which can be easily obtained by direct calculation (we will not write out the explicit form of the normalizations here (see Refs. 1 and 2)):

$$D_x\psi\equiv(\partial_x+\partial_x K)\psi=\psi_x+\Phi_x\lambda\psi,\quad D_x^2\psi, \tag{6}$$

$$D_t\psi\equiv(\partial_t+\partial_t K)\psi=\psi_t+\Phi_t\lambda\psi+\frac{\gamma}{\lambda-a}\psi,\quad \Omega^k\psi,\quad k\in\mathbf{Z}.$$

The problem is to construct, using a combination of these solutions, the solution of Eq. (2) which equals zero identically or, equivalently, a solution with zero normalization. Two independent combinations of the functions (6) lead to such a solution:

$$L_1\psi\equiv D_t\psi-uD_x\psi+V\Omega D_x\psi+W\psi=0, \tag{7}$$

$$L_2\psi\equiv D_xD_x\psi-U_1\frac{1}{\Omega}\psi-U_2D_x\psi=0, \tag{8}$$

where

$$V^{-1}=-\left(\frac{\psi_x(a)}{a}+\Phi_x\psi(a)\right)\frac{1}{\gamma\psi(a)}, \tag{9}$$

$$u=\frac{\Phi_t}{\Phi_x},\quad W=\frac{\gamma}{a}+\frac{\psi_{1x}(0)}{a}+\frac{\Phi_x}{a}, \tag{10}$$

$$U_1=\Phi_x^2,\quad U_2=\frac{1}{\psi_1\Phi_x}(2\Phi_x\psi_{1x}+\Phi_{xx}\psi_1+U_1a\psi_1). \tag{11}$$

Equations (7) and (8) form an overdetermined system of linear equations. Since its coefficients contain the arbitrary function Φ, an additional condition, which will be an equation for the function Φ, can be imposed on them, thereby removing the arbitrariness in its choice. Let this condition be the reduction $V=1$. When Eq. (9) is taken into account, this means that

$$\psi(a)\neq0,\quad \psi_x(a)=-(\Phi_x+\gamma)a\psi(a) \tag{12}$$

or

$$\psi(a)=ce^{-(\Phi+\gamma x)a},\quad c=\text{const}\neq0. \tag{13}$$

In the general case Eq. (14) must be solved numerically, since the explicit dependence of $\psi(a)$ on Φ is determined by the choice of the kernel R_0 and can be quite complicated. In particular cases it can be solved analytically. Such a situation is studied in the examples presented below.

It follows from the condition (12) that $U_2=$ const in Eq. (8). Indeed, we take the limit of Eq. (8) as $\lambda\to a$ and use the condition (12). The expression in front of $(\lambda-a)^0$ is

$$(U_2+a\gamma)a\gamma\psi(a)=0,$$

which, since $a\neq0,\gamma\neq0$, and $\psi(a)\neq0$, means that

$$U_2=-a\gamma. \tag{14}$$

As will be seen below, the function u is a solution of the desired nonlinear equation (1). For this reason, it is desirable to express the potentials U_1 and W of the system (7)

and (8) in terms of the function u. For this we expand Eq. (7) in powers of the parameter $\varepsilon_1=1/\lambda$ as $\lambda\to\infty$ and Eq. (8) in powers of the parameter $\varepsilon_2=\lambda$ as $\lambda\to 0$, and we write out the first nontrivial terms of these expansions

$$\psi_{1t}-u\psi_{1x}+W\psi_1=0, \tag{15}$$

$$\psi_{1xx}(0)+a\gamma\psi_{1x}(0)+\Phi_{xx}+a\gamma\Phi_x+U_1 a=0. \tag{16}$$

We now integrate Eq. (14) in order to obtain from it an expression for ψ_1, which we substitute into Eq. (15). Taking the integration constant to be zero, we find

$$W=\frac{1}{2}(u_x-a\gamma u). \tag{17}$$

We obtain from Eq. (16) an expression for U_1, taking into account Eq. (10) (which determines $\psi_1(0)$) and Eq. (17):

$$U_1=-\frac{1}{2}u_{xx}+\frac{1}{2}a^2\gamma^2 u+\gamma^2. \tag{18}$$

Now the linear system (7) and (8) can be rewritten in the form presented in Ref. 5 in an investigation of Eq. (1) ($\Psi=\psi e^{K-a\gamma x/2+a\gamma\Omega t/2}$):

$$\Psi_t+(\Omega-u)\Psi_x+\frac{1}{2}u_x\Psi=0, \tag{19}$$

$$\Psi_{xx}-\frac{1}{4}a^2\gamma^2\Psi+\frac{(m-\kappa)}{2\Omega}\Psi=0,\quad m=u_{xx}-\Gamma u,\quad \kappa=2\gamma^2,\quad \Gamma=a^2\gamma^2, \tag{20}$$

which is the consistency condition for this system. Here Ω plays the role of a spectral parameter. In addition, a and γ must be purely real or purely imaginary, since we are interested in Eq. (1) with real coefficients. The real solutions of this equation correspond to real or purely imaginary solutions Φ of the coupling equation (13). This question is worked out below for a specific example.

It is evident from Eq. (20) that $\kappa\neq 0$ in Eq. (1). However, as one can easily see, the mapping

$$\left\{t\to t,\quad x\to x-\frac{\kappa}{\Gamma}t,\qquad u\to u-\frac{\kappa}{\Gamma}\right\} \tag{21}$$

cancels in Eq. (1) the term proportional to κ. For this reason the $\overline{\partial}$ problem furnishes a class of solutions for Eq. (1) with arbitrary κ. It follows from Eq. (21) that the solutions of Eq. (1) with $\kappa\neq 0$ which decrease to zero at infinity ($x\to\infty$) correspond to the solutions of Eq. (1) with $\kappa=0$ which approach a constant at infinity.

EXPLICIT SOLUTIONS

Let us now examine a simple class of explicit solutions of Eq. (1). Specifically, let the kernel R_0 in Eq. (2) be of the form

$$R_0(\mu,\lambda)=-\frac{\pi i}{2}(\mu-\lambda)(\delta(\lambda-\mu)+\delta(\lambda-a+\mu))\sum_{k=1}^{N}\frac{p_k}{2b_k-a}\delta(\mu-b_k), \tag{22}$$

where p_k and b_k are real constants and $b_k \neq a \neq 0$, $b_k \neq a/2$. In this case Eq. (2) can be solved explicitly, and Eq. (13) for determining the function Φ will assume the form

$$\frac{1}{a}-\sum_{k=1}^{N}\psi(b_k)\exp\left((2b_k-a)\Phi+\gamma t\frac{2b_k-a}{b_k(b_k-a)}\right)\frac{p_k}{b_k}=ce^{-(\Phi+\gamma x)a}, \tag{23}$$

where the functions $\psi(b_k)$ satisfy the system of linear equations

$$\psi(b_j)=\frac{1}{b_j}+\sum_{k=1}^{N}\frac{\psi(b_k)p_k}{a-b_k-b_j}\exp\left((2b_k-a)\Phi+\gamma t\frac{2b_k-a}{b_k(b_k-a)}\right), \quad j=1,\ldots,N. \tag{24}$$

Specifically, if the constants b_k are multiples of $a/2$ ($2b_k=n_k a, n_k \in \mathbf{Z}, n_k \neq 1$), then Eqs. (23) and (24) reduce to a polynomial equation for the function $\phi=e^{a\Phi}$. Examples of the solutions of Eq. (1) for which $c=1$ are examined below.

Example 1. Let $N=1$, $p_1=\beta$, and $b=-a/2$ in Eq. (22). Then the polynomial equation into which the system (23) and (24) transforms is cubic,

$$a\phi^3-\phi^2a^2\exp-ax-\frac{9}{2}\beta\phi\ \exp-\frac{8\gamma}{3a}t+\frac{1}{2}\beta a\ \exp-ax-\frac{8\gamma}{3a}t=0, \tag{25}$$

and the solutions of Eq. (1) are related with the solutions of Eq. (25) by the formula (see Eq. (10))

$$u=\frac{\Phi_t}{\Phi_x}=\frac{\phi_t}{\phi_x}=\frac{8\beta}{3a^3}\frac{9\phi e^{ax}-a}{2\phi^2e^{8\gamma/(3a)t}-\beta}. \tag{26}$$

Let a and γ be real constants. In this case the coefficients of Eq. (25) are real and it has real solutions, each of which generates a real solution u of Eq. (1). For definiteness let $a=\gamma=1$. Such a solution is unique if $\beta<0$:

$$u=-\frac{16}{3}\frac{3e^{-\eta}((\sinh(\eta)\cosh(\eta)^2)^{1/3}+(\sinh(\eta)^2\cosh(\eta))^{1/3})+1}{12e^{2\eta}((\sinh(\eta)\cosh(\eta)^2)^{1/3}+(\sinh(\eta)^2\cosh(\eta))^{1/3}+e^{\eta}/2)^2+1},$$

$\eta=-1/2x+2/3t-\alpha$. Here $\alpha=\ln(\sqrt{3/2\sqrt{6|\beta|}})$, though, evidently, α is arbitrary since it can be removed by a coordinate shift $x\to x-2\alpha$, which trivially affects the dressing operator $K(\lambda)$ in Eq. (3) and does not affect Eq. (1). Note that as $\eta\to 0$ the solution $u\to -4/3+4\eta^{2/3}$, and the η derivative of the solution has a *power-law singularity*: $\partial_\eta u \sim 1/\eta^{1/3}$. This is the fundamental difference between the solution constructed above and the peakons found in Ref. 5, whose derivative has a *finite jump* at a certain point. The solution u has exponentially decaying asymptotic behavior: $u\to -(8/9)^2\exp(-4|\eta|)$ as $|\eta|\to\infty$.

If $\beta>0$, then there are three different real solutions u_1, u_2, and u_3

$$u_1=\frac{16}{3}\frac{3e^{-\eta}\sqrt{2\cosh(2\eta)}\cos(\theta/3)+1}{12e^{2\eta}(\sqrt{2\cosh(2\eta)}\cos(\theta/3)+e^{\eta}/2)^2-1}, \quad \theta=\arctan(e^{-2\eta}), \tag{27}$$

$$u_{2,3}=\frac{8}{3}\frac{2-3e^{-\eta}\sqrt{2\cosh(2\eta)}(\cos(\theta/3)\mp\sqrt{3}\sin(\theta/3))}{3e^{2\eta}(\sqrt{2\cosh(2\eta)}(\cos(\theta/3)\mp\sqrt{3}\sin(\theta/3)-e^{\eta})^2-1}, \tag{28}$$

which grow as $\exp(2|\eta|)$ as $\eta\to-\infty(u_1)$, as $\eta\to\infty(u_2$, the minus sign in Eq. (28)), and as $|\eta|\to\infty(u_3)$.

In all integrable models covered by the $\bar{\partial}$ problem with a dressing operator K which is linear with respect to the independent variables, soliton solutions parametrized by the constants b_k correspond to a kernel of the form (22). Here, however, the choice of these constants determines the form of the algebraic equation from which the function Φ must be found. For this reason, they are always fixed. This explains the absence of any parameters (except for the unimportant parameter α) in all solutions presented above. The parameters a and γ in Eqs. (22)–(26) cannot be regarded as free, since they fix the coefficients in Eq. (1) (in this case $\kappa=2,\ \Gamma=1$).

Example 2. Let $N=1,\ p_1=\beta, b=2a$, and $a=\gamma=1$. Then, instead of Eq. (24) we obtain the quartic equation

$$\beta(\phi^4-4\phi^3e^{-x})+12\phi e^{-3t/2}-12e^{-x-3t/2}=0,$$

and the solution of Eq. (1) is related with the solutions of this equation by the formula

$$u=\frac{\Phi_t}{\Phi_x}=\frac{\phi_t}{\phi_x}=-\frac{9}{2}\frac{\phi e^x-1}{\phi^3\beta e^{3t/2}+3}.$$

We will not analyze these solutions here.

I thank S. V. Manakov for a discussion of this work and D. D. Holm for formulating the problem. This work was supported by the Russian Fund for Fundamental Research (Grant No. 98-01-0525).

[a)]e-mail: zenchuk@itp.ac.ru

[1] V. E. Zakharov and S. V. Manakov, Funk. Analiz. **19**(2), 11 (1985).
[2] L. V. Bogdanov and S. V. Manakov, J. Phys. A: Math. Gen. **21**, L537 (1988).
[3] V. E. Zakharov and A. B. Shabat, Funk. Analiz. **8**(3), 43 (1974).
[4] B. Fuchssteiner and A. S. Fokas, Physica D **4**, 47 (1981).
[5] R. Camassa and D. D. Holm, Phys. Rev. Lett. **71**, 1661 (1993).
[6] M. S. Alber, R. Camassa, D. D. Holm, and J. E. Marsden, Lett. Math Phys. **32**, 137 (1994).
[7] A. S. Fokas, Physica D **87**, 145 (1995).
[8] A. Degasperis, S. Manakov, and A. Zenchuk, to be published.
[9] A. I. Zenchuk, JETP Lett. **66**, 222 (1997).

Translated by M. E. Alferieff